Numerical Simulation of Fine-Wire Instruments for In-Situ High-Altitude Turbulence Measurements

by

Christopher A. Roseman

M.S., University of Colorado Boulder, 2020

B.S., Bradley University, 2017

A thesis submitted to the

Faculty of the Graduate School of the

University of Colorado in partial fulfillment

of the requirements for the degree of

Doctor of Philosophy

Department of Aerospace Engineering Sciences

2022

Committee Members:

Brian M. Argrow, Chair

Dale Lawrence

Iain Boyd

Peter Hamlington

John Farnsworth

Timothy Minton

Roseman, Christopher A. (Ph.D., Aerospace Engineering Sciences)

Numerical Simulation of Fine-Wire Instruments for In-Situ High-Altitude Turbulence Measurements

Thesis directed by Prof. and Chair Brian M. Argrow

Fine-wire instruments have long been used for the study of turbulence. Current research involves the use of balloon-borne fine-wire instruments to make in-situ measurements of stratospheric turbulence. These measurements are needed to characterize the turbulence through which hypersonic cruise vehicles will fly. In the stratosphere, fine-wires experience Knudsen number values in the transition regime between slip-flow and free-molecular flow. Fine-wire instruments have seldom been used to study turbulence in transition regime conditions. Energy transfer models for fine-wires in this new class of flow must be developed and validated, and a thorough phenomenological understanding of these instruments is required to accurately process and interpret collected data. This document presents results from a numerical study of fine-wires in low-speed, transition regime flows.

A review of numerical methodologies for simulating transition regime flow is presented. Direct Boltzmann Solvers appear most suited for low-speed transition regime simulations, however, there is no readily available software, and much development is needed before a code could be applied to general problems. The direct simulation Monte Carlo (DSMC) method remains the most accurate, generally applicable, and available method for transition regime simulations. Therefore, the DSMC method serves as the primary simulation tool for this work.

The DSMC method is well suited for simulations of high-speed flows. However, care must be taken in the choice of boundary conditions for low-speed DSMC simulations. Analysis and discussion of boundary conditions for low-speed DSMC simulations is included. A target mass flow rate boundary condition for low-speed DSMC is presented. Preliminary results show good performance, but further tuning and characterization are required before the method can be generally applied.

Results from low-speed DSMC simulations are shown to be strongly dependent on the computational domain size. This dependence is due to thermal conduction between the wire surface and domain boundaries which dominates the energy transfer due to forced convection when the computational domain is too small. Convergence is not achieved even for domain sizes that push the limits of an available supercomputer resource. The dependence of simulated fine-wire power loss is characterized with respect to simulated Reynolds and Knudsen numbers. A domain convergence extrapolation method to correct results for the domain size effect is discussed, though results show that the method can produce unrealistic corrections at lower simulated velocities.

A thorough investigation of the fine-wire parameter space is conducted. The sensitivity of wire power loss with respect to Knudsen number, flow speed, surface accommodation coefficient, gas composition, and temperatures is explored. Results validate the use of a previously derived empirical models for analysis of data collected to-date in the HYFLITS research campaign. However, it is shown that empirical models diverge significantly from simulation results for Knudsen number values above 2 or altitudes above about 35 km. Measurements made at these higher altitudes would require new energy transfer models to analyze data.

Comparisons with free-molecular theory are used to validate simulations of high Knudsen number flows. It is observed that the derivative of power loss with respect to velocity at low Reynolds numbers is positive in the continuum regime but negative in the free-molecular regime. In agreement with this observation, simulation results show a decrease in power loss sensitivity with respect to velocity as Knudsen number increases. Insensitivity of power loss with respect to flow speed represents a fundamental limitation of thermal anemometry for sensing flow speed in the transition regime. It is predicted that this would occur at some altitude between 40 and 50 km for the HYFLITS measurement system, but further studies are required to more precisely characterize where this insensitivity occurs.

Finally, the temperature jump around fine-wires through the transition regime is investigated. As could be expected, simulation data show that temperature jump increases through the transition regime to the point where the temperature of the gas surrounding the wire is equal to the free-

stream and unaffected by the presence of the wire. This suggests that classical energy transfer models based on evaluating fluid properties at the film temperature are not appropriate and may introduce significant errors for fine-wires with a high temperature loading. An empirical model for temperature jump derived from simulation data is presented and analyzed. Applicability of the model over a range of wire temperatures, gas compositions, surface accommodation coefficients, and flow velocities is demonstrated. When temperature loading is sufficiently high, the presented model can be used to calculate fluid properties at the appropriate temperature throughout the transition regime.

Results presented expand the current knowledge of fine-wire power loss in the transition regime and have immediate implications for the analysis of turbulence data currently being collected for the HYFLITS measurement campaign.

Dedication

To my wife, Samantha, my children, Emelia and David, and my Savior, Jesus Christ.

Acknowledgements

I would like to acknowledge my advisor, Dr. Brian Argrow, and Dr. Dale Lawrence for the technical guidance and funding that made this work possible. I also would like to acknowledge my lab mates Joseph Pointer, Sara Swenson, Robert Sasse, and Nicholas Campbell whose camaraderie and collaboration over these last few years has been invaluable.

Contents

Chapter

Tables

Table

Figures

Figure

Chapter 1

Introduction

1.1 Motivation for Low-Speed Rarefied Gas Simulations

Cruising hypersonic vehicles will fly at altitudes between 18 and 40 km. It has been shown that free stream turbulence can affect the laminar to turbulent transition of hypersonic boundary layers [50, 40]. The Hypersonic Flight in the Turbulent Stratosphere (HYFLITS) research campaign, supported by the Air Force Office of Scientific Research (AFOSR) Multidisciplinary University Research Initiative (MURI), is making in-situ measurements of stratospheric turbulence with balloon-borne fine-wire instruments. Fine-wires have long been used to measure turbulent fluctuations of velocity and temperature. Calibration of these instruments is a crucial step in this research effort. Balloon-borne instruments will experience mean flow rates between 1 and 10 m/s while collecting data. Corresponding fine-wire Reynolds number (Re) values at the altitudes of interest have a wide range, $1.2 \times 10^{-3} < \mathrm{Re} < 4.2 \times 10^{-1}$. Low air density in the stratosphere results in fine-wire Knudsen number (Kn) values in the range $0.1 < \mathrm{Kn} < 4$ based on a wire diameter of $d = 5$ μm ($\mathrm{Kn} = \lambda/d$, where λ is the mean free path). These values correspond to the transition regime between slip-flow and free-molecular flow. Figure 1.1 shows balloon-borne fine-wire instrument flow conditions with altitude. Slip-flow, transition, and free-molecular flow regimes are highlighted.

Most fine-wire applications to date have had Kn values that lie in the continuum or slip-flow regimes. As fine-wire Kn values increase into the transition regime, heat transfer between the wire and the surrounding fluid changes significantly [16, 63]. Only recently has there been

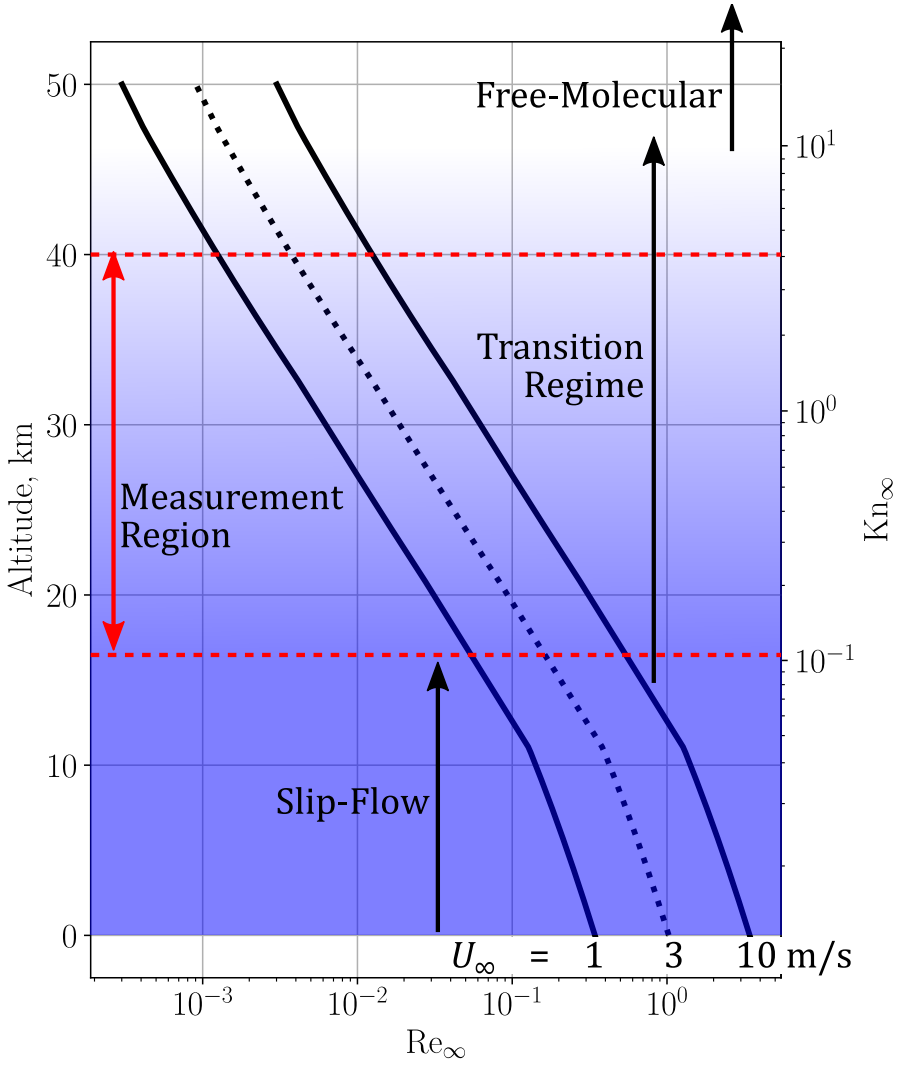

Figure 1.1: Plot showing conditions of balloon-borne fine-wire instruments for altitudes up to 50 km. Air properties are calculated using the 1976 Standard Atmosphere [1]. Kn and Re values are based on $d = 5$ μm. The measurement region of interest to the HYFLITS research campaign is indicated. Slip-flow, transition, and free-molecular regimes are highlighted.

demand for using fine-wires at rarefied conditions, so relatively few studies have investigated Kn dependence of fine-wire heat transfer for Kn values in the transition regime. The work presented addresses this knowledge gap by using numerical simulation to investigate power loss from fine-wires in the transition regime. Results help to address an immediate need for the HYFLITS research campaign: a thorough understanding of heat transfer for balloon-borne fine-wire instruments at altitudes between 18 and 40 km.

In addition to the immediate motivation from the HYFLITS campaign, there are at least two other notable applications of the current work. The first is for the simulation of fibrous thermal protection system (TPS) materials which are used on hypersonic reentry vehicles. Fibrous TPS materials are typically modeled as a matrix of randomly oriented micro cylinders [55, 49]. In flight, the fibrous TPS material, which is located in the vehicle boundary layer, experiences rarefied subsonic gas flow. The second application is microelectromechanical systems (MEMS). The small scale features of these systems can experience Kn values in the slip or transition regimes even at standard atmosphere conditions. Numerous studies have investigated subsonic rarefied flows in MEMS devices, but many of these are limited to enclosed systems such as channel flow [9, 20, 44, 57]. Results of the current study contribute useful insight about the simulation methods and physics of low-speed rarefied flows that could be applied to both these areas of work.

The remainder of this chapter presents an overview of fine-wire instruments and a review of the relevant literature. General background of fine-wire operation is provided in §1.2. A review of previously published research on fine-wire instruments is presented in §1.3. Particular focus is placed on publications that investigate fine-wires in low-speed, rarefied flows and numerical simulation studies of these instruments. Knowledge gaps in the field are highlighted in §1.4. The chapter finishes with a discussion of the current project in §1.5.

1.2 Fine-Wire Instrument Background

Fine-wire instruments consist of a thin wire suspended between two prongs. Figure 1.2 shows a schematic of a fine-wire instrument. Wires typically have diameters between 1 and 5 μm. During operation, a known voltage or current is applied to the wire. Small wire diameters and typical wire materials (platinum or tungsten) lead to the wire having a large resistance relative to the rest of the serial electrical components. Joule heating in the wire causes the wire temperature to be raised relative to the surrounding fluid. The working principle for these instruments is rooted in the power balance of the wire. If the thermal time response of the wire is negligible (which is often

the case because of the small wire diameters) the power balance can be written as

$$\dot{Q}_{gen} = \dot{Q}_c + \dot{Q}_r + \dot{Q}_h \tag{1.1}$$

where $\dot{Q}_{gen}$ is Joule heating in the wire, $\dot{Q}_c$ is conduction through the wire ends to the prongs, $\dot{Q}_r$ is radiation from the wire surface, and $\dot{Q}_h$ is the rate of heat transfer (power loss) to the surrounding fluid. All terms in Equation 1.1 have units of watt (W). The value for $\dot{Q}_h$ depends on properties of the surrounding fluid such as temperature and velocity. The convective heat transfer coefficient h is used to express the rate of convective heat transfer per unit surface area per unit temperature and is given by

$$h = \frac{\dot{Q}_h}{A_s(T_w - T_\infty)} \tag{1.2}$$

where T_w is the wire temperature, T_∞ is the free stream fluid temperature, and A_s is the surface area of the wire. The most common method of reporting power loss values for fine-wire instruments is in terms of the Nusselt number (Nu) which is given by

$$\mathrm{Nu} = \frac{hd}{k} \tag{1.3}$$

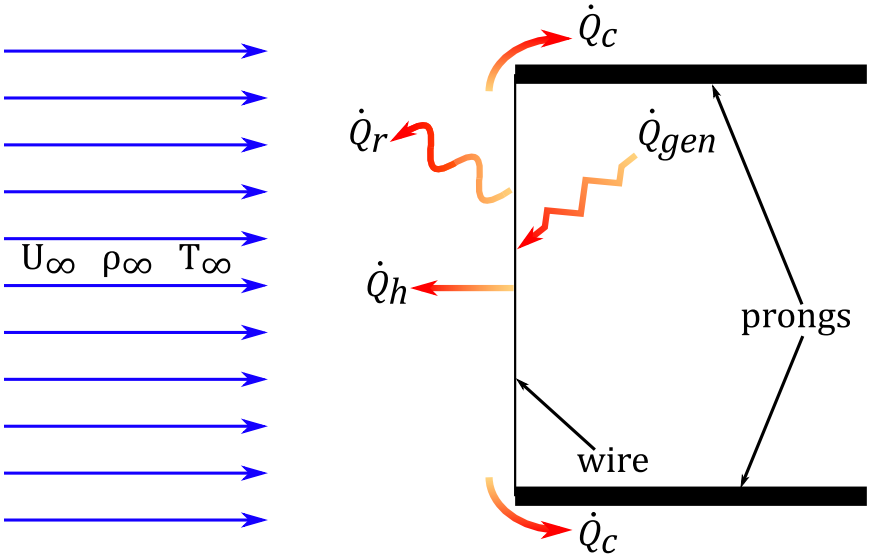

Figure 1.2: Schematic of a fine-wire instrument.

where k is thermal conductivity. Nu is the ratio of the total power loss from a surface to the rate of conductive heat transfer through the surrounding fluid.

Fundamentally, a fine-wire works by calibrating $\dot{Q}_h$ against a particular property of the surrounding fluid. This methodology requires a thorough understanding and accurate predictions of all other terms in Equation 1.1 ($\dot{Q}_{gen}$, $\dot{Q}_c$, and $\dot{Q}_r$). Joule heating can be expressed as a function of the electrical properties of the wire by

$$\dot{Q}_{gen} = I_w^2 R_w = E_w^2 / R_w \tag{1.4}$$

where I_w is electrical current through the wire, R_w is the wire resistance, and E_w is the voltage drop across the wire. Joule heating is readily calculated from known electrical properties of a fine-wire circuit. Any changes in the terms on the right hand side of Equation 1.1 can be sensed through subsequent changes in $\dot{Q}_{gen}$. Under many conditions, $\dot{Q}_c$ and $\dot{Q}_r$ are negligible relative to $\dot{Q}_h$. When this is the case, Equation 1.1 leads to the simple relation: $\dot{Q}_{gen} = \dot{Q}_h$. However, when $\dot{Q}_h$ is small, the relative significance of $\dot{Q}_c$ and $\dot{Q}_r$ increases. It has been shown that $\dot{Q}_c$ is significant for the fine-wires of interest to the current study [16, 52]. Precise modeling of $\dot{Q}_c$ and $\dot{Q}_r$ are not a focus of the current work, and has been addressed by several previous studies, and so will not be discussed here [16, 52]. The current work is focused on developing a precise understanding of $\dot{Q}_h$ in different flow conditions.

1.3 Previous Work

Many studies have investigated fine-wire power loss. The review presented here will mention a few key works for this field, and it will focus on studies that consider rarefaction effects and numerical simulation studies of heated cylinders.

A seminal work for hotwire anemometer power loss is that of [32] who first derived a relation (known as King's law) between wire heat transfer rate and streaming velocity. King's law can be expressed in non-dimensional form as

$$\mathrm{Nu} = A + B\mathrm{Re}^n \tag{1.5}$$

where Re is the wire Reynolds number and is given by

$$\mathrm{Re} = \frac{\rho U_\infty d}{\mu} \tag{1.6}$$

where ρ is the fluid density, μ is the fluid dynamic viscosity, and U_∞ is the free stream fluid velocity. Parameters A, B, and n are calibration constants. The original derivation in [32] suggested a value of 0.5 for n. This has been shown to be fairly accurate for $\mathrm{Re} \gtrsim 44$, the value at which vortex-shedding commences [15].

In [15], hotwires were experimentally investigated in low-Re flows. They propose a slightly different power loss model than [32] that includes an explicit dependence on the ratio of the film and free stream temperatures (T_f and T_∞, respectively). That model is given by

$$\mathrm{Nu}\left(\frac{T_f}{T_\infty}\right)^{-0.17} = A + B\mathrm{Re}^n. \tag{1.7}$$

The film temperature T_f is equal to the arithmetic mean of T_w and T_∞. Values for A, B, and n are different depending on whether Re is above or below the value at which vortex shedding occurs. The temperature ratio is included as a way of taking into account the fact that fluid properties are a function of temperature. Many studies to develop power loss models have not found it necessary to include an explicit temperature dependence. Instead they find that the effect of variable fluid properties is sufficiently captured by calculating non-dimensional quantities using fluid properties evaluated at the film temperature.

Fine-wires in low-Re flows and with Kn values in the slip to early transition regime were investigated in [14]. Oseen's theory for low-speed flow around a cylinder is compared with experimental data. As with most theoretical treatments of fine-wires, only small values of $T_w - T_\infty$ are considered. The expression for convective power loss that they derive from theory is

$$\mathrm{Nu} = \frac{2}{\log\left(\frac{8}{\mathrm{RePr}}\right) - \Gamma} \tag{1.8}$$

where Pr is the gas Prandtl number ($\mathrm{Pr} = \mu c_p/k$, where c_p is specific heat of the fluid) and Γ is Euler's constant ($\Gamma = 0.5772...$). Their experimental results differ from this theory as $\mathrm{Re} \to 0$.

They attribute this divergence to end-conduction ($\dot{Q}_c$) which was not taken into account. Though their data does extend into the transition regime, the authors make no attempt at investigating dependence of heat transfer on Kn.

Another theoretical model of Nu was derived in [31]. That expression is of a higher order than Equation 1.8, and it takes into account thermal and velocity slip at the wire surface. A subsequent experimental study shows moderate to good agreement with the theory [2]. While these results may be reasonable for slip-flow conditions, transition regime conditions were not considered.

In [5], hotwires with Kn values in the slip-flow regime are investigated. The relationship they propose has the same form as King's law (Equation 1.5) with $A = 0.34$, $B = 0.65$, and $n = 0.45$. The Nu value given by that model (referred to as the continuum Nu) differs from the measured value (Nu_m) because of thermal slip at the wire surface. The relationship between Nu and Nu_m is given as

$$\mathrm{Nu} = \frac{\mathrm{Nu}_m}{1 - \phi \mathrm{Kn} \mathrm{Nu}_m}. \tag{1.9}$$

Equation 1.9 is derived from kinetic theory and a first-order approximation of the temperature-jump boundary condition. The value for ϕ depends on the accommodation coefficient at the surface of the wire. A value of $\phi = 2$ successfully captured the slip affects seen in the experimental data of [5]. Equation 1.9 was also presented in [15], though they did not have enough experimental data to thoroughly expound upon its validity. A similar expression was derived in [31] and partially validated by [2].

Equation 1.9 is limited by the fact that its derivation depends on a first-order approximation of the thermal slip at the wire surface [17]. This assumption degrades at higher Kn values because property gradients are no longer linear over a distance approximately equal to the mean free path. Second-order slip boundary conditions were derived in [17]. Although these boundary conditions have not been used to derive solutions for fine-wire heat transfer, they show only a slight improvement over first-order boundary conditions in terms of the applicable range of Kn.

An experimental analysis of fine-wire heat transfer in transition regime air flows is presented

in [16]. They show a strong dependence of Nu on Kn in the transition regime and claim that this dependency increases with Re such that higher Re conditions converge to continuum behavior at lower Kn values. It is concluded that as Kn values approach the free-molecular regime, the value for Nu has no dependence on wire temperature, and significant dependence on wire temperature is observed as continuum conditions are approached. It is unclear the exact meaning of that conclusion, especially in light of free-molecular theory which shows an explicit dependence of wire heat transfer on the ratio of wire to free stream temperature ($T^* = T_w/T_\infty$, §3.3).

Dependence on Péclet Number Pe is also investigated in [16]. Pe is defined as

$$\mathrm{Pe} = \frac{Ud}{\alpha} = \frac{Ud}{k/(\rho c_p)} = \mathrm{RePr} \tag{1.10}$$

and represents the ratio of the advection time scale to the thermal diffusion time scale. Thermal diffusion becomes an increasingly dominant process for decreasing values of Pe. It was observed in [16] that King's Law is applicable for Pe > 10. This is a similar result to [15] who noted that a shift in the heat transfer relation between Re and Nu changes for Re values above that at which vortex shedding occurs (Re ≈ 44). Additionally, it can be seen from Equation 1.8 that the theory of [14] predicts a dependency on Pe. Despite the relatively large amount of transition regime data presented, no general relationship for fine-wire heat transfer in the transition regime is proposed in [16].

A thorough review of fine-wire data over a wide range of Re and Kn values is performed in [6]. That study presents a graphical model that covers Re values between 10^{-2} and 10^5 and Mach Numbers between 0 and 1. This corresponds to Kn values from 0 (continuum flow) to > 10 (free-molecular flow). While their model ostensibly covers a wide range of conditions, practical use of their model is difficult. The model is presented graphically on a log-log plot, and model lines are sparse for slip and transition regime conditions. The model and data presented can, however, serve as a good baseline for comparison with future results.

The dependence of heat transfer on wire temperature is also discussed in [6]. In continuum conditions, they note that non-dimensionalizing by film-temperature fluid properties appears to

effectively account for wire temperature effects. However, they point out that this approach is not effective, and even detrimental, in transition and free-molecular regimes. The models presented in [6] are based on evaluating fluid properties at the total free stream air temperature.

In [63], experimental heat transfer data for hotwires in the slip-flow and transition regimes are presented for velocities between 0.5 and 20 m/s ($10^{-3} < \mathrm{Kn} < 3$, $10^{-3} < \mathrm{Re} < 20$). In agreement with previous studies, their results show a clear decrease in Nu with increasing Kn. They present an empirical model for Nu as a function of Re and Kn given by

$$\mathrm{Nu} = A + B\mathrm{Re}^n + C\mathrm{Kn}^m + D\mathrm{Re}^i\mathrm{Kn}^j. \tag{1.11}$$

Values for the constants A, B, C, D, n, m, and i in Equation (1.11) are calculated using a non-linear least-squares fit to the experimental data. The empirical model presented by [63] is the only useful model for fine-wires in the transition regime that the author is aware of. However, the way in which the calibration parameters were calculated did not require that the model be a continuous function of Kn. Data were grouped into three different Kn regimes. The parameters of Equation 1.11 were then determined for each group of data. The predicted values of Nu for various Re over the full reported applicable range of Kn is shown in Figure 1.3. Values for the respective slope of Nu with respect to Re are shown in Figure 1.4. For each plot, lines of constant Re are only drawn where the conditions lie within the model boundaries given by the authors. The figures show that the models given in [63] may be useful for some limited engineering applications, but they do not represent a continuous description of fine-wire heat transfer for Kn values through the transition regime.

Relatively few numerical simulation investigations of fine-wire energy transfer have been conducted [7, 10, 18, 28, 30, 34, 38, 64]. The work of [18] is probably the first numerical simulation study of fine-wire instruments. The simulated velocity field was solved separately from the temperature field, making their results appropriate for low wire temperatures (cold-wires). Good agreement is seen with previous experimental data. Other numerical studies of fine-wires in the continuum regime show good agreement with experimental values [7, 30, 34]. Few numerical simulation studies

have considered rarefaction effects.

A numerical study of fine-wire instruments from slip-flow to near free-molecular flow was conducted by [65]. That study used an inner and outer solution approach. The region near the wall was treated using the linearized Bhatnager-Gross-Krook model equation. Flow far from the cylinder is modeled with the Oseen-Stokes equations. That study does not provide a thorough examination of wire energy transfer, and it only considers cases where $T_\infty = T_w$.

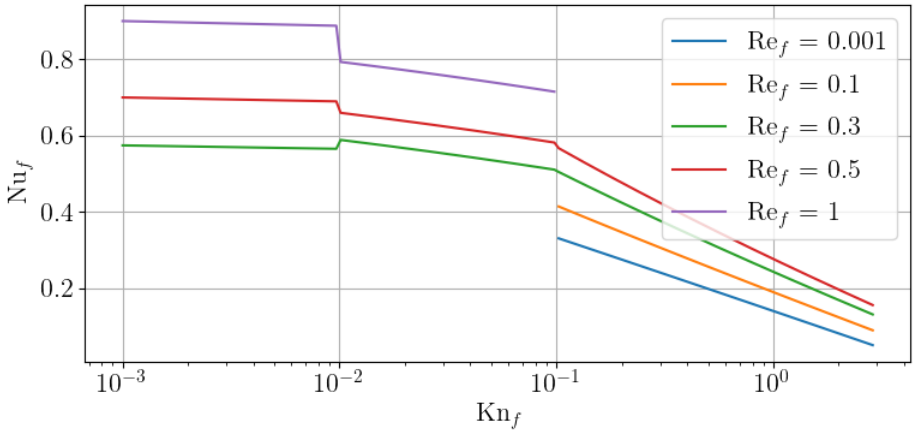

Figure 1.3: Power loss models of [63] for various Re values over the full range of applicable Kn values.

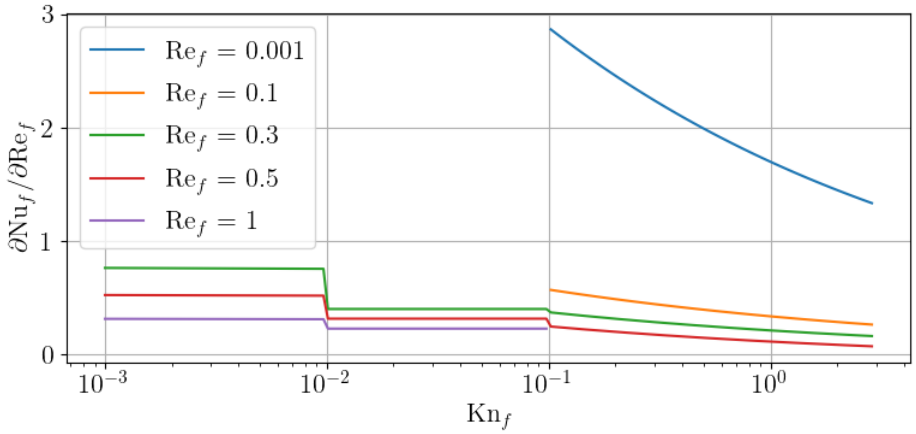

Figure 1.4: Derivative of power loss models from [63] for various Re values over the full range of applicable Kn values.

The vorticity transport and energy equations are solved numerically for laminar flow past a micro-cylinder in [38]. Velocity slip and temperature jump boundary conditions are used at the cylinder surface. Power loss dependence on Kn is explored for Kn values up 0.05. It is reported that results are within 10% of empirically derived models. They discuss the implication of rarefaction on fine-wire temperature sensors. It is shown that up to a 100% error in measured temperature may occur if temperature jump effects are not considered for the highest Kn and Re case investigated.

In [10], the direct simulation Monte Carlo (DSMC) method is used to explore cylinder energy transfer for Kn = 0.02 and 0.2. Cylinder Re ranged from 0.6 to 24. Rough agreement with previously published data is demonstrated. That study most closely resembles the numerical work presented here. Even though only a limited number of conditions were investigated, it serves to support the validity of the current work.

In [64], slip-flow boundary conditions are derived and implemented into the ANYSYS Fluent finite-volume computational fluid dynamics (CFD) solver. The study is limited to low wire temperatures relative to the free stream ($T_w - T_\infty \approx 1$ °C) to avoid implementing temperature-dependent fluid properties. At Kn < 0.1, simulation results show good agreement with experimental data and with several published Nu models. Numerical results diverge significantly from experiment for Kn > 0.1. This deviation from experimental data is caused by the inaccuracy of first-order slip boundary conditions when applied in the transition regime.

1.4 Knowledge Gaps

The relevant literature for the current project can be divided into two groups: studies that experimentally investigate fine-wire power loss near the conditions of interest, and numerical investigations of heated fine-wires. An overview of the literature in the former group is presented in Table 1.1. Also shown, for reference, is the present work. Three different studies reviewed here present data within the range of interest [6, 16, 63]. General energy transfer relations are only proposed in [6] and [63], and only that of [63] is practically useful.

The later group of literature, numerical investigations of fine-wires, is summarized in Table

1.2. Most of the studies to date have used CFD methods, limiting their possible region of applicability to the continuum and slip-flow regimes. The only known DSMC study of cylinder heat transfer near the flow regime of interest is [10]. A very limited set of conditions were explored in that study. Rough agreement with some experimental data is demonstrated, which further supports the feasibility of the current proposed work. Methods and models used in that study are similar to those of the current work, though the higher flow speeds investigated mitigate the finite domain effects that are important for the current flow regime of interest (Chapter 5).

To summarize, currently available fine-wire literature is lacking in two areas:

(1) A thorough understanding of transition regime fine-wire power loss

(2) Numerical simulation of heated cylinders in low-speed, transition regime flows

Table 1.1: Summary of key previous fine-wire power loss studies.

Study	**Re**	**Kn**
King 1914 [32]	$0.055 \rightarrow 55$	< 0.01
Cole and Roshko 1954 [14]	$0.01 \rightarrow 10$	$0.008 \rightarrow 0.26$
Collis and Williams 1959 [15]	$0.02 \rightarrow 140$	< 0.03
Baldwin et al. 1960 [6]	$10^{-2} \rightarrow 10^{5}$	$4.0 \times 10^{-6} \rightarrow 37$
Aihara et al. 1967 [2]	$3 \times 10^{-3} \rightarrow 2 \times 10^{-1}$	< 0.03
Andrews et al. 1972 [5]	$0.015 \rightarrow 20$	$0.003 \rightarrow 0.12$
Davis and Davies 1972 [16]	$0 \rightarrow 5.12$	$0.01 \rightarrow 10$
Xie et al. 2017 [63]	$10^{-3} \rightarrow 20$	$1.0 \times 10^{-3} \rightarrow 3$
Current Work	$0 \rightarrow 0.2$	$0.3 \rightarrow 30$

Table 1.2: Table summarizing previous simulation studies of low-speed flow over heated cylinders. No value for Kn is provided for studies that do not consider rarefaction.

Study	**Re**	**Kn**	**Method**
Dennis et al. 1968 [18]	$0.01 \rightarrow 40$		CFD
Karniadakis 1988 [30]	$20 \rightarrow 200$		CFD
Lange et al. 1998 [34]	$10^{-4} \rightarrow 200$		CFD
Bharti et al. 2006 [7]	$10 \rightarrow 45$		CFD
Maghsoudi et al. 2013 [38]	$10 \rightarrow 40$	$0 \rightarrow 0.05$	CFD with Slip BCs
Çelenligil 2016 [10]	$0.626 \rightarrow 24.63$	0.02 & 0.2	DSMC
Xie et al. 2018 [64]	$10^{-3} \rightarrow 20$	$0.01 \rightarrow 0.1$	CFD with Slip BCs
Current Work	$0 \rightarrow 0.2$	$0.2 \rightarrow 30$	DSMC

The first knowledge gap is critical for the HYFLITS campaign. The current work represents the most thorough numerical study of low-speed heated cylinders to-date, satisfying the second knowledge gap. Presented results and analyses help satisfy the first.

1.5 Current Work

The current work seeks to answer the following two research questions which arise from the need for measurements of stratospheric turbulence.

(1) Can current empirical models for transition regime wire power loss be accurately used for analyzing data from fine-wires in the stratosphere?

(2) How does power loss depend on free stream velocity for fine-wires from the transition regime to the free-molecular flow regime?

To answer these questions, a thorough investigation of power loss from fine-wires in transition regime flows has been conducted. This document presents results from that numerical study. The new information provided by this work has direct implications for the processing and analyzing of data that has been collected by the HYFLITS research campaign using balloon-borne fine-wires. Scientific and engineering contributions of the current work include:

(1) Development of an implicit target mass flow boundary condition for low-speed DSMC (Chapter 4)

(2) Evaluation of simulation accuracy for predicting fine-wire power loss in low-speed rarefied flows (Chapter 5)

(3) Verification of an empirical power loss model for fine-wires in the transition regime (Chapter 6)

(4) Characterization of fine-wire power loss from the transition to free-molecular flow regimes (Chapter 6)

(5) Empirical model for fine-wire temperature jump from the transition to free-molecular flow regimes (Chapter 7)

Chapter 2

Simulation Methods for Low-Speed Rarefied Flows

2.1 Overview

The previous chapter motivated the need for investigations of low-speed rarefied flows. Numerical simulations of these flows allow for the characterization of many details that are difficult or impossible to study experimentally. This chapter presents an overview of currently available simulation methods for low-speed rarefied flows. For each of the methods below, the current state-of-the-art is discussed, results from key studies are presented, and the future potential of each method is opined by the author.

All rarefied flow simulation methodologies seek to find or approximate solutions to the Boltzmann equation which, for a simple dilute gas, can be written as

$$\frac{\partial(nf)}{\partial t} + \boldsymbol{c} \cdot \frac{\partial(nf)}{\partial \boldsymbol{r}} + \boldsymbol{F} \cdot \frac{\partial(nf)}{\partial \boldsymbol{c}} = \int_{-\infty}^{\infty} \int_{0}^{4\pi} n^2 \left(f^* f_1^* - f f_1 \right) c_r \sigma \, \mathrm{d}\Omega \, \mathrm{d}\boldsymbol{c}_1 \tag{2.1}$$

where f is the velocity distribution function, n is the number density, $\boldsymbol{c}$ is the velocity vector, $\boldsymbol{r}$ is the position vector, $\boldsymbol{F}$ is the force vector per unit mass, and the right hand side is the collision integral. The Boltzmann equation is a model of the number density of a particular molecular species in six-dimensional phase space, which consists of both physical space and velocity space. The first term represents the time rate of change of the number density in the particular volume of phase space. The second term represents the convection of particles into or out of the particular volume of physical space due to the local velocity $\boldsymbol{c}$. The third term represents the movement of particles into and out of the particular volume of velocity space due to the acceleration of the gas by some

body force. The term on the right hand side is known as the collision operator and represents the rate of change of particles in the particular velocity space element caused by intermolecular collisions. A thorough mathematical derivation of the collision operator can be found elsewhere [8].

2.2 Simulation Methods

2.2.1 Moment Methods

One approach to the simulation of rarefied gas flows is to derive macroscopic transport equations for this flow regime [56]. These equations are derived by taking moments of the Boltzmann equation. The seminal work for moment based methods is [24]. In that work, a governing set of 13 moment equations were derived and are known as Grad's 13 moment equations. Some implementations of the method of moments have been shown to be accurate up to Kn values of ~ 1 [26]. This is only a slight improvement over CFD with slip boundary conditions which consistently reports accurate results for Kn values up to 0.1. Moment based methods are appealing because of their computational efficiency relative to particle based or direct simulation methods. Current work requires fine-wire simulations for Kn values up to 4, exceeding the range of applicable Kn for the current state of moment based methods.

2.2.2 Direct Boltzmann Solver

Another approach to simulating rarefied flows is to numerically solve the Boltzmann equation over discretized phase space [22, 29, 46, 62]. These methods are similar, in principle, to Navier-Stokes CFD for continuum flow, but velocity space, in addition to physical space, must be discretized. Additional mathematical and numerical challenges arise from the fact that Equation 2.1 is an integro-differential equation, rather than simply a differential equation as in the case of the Navier-Stokes equations. Recent studies have proposed discretizing velocity space using spectral methods to efficiently compute the collision term of the Boltzmann equation, while time and space are discretized in manners similar to classical CFD methods: Runge-Kutta for time and either

Finite-Volume, Finite-Difference, or Finite-Element for space [22, 29, 46]. Recent implementations have shown very good agreement with DSMC [29]. As these methods are based on solving partial differential equations, they can be more computationally efficient than DSMC. This is especially true for low-speed flows where the velocity space can be well-predicted and has a relatively small range. The computational cost of direct solvers grows significantly as the range of velocities in a given simulation becomes large, as is the case with high-speed flows over bodies. Some of these methods have been developed, but only primitive versions exist and significant development is required before they can be generally applied.

2.2.3 Lattice Boltzmann Method

The lattice Boltzmann (LB) method is derived from a Hermite polynomial expansion of the Boltzmann equation [33]. In essence, the method models the minimal amount of molecular physics in order that averaged macroscopic properties obey desired macroscopic conservation equations. This method is computationally efficient relative to DSMC, but challenges arise when applying it to higher Kn flows. Until recently, the LB method has not been able to capture Kn layers for transition regime flows because of inadequate boundary conditions [27, 67]. Improvements have been made, but recent models have not been thoroughly validated or implemented into readily available codes [35, 37].

2.2.4 Discrete Velocity Methods

Discrete velocity methods (DVM) are similar to DSMC in that numerical particles are tracked and collided in a stochastic manner. However, instead of allowing for arbitrary particle velocities, only a discrete number of velocities are simulated [41, 42, 66]. As an example, a recently proposed method called quasi-particle simulation (QuiPS) is currently under development at The University of Texas at Austin [13, 43, 48]. The numerical particles simulated may have only a discrete number of velocities, but they have variable mass. During a collision, mass is transferred between particles that have different velocities. The primary motivation for development of QuiPS (and other DVM

codes) is the reduction of statistical scatter and the accurate modeling of trace particles [45]. Discrete velocity methods have shown reduced statistical scatter and computational cost relative to DSMC.

2.2.5 Direct Simulation Monte Carlo Method

The DSMC method, pioneered by Graeme Bird, simulates dilute gases by tracking a finite number of representative gas particles within a domain [8]. Particles are moved according to their individual velocity and a time-step Δt. Particles are collided with each other stochastically. These movement and collision steps are repeated for each time-step of a simulation until some specified time has been reached. The DSMC method has been widely used over the last few decades for applications ranging from the simulation hypersonic reentry vehicles to channel flow through microelectromechanical systems. The method is theoretically applicable for Kn values ranging from the continuum to the free-molecular regimes. Computational cost, however, scales inversely with Kn number, making most continuum and many slip-flow simulations impossible with current computational resources. Particular challenges also arise when using DSMC for low-speed flows. These include statistical scatter and boundary conditions. Statistical scatter arises from the fact that DSMC stochastically simulates particles which travel at the thermal speed of a gas. As average velocity decreases, the signal (average flow velocity) to noise (thermal speed of particles) ratio decreases. An easy and popular solution to the problem of statistical scatter is to increase the density of simulated particles. This, however, increases the computational cost accordingly. The treatment of boundaries in low-speed DSMC is also challenging relative to high speed simulations. In the high speed case, inlet conditions are accurately modeled as equilibrium boundaries while the outlet can be simply treated as a vacuum because speeds are high enough that the flux of particles into the domain through the outlet can be entirely ignored. For low-speed flows, the flux of particles from all sides of the domain must be considered. Equilibrium boundaries are still appropriate where conditions are confidently known, but at boundaries where conditions are not known a priori, the flux of particles into the domain must be determined implicitly from the DSMC solution as it

progresses through time. These implicit boundary methods are sensitive to the statistical scatter of collision cell data. Despite these challenges, DSMC is the most popular simulation method for transition regime flows at all flow speeds because of widely available simulation codes, thoroughly validated models, and physical accuracy across a wide range of conditions.

2.2.6 Information Preserving DSMC

The velocity of a particle in a particular volume of fluid can be thought of as containing two different components, the bulk speed of the surrounding particles and the thermal speed of that individual molecule. The statistical distribution of the thermal speed of molecules in a volume is a function of the thermal temperature of that volume of fluid. For a volume that is in equilibrium, that functional relationship is given by the Maxwell-Boltzmann distribution. Several studies have presented information preserving DSMC (IP-DSMC) methods for reducing the statistical scatter of low-speed simulations [9, 20, 54, 58, 59]. These methods seek to reduce the statistical scatter by preserving information about the macroscopic flow variables such as velocity, temperature, and density. The basic idea for IP-DSMC lies in the decomposition of flow properties into macroscopic flow properties and random thermal properties. Individual particles are tracked and moved in the same manner as is done in traditional DSMC. Macroscopic flow properties are stored at the particle and/or cell level and are updated according to some conservation law such as the Euler Equations. The treatment of energy flux at walls and between collision cells is non-trivial [58, 59]. While IP-DSMC has been shown to effectively reduce statistical scatter and efficiency of low-speed DSMC simulations, the method is not widely used and no implementation of the method is readily available.

2.3 Summary and Conclusions

Many different methods have been developed for the simulation of rarefied flows. In theory, a Direct Boltzmann Solver would seem to be the best candidate for simulating flow over a heated fine-wire. The computational cost of Direct Boltzmann solvers decrease with the simulated velocity

because velocity space subsequently reduces in size. This is the opposite trend of DSMC where statistical scatter at low-speeds requires more simulated particles and, therefore, higher computational cost. Unfortunately, no known Direct Boltzmann Solvers are readily available or are capable of simulating the flow of interest. Despite the challenges of applying DSMC to low-speed flows, it is the most widely available and most popular method for simulating the transition regime at all flow conditions. The method is well validated and physically accurate. For these reasons, the DSMC method serves as the primary modeling tool for the current work, although future studies should consider using some of the other methods discussed as they increase in maturity and general applicability. Chapter 3 presents the details of the DSMC simulations performed for this study.

Chapter 3

Numerical Simulation Methodology

3.1 Overview

The current study utilizes the DSMC method and kinetic theory for free-molecular flow to simulate fine-wires in rarefied flows. Ideal gas behavior is assumed for all simulations and experimental data discussed in this work. The DSMC method is used for simulating the transition and free-molecular regimes. Theory for free-molecular flow is used to validate DSMC results at high values of Kn. Details about each of these methods are discussed in this chapter.

3.2 Direct Simulation Monte Carlo

Simulations of the current work were run with the open source DSMC code SPARTA developed by Sandia National Laboratory (Stochastic PArallel Rarefied-gas Time-accurate Analyzer, http://sparta.sandia.gov) [47]. This code is continually updated and well documented. It represents the current state-of-the-art for computationally efficient DSMC software. Simulations using this code were run on the RMACC Summit supercomputer and utilized as many as 660 total processors.

3.2.1 Simulation Domain Construction

Figure 3.1 shows a schematic of the DSMC domain used in the current study. The reflective wall serves as a symmetry plane. Some results were produced with a domain that included the entire wire and did not have a symmetry plane. For all simulations, $L_{inlet} = L_{top}$. Various values of L_{outlet} were used.

Collision cells are uniformly spaced in the x (streaming) and y directions of the computational domain. Collision cell width and height (ΔL_c) are set to less than half of the mean free path ($\Delta L_c \approx \lambda/2.1$). Simulation time-steps were set so that a particle traveling at the free stream temperature thermal speed ($\overline{v}$) travels less than half a collision cell width in one time-step ($\Delta t = 0.4\,\Delta L_c/\overline{v}$). Average particle thermal speed was calculated as

$$\overline{v} = \sqrt{\frac{8R_{gas}T_\infty}{\pi}}. \tag{3.1}$$

The ratio of real to simulated particles (f_{num}) was calculated by

$$f_{num} = \frac{n\Delta V_c}{N_{ppc}} \tag{3.2}$$

where n is the gas number density, ΔV_c is the collision cell volume, and N_{ppc} is the desired number of particles per cell. Most simulations are setup with $N_{ppc} = 100$, though some earlier simulations used $N_{ppc} = 10$. Negligible difference is observed between the average results of these two different particle counts, but the higher simulated particle density significantly reduces the statistical scatter of results [51].

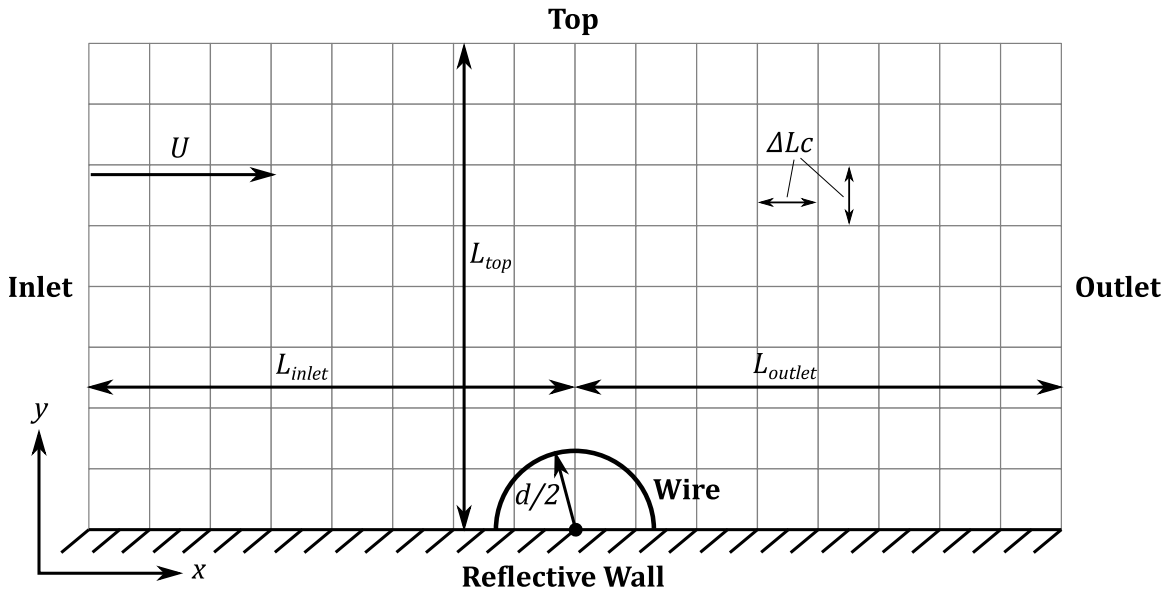

Figure 3.1: Schematic of the DSMC simulation domain used for the current study.

The variable soft-sphere model is used to model particle collisions. The corresponding equation for mean free path, as derived from kinetic theory in [8], is given by

$$\lambda = \left[\sqrt{2}\pi d_{ref}^2 n \left(\frac{T_{ref}}{T}\right)^{\omega-1/2}\right]^{-1} \tag{3.3}$$

where d_{ref} is the reference collision diameter for the gas, n is the number density, T_{ref} is the reference temperature corresponding to d_{ref}, and ω is the temperature exponent for viscosity. The viscosity of a variable soft-sphere gas is given in [8] as

$$\mu = \frac{5(\alpha_s+1)(\alpha_s+2)\sqrt{\pi m k_B}(4k_B/m)^{(\nu)}T^{\omega}}{16\alpha_s\Gamma(4-\nu)(\sigma_{T,ref})(c_{r,ref}^{2\nu})} \tag{3.4}$$

where m is the molecular mass, k_B is the Boltzmann constant, $\sigma_{T,ref} = \pi d_{ref}^2$ is the reference condition collision cross section, $\nu = \omega - 1/2$, α_s is the angular scattering parameter, $\Gamma()$ is the gamma function, and $c_{r,ref}$ is the mean relative speed of particles at reference conditions and is given by

$$c_{r,ref} = \frac{2}{\sqrt{\pi}}\sqrt{\frac{4k_B T_{ref}}{m}}. \tag{3.5}$$

The thermal conductivity k is then given in terms of viscosity and the specific gas constant by

$$k = \frac{15}{4}\mu R_{gas}\left(\frac{4}{15}\frac{1}{\gamma-1} + \frac{3}{5}\right) \tag{3.6}$$

where R_{gas} is the specific gas constant, γ is the ratio of specific heats, and the term in parentheses is a form of Eucken's correction for polyatomic gases [19]. The above equations for λ, μ, and k along with the ideal gas law are used for calculating fluid properties for simulated gases.

Internal rotational energy is modeled while vibrational energy is ignored. SPARTA uses the no time counter algorithm for selecting collision partners. The Larsen-Borgnakke model is used with a constant rotational relaxation number to model the exchange of rotational and translational energy during collisions. Table 3.1 provides the parameters for collision models for various gas species used in this study.

Table 3.1: Parameters for the variable soft-sphere collision model and the Larsen-Borgnakke model used in the current work. d_{ref} is the collision diameter, ω is the temperature exponent for viscosity, T_{ref} is the reference temperature, α_s is the angular scattering parameter, ζ_{rot} is the number of rotational degrees of freedom, and Z_{rot} is the rotational relaxation number.

Gas Species	$\boldsymbol{d_{ref} \times 10^{10}}$**, m**	$\boldsymbol{\omega}$	$\boldsymbol{T_{ref}}$**, K**	$\boldsymbol{\alpha_s}$	$\boldsymbol{\zeta_{rot}}$	$\boldsymbol{1/Z_{rot}}$
Nitrogen, N_2	4.07	0.74	273.15	1.6	2	0.2
Oxygen, O_2	3.96	0.77	273.15	1.4	2	0.2
Argon, Ar	4.11	0.81	273.15	1.4	0	0

3.2.2 Statistical Scatter

As discussed in the previous chapter, low-speed DSMC simulations suffer from large statistical scatter because the method stochastically models particle thermal velocities which are typically ~ 300 m/s. Mean flow velocities of interest to the current study are < 10 m/s, resulting a very low signal to noise ratio. For simulations in this work, statistical scatter has been addressed by simply taking large sample sizes at steady state conditions. This method has proven sufficient for hotwire simulations where the signal to noise ratio is relatively high because of the high energy transfer between the surface and the gas. Cold-wire simulations, however, have a very low wire power loss which dramatically reduces the signal to noise ratio. Figures 3.2 and 3.3 show the typical evolution of the rate of energy transfer for hotwire ($T_w - T_\infty = 100°$C) and cold-wire ($T_w - T_\infty = 4°$C) simulations, respectively. Both simulations are run with free stream temperature and pressure equal to that at 25 km altitude and a free stream velocity of $U_\infty = 2$ m/s [1]. Simulation domain size and boundary conditions are also identical. Significantly higher scatter is observed for the cold-wire simulations.

One method for reducing statistical scatter is to run an ensemble of simulation instances, each with a unique random number seed. Running ensembles of DSMC simulations is most useful when unsteady, time-accurate data is of interest because each simulation of the ensemble provides statistically independent data at each time-step. For the current work, statistical scatter was reduced by increasing simulated particle density and by ensuring a sufficient amount of steady state data was obtained for each simulation.

The relatively high computational cost of the scatter reducing methods used in the current work has pushed the limits of available computational resources because computational cost scales with the number of simulated particles. Additionally, simulation run-times are limited on the available supercomputer resource (RMACC Summit). Because of these limitations, most of the data presented here is for hotwires where the simulation scatter is reasonable. Some cold-wire data is shown, but uncertainty of results makes it difficult to draw strong conclusions from the data.

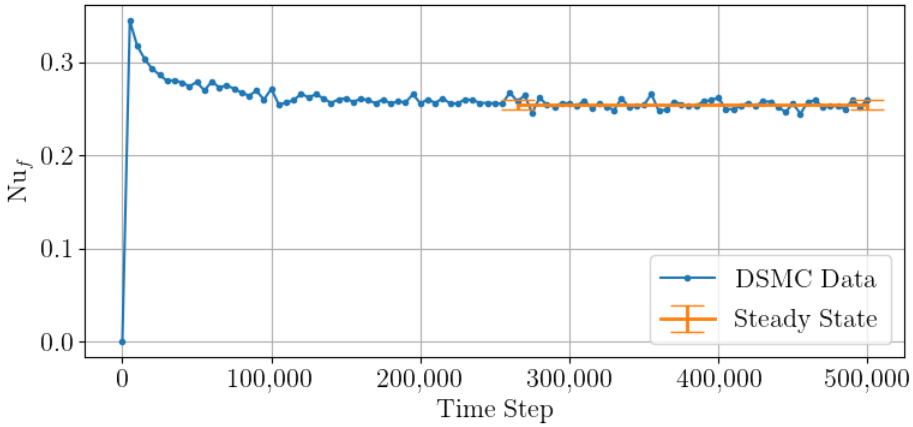

Figure 3.2: Typical time dependent results of wire power loss for a hotwire ($T_w - T_\infty = 100$ °C) DSMC simulation. The solid orange line shows the average of the steady state data (§3.2.4) and $\pm 1\sigma$.

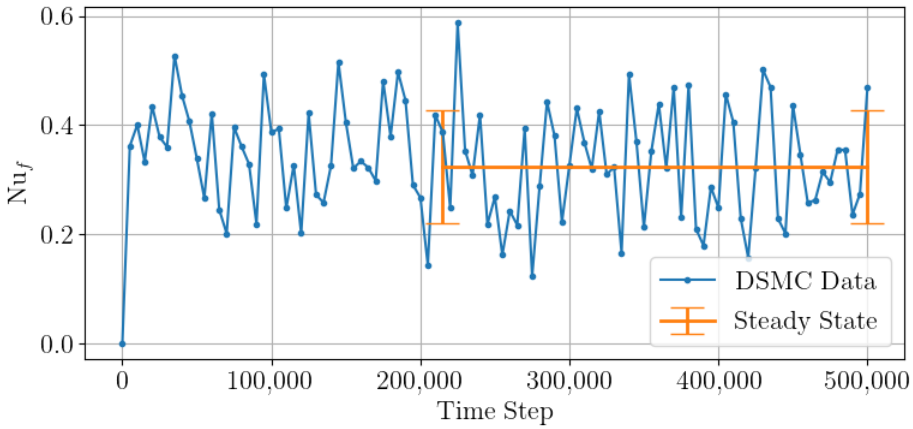

Figure 3.3: Typical time dependent results of wire power loss for cold-wire ($T_w - T_\infty = 4$ °C) DSMC simulation. The solid orange line shows the average of the steady state data (§3.2.4) and $\pm 1\sigma$.

3.2.3 Simulated Particle Density

In addition to statistical scatter of simulation results, low signal to noise ratio in DSMC simulations may result in insufficiently modeling the particle thermal velocity distribution, leading to erroneous results [60]. Typical recommendations for the number of simulated particles per-collision-cell in DSMC simulations is ≈ 10. This recommendation is largely based on supersonic and hypersonic simulations where the Maxwellian distribution is narrow relative to the free stream velocity. The relatively slim thermal velocity distribution can be easily captured with $N_{ppc} \approx 10$. At low velocities, however, the Maxwellian thermal velocity distribution is very wide relative to the free stream velocity. It can be expected that a higher density of simulated particles will be required to sufficiently reproduce the Maxwellian distribution for low-speed flows. Dependence of wire energy transfer on the number of simulated particles was investigated by running simulations with varying values of N_{ppc}. Results are shown in Figure 3.4. Free stream velocity and temperature are 3 m/s and 300 K, respectively. Wire temperature and accommodation coefficient are 373.15 K and 0.85, respectively. Wire Kn_f is 0.65. A weak dependence on N_{ppc} is observed. Mean wire energy transfer is within 1% for all values of N_{ppc} tested. All mean values are within $\pm 1\sigma$ of the statistical scatter for the $N_{ppc} = 50$ case.

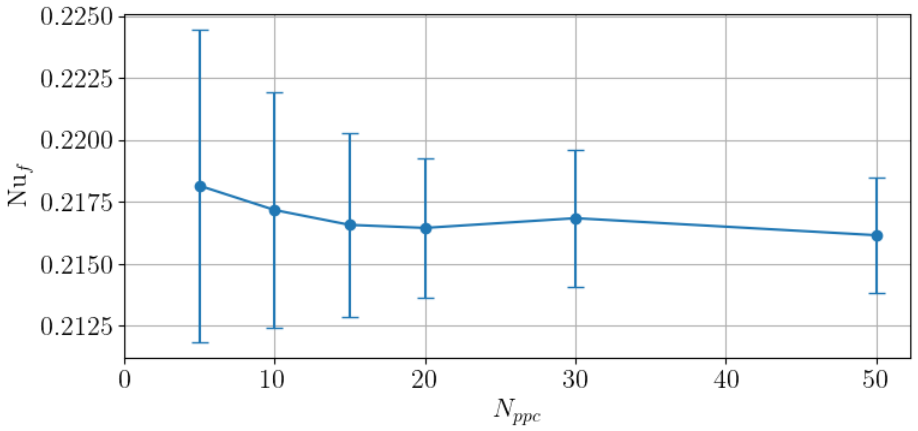

Figure 3.4: Dependence of hotwire Nusselt number on the number of simulated particles per-cell. Uncertainty bars indicate $\pm 1\sigma$ of the steady state DSMC data.

Other DSMC studies of subsonic flows have used N_{ppc} values ranging from 10 to 100 [10, 25, 39, 53, 57, 58, 60]. These studies typically use collision cell sizes that are approximately equal to the mean free path. Simulations performed for this work use collision cell sizes that are less than half of the mean free path. This results in about 40 simulated particles per square mean free path for the case where $N_{ppc} = 10$ (current simulations are two-dimensional) which is a similar simulated particle density to many previous studies. Simulated particle densities of $N_{ppc} = 10$ and 100 were used for results presented in the current work. Based on the results shown in Figure 3.4, minimal error for simulations with $N_{ppc} = 10$ is expected. A value of $N_{ppc} = 100$ has been used for many simulations to further reduce statistical scatter.

3.2.4 Determination of Steady State

In light of the statistical scatter of DSMC results, and to clarify the meaning of the data presented, a detailed description of the averaging and sampling procedures is warranted. During a DSMC simulation, numerical particles are moved throughout the domain and collide with one another in a stochastic manner. During the course of a simulation, SPARTA allows for data to be continually averaged and dumped every N time-steps. The data of primary interest to the current study is the energy transfer between the wire surface and the gas. Each data point of the time series shown in Figures 3.2 and 3.3 represents the average rate of energy transfer from the surface for the previous N time-steps. Lower values of N (higher sampling frequency) will result in more scatter in the output data than if a larger value of N is used (lower sampling frequency). For larger values of N, larger data sets are averaged for each output data point which effectively filters out the high-frequency, random fluctuations in the wire heat transfer rate. Fluctuations are filtered out more with increasing N. Preliminary simulations were run with a sampling frequency of $N = 1{,}000$ to establish a clear understanding of the time-variation of the heat transfer rate. Results presented here are from simulations that were run with $N = 5{,}000$, $10{,}000$, or $20{,}000$. Small sampling frequencies (large N) are desired to reduce the time spent writing results during the simulation, reduce the memory required to store the output data, and reduce the post-processing time.

Running simulations for longer times would allow for larger values of N to be used, leading to reduced statistical scatter. However, the frequency of output data must be high enough that the beginning of steady state can be confidently identified. Additionally, enough data must be dumped during steady state in order that meaningful statistical analysis of the results can be performed.

A simple algorithm has been developed to determine the section of steady state data from the time-history data like that shown in Figures 3.2 and 3.3. The algorithm follows the process enumerated below.

(1) Select entire time series of power loss data (t, Nu_f) as initial window of data

(2) Normalize the time t in the window of data to have a range between 0 and 1:

$$t^* = \frac{t - t_{min}}{t_{max} - t_{min}},\ 0 \leq t^* \leq 1 \tag{3.7}$$

(3) Calculate the average Nu_f in the data window ($\overline{\mathrm{Nu}_f}$)

(4) Express Nu_f values as a percent change from the window average:

$$\mathrm{Nu}_f^* = 100 \times \frac{\mathrm{Nu}_f - \overline{\mathrm{Nu}_f}}{\overline{\mathrm{Nu}_f}}$$

(5) Perform a linear regression analysis of the normalized data (t^*, Nu_f^*)

(6) Compare the slope of the linear fit $\mathrm{dNu}_f^*/\mathrm{d}t^*$ to the tolerance value of 1:

   (a) If $\mathrm{dNu}_f^*/\mathrm{d}t^* \geq 1$: remove first data point (where $t^* = 0$) from the current window of data and repeat steps 2–6

   (b) If $\mathrm{dNu}_f^*/\mathrm{d}t^* < 1$: current window is the estimated steady state section of data and the process ends

After the algorithm is completed, plots like those shown in Figures 3.2 and 3.3 are produced and visually inspected to check that the algorithm chose a reasonable set of steady state data. Effectively, the algorithm selects a set of data where a fitted line through that data does not predict more than 1% deviation from the data mean.

The DSMC data presented herein is given as a point with uncertainty bounds. These represent the average of the steady state period and one standard deviation of the steady state data ($\pm 1\sigma$). The uncertainty bounds are omitted when they are smaller or very close in size to the plot marker itself, or when they introduce unnecessary clutter that obscures the objective of a particular figure.

3.2.5 Allocation of Computational Resources

With the wide range of Kn values and various velocities simulated, the computational cost of different simulations performed for the current work varies widely. A procedure was developed to ensure that an appropriate amount of computational resources was used for each simulation. This procedure begins with estimating the amount of time it will take for a simulation to reach steady state. A typical estimation for steady state time in high speed flows is some multiple of the body flow time which is equal to body length divided by the mean flow speed. For the current simulations of heated fine-wires, estimating steady state using the wire diameter and the bulk flow speed results in a large under-prediction of the time to steady state. This is due to the fact that steady state is dependent on the entire domain reaching a steady state temperature. It was found that an effective, though somewhat conservative, approximation for steady state is to use the domain length and the mean flow speed to calculate the flow time as

$$t_{flow} = \frac{L_{inlet} + L_{outlet}}{U_\infty}. \tag{3.8}$$

The number of time-steps to run a simulation for was then calculated using the time-step Δt for that simulation.

Most DSMC simulations were run on the RMACC Summit supercomputer at CU Boulder [4]. The computational cost of the present simulations on that computer was characterized by running a number of simulations of various size and with various numbers of processors. The average wall-clock time per time-step was calculated for each simulation. This was found to be primarily a function of the number of simulated particles per processor. These data are shown in Figure 3.5.

Using the estimated number of simulated particles, the estimated number of steps to steady

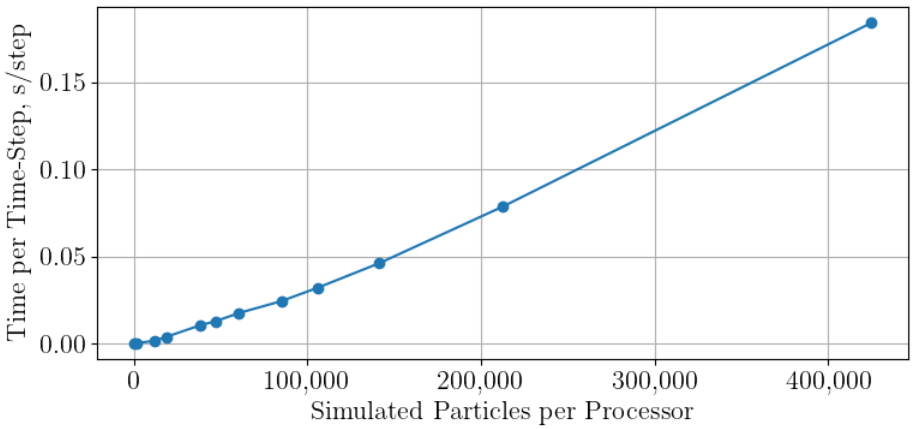

Figure 3.5: Computational cost of the present fine-wire simulations shown in terms of the wall-clock time to run a single time-step vs. the number of simulated particles per processor. Data shown are from simulations run on the RMACC Summit supercomputer.

state, and the data shown in Figure 3.5, computational resources were efficiently allocated for each simulation run. This systematic process allowed for hundreds of simulations to be run on the Summit computer with minimal overhead.

3.3 Kinetic Theory for Free-Molecular Flow

At sufficiently high values of Kn, particle collisions can be ignored entirely. This regime is referred to as free-molecular or collisionless flow. Relatively simple and exact relations can be written for aerodynamic forces and energy transfer in this regime for a wide variety of flows. In [11], the rate of energy transfer $d\dot{Q}$ from a flat surface of area dA to the surrounding gas in free-molecular flow is given by

$$d\dot{Q} = -\alpha\rho_\infty RT_\infty\sqrt{\frac{RT_\infty}{2\pi}}\left(\left[S^2+\frac{\gamma}{\gamma-1}-\frac{\gamma+1}{2(\gamma-1)}T^*\right]\left\{e^{-(S\sin\theta)^2}\right.\right.$$
$$\left.\left.+\sqrt{\pi}(S\sin\theta)[1+\mathrm{erf}(S\sin\theta)]\right\}-\frac{1}{2}e^{-(S\sin\theta)^2}\right)dA \quad (3.9)$$

where α is the surface accommodation coefficient, γ is the ratio of specific heats, θ is the angle of surface element dA with respect to the streaming velocity U, $T^* = T_w/T_\infty$, and S is the molecular speed ratio, $S = U/\sqrt{2RT_\infty}$. A quick dimensional analysis of Equation 3.9 shows that there are 4

fundamental units (mass, length, temperature, and time) and 7 independent dimensional quantities ($\dot{Q}$, ρ_∞, R, T_∞, T_w, U, and A) which means that the expression can be written with $7 - 4 = 3$ dimensionless parameters. These parameters are in addition to α and γ which are also dimensionless problem-dependent parameters on which Equation 3.9 depends. Two obvious parameters to choose include the molecular speed ratio S and the temperature ratio $T^* = T_w/T_\infty$. The third parameter can be defined as

$$\dot{Q}^* = \frac{\dot{Q}}{A_s \rho c_p (T_w - T_\infty)\sqrt{2RT_\infty}} = \frac{h}{\rho c_p u'_m} \tag{3.10}$$

where A_s is the energy transfer surface area, $u'_m = \sqrt{2RT_\infty}$ is the most probable molecular speed, and c_p is the specific heat at constant pressure. This dimensionless expression for the rate of energy transfer represents the ratio of the total energy flux to the surface to the average molecular energy flux of the gas. This parameter is similar to the Stanton Number but uses the most probable molecular speed u'_m as the velocity scale in the denominator, rather than the bulk flow speed U. This gives $\dot{Q}^*$ the advantage of being well-defined for all flow velocities, whereas Stanton Number is ill-defined when bulk flow speed is zero. Rearranging, and using the relation $R = c_p(\gamma - 1)/\gamma$ for an ideal gas, Equation 3.9 can be written in terms of S, T^*, and $\dot{Q}^*$ as

$$d\dot{Q}^* = -\frac{\alpha}{\sqrt{4\pi}} \frac{\gamma - 1}{\gamma} \frac{1}{T^* - 1} f\left(S, T^*, \theta\right) \frac{dA}{A_s} \tag{3.11}$$

where $f\left(S, T^*, \theta\right)$ is equal to the quantity in parenthesis in Equation 3.9. The differential dA/A_s is specific to the geometry of interest. For the case of a two-dimensional circular cylinder, $A_s = \pi d$ and $dA = (d/2)d\theta$ for $0 \geq \theta > 2\pi$. This gives $dA/A_s = d\theta/2\pi$. This expression can then be used to calculate the free-molecular heat transfer for circular cylinders by numerically integrating for $0 \geq \theta > 2\pi$. Previous authors have taken the time to derive (quasi-) analytical solutions for the case of a circular cylinder. However, these solutions include modified Bessel functions, solutions for which can only be estimated numerically anyway. The author has therefore chosen to forgo the burden of deriving an explicit solution (that can still only be estimated numerically) in favor of

numerically integrating Equation 3.11. This integration is given by

$$\dot{Q}^* = -\frac{\alpha}{\sqrt{4\pi}} \frac{\gamma - 1}{\gamma} \frac{1}{T^* - 1} \sum_{i=0}^{N-1} f\left(S, T^*, i\frac{2\pi}{N}\right) \frac{\Delta\theta}{2\pi} \tag{3.12}$$

where N is the number of differential surface elements and $\Delta\theta = 2\pi/N$. For all calculations performed herein, $N = 2{,}000$ surface elements were used.

Since most fine-wire energy transfer data is presented in terms of Nu and Re, it is useful to put the solution for free-molecular flow in terms of these parameters. Nu can be written in terms of $\dot{Q}^*$ as

$$\mathrm{Nu} = \frac{\rho c_p u'_m d}{k} \dot{Q}^*. \tag{3.13}$$

This can be written in terms of other dimensionless parameters as

$$\mathrm{Nu} = \frac{\mathrm{RePr}}{S} \dot{Q}^* \tag{3.14}$$

where $\mathrm{Pr} = c_p\mu/k$ is Prandtl number. Note that all fluid properties for free-molecular calculations are evaluated at the free stream temperature T_∞ since it is only undisturbed free stream particles which collide with the wire surface. The quantities S and Re can be approximately related by

$$\mathrm{Re} = \sqrt{\frac{\pi\gamma}{2}} \frac{\mathrm{M}}{\mathrm{Kn}} = \sqrt{\pi} \frac{S}{\mathrm{Kn}} \tag{3.15}$$

where M is Mach number. The above relationship between Re, M, and Kn relies on a definition of mean free path λ based on a hard-sphere molecular model. The relation does not strictly hold when a different model for mean free path is used. Because of this nuance, free-molecular heat transfer results for the present study were calculated first in terms of $\dot{Q}^*$ using Equation 3.12, and then converted to Nu using either Equation 3.13 or 3.14. Reynolds number was calculated directly from known gas properties.

Expressing free-molecular heat transfer in terms of Nu and Re introduces the coefficients of thermal conductivity k and viscosity μ. Both of these phenomena, conductivity and viscosity, are due to intermolecular collisions which do not exist in free-molecular flows. This suggests that, while it can be done, the use of Nu and Re to describe heat transfer in the free-molecular regime

is not the most physically appropriate approach. This is further demonstrated when reconsidering the above dimensional analysis. When expressing heat transfer in terms of Nu and Re, k and μ are introduced into the parameter space. These two quantities are related by Equation 3.6, so this changes the dimensional analysis so that now there are 8 independent dimensional quantities and still only 4 fundamental units, leading to the need for $8 - 4 = 4$ dimensionless parameters. This suggests that the classical method of discussing heat transfer in terms of Nu and Re may not be the most physically appropriate dimensionless grouping for rarefied flows. Despite this observation, results of the current work will still be expressed in terms of Nu and Re because this is the classical approach and the current fine-wire analysis methodology for the HYFLITS campaign assumes this form (See Appendix A). Additionally, even with the unnecessarily expanded parameter space, the free-molecular solution for Nu is still readily calculated if all fluid properties are known.

Chapter 4

Boundary Conditions for Low-Speed DSMC

4.1 Overview

Low-speed DSMC simulations require that a flux of particles enter the domain from the outlet. This is different from high speed simulations where, generally speaking, flow speeds at the domain outlet are sufficiently large such that it can be accurately assumed that no particles enter the domain from the outlet. This is due to the fact that supersonic flows are hyperbolic, while subsonic flows are elliptic. This means, in particular, that outflow boundary conditions influence the overall flow field more as flow speed decreases. This chapter discusses boundary conditions for subsonic DSMC simulations and the implementation of a new boundary condition for DSMC.

4.2 Equilibrium Boundary Conditions

Equilibrium, or open, boundary conditions create a flux of particles into the domain according to the Maxwell-Boltzmann velocity distribution function for an equilibrium gas. Several different methods have been developed for implementing this method. The simplest method, and the one that is implemented in the SPARTA code, is to simply use the equation for number flux $\dot{N}$ through a plane of an equilibrium gas which is given in [8] as

$$\dot{N} = \frac{\beta}{2n\sqrt{\pi}} \left[\exp(-S^2 \cos^2\theta) + S\sqrt{\pi} \cos\theta \left\{ 1 + \operatorname{erf}(S\cos\theta) \right\} \right] \tag{4.1}$$

where n is number density, θ is the angle of the plane relative to the bulk flow speed U, and S is the molecular speed ratio ($S = U\beta = \frac{U}{\sqrt{2RT}}$). For the equilibrium flux method, Equation 4.1 is used

to calculate the number of particles to be introduced into the domain each time-step. Thermal velocity components are then assigned to those particles by sampling from the Maxwell-Boltzmann velocity distribution function for the temperature specified. It has been shown that this method of implementing equilibrium boundary conditions can introduce slight non-equilibrium effects because of the fact that it uses a fixed number flux at each time-step [61]. In reality, the number flux itself should follow a Poisson distribution. The surface flux method described above generates the correct average number flux, but not the correct distribution of number flux over time.

Another method of implementing equilibrium boundary conditions is with a so-called volume boundary condition. With this approach, particles are generated each time-step in some volume that sits immediately adjacent to the simulation domain. The particles are randomly located in this volume and given a velocity by sampling from the equilibrium distribution function. Particles in this volume are then moved in the same manner as normal DSMC particles. Only particles that enter the simulation domain are retained and tracked normally, all other particles are deleted. The volume boundary condition method produces the correct distribution of number flux into the domain, unlike the surface flux method. While the volume boundary method has been shown to be more accurate, the equilibrium surface flux method is used in the current work for all equilibrium, or open, boundaries because the volume method is not implemented in the SPARTA DSMC code. It is expected that the error introduced by using this method are negligible relative to other sources of uncertainty including the statistical scatter of DSMC results and the domain size bias that will be discussed in Chapter 5.

4.3 Piston Boundary Condition

The piston boundary condition was presented in [8] as a way to simulate a standing shock wave. This condition treats the outlet as a reflective moving wall. The only user input for this condition is the speed of the boundary. Because the wall is moving, particles actually collide with it some distance downstream of the domain. After they are reflected and moved back in the direction of the domain, particles which make it back inside the domain boundaries are retained and tracked

as normal, particles which do not make it back inside the domain are discarded. The result of this condition is an average particle speed at the boundary equal to the specified velocity at the wall. Thermal temperature at the boundary is not specified.

A piston boundary condition at the domain outlet was used for many simulations early in this work, including those used to produce data for [51]. Data produced with this outlet condition compared reasonably well with experimental data from [63]. However, the boundary condition is physically unreasonable as flow velocities approach zero. In fact, the SPARTA code does not allow a velocity of zero to be set for a piston boundary condition. The reason for this is that as velocity goes to zero, the boundary simply acts like a reflective wall. This means that it is effectively simulating two wires right next to each other, which is unrealistic and will introduce some error.

4.4 Implicit Boundary Conditions

One class of boundary conditions that have been used for subsonic DSMC are known as implicit boundary conditions [36, 44]. The principle behind these boundary conditions are to specify the static pressure at a boundary and determine the flux of particles into the domain that will achieve that specified pressure. These implicit boundary conditions can be thought of as applying a set of governing equations to ghost cells that exist immediately outside of the domain. Each collision cell on a boundary will have an accompanying ghost cell immediately outside of the boundary. The fluid properties of a ghost cell are determined by extrapolating from the properties of the adjacent DSMC cell. This extrapolation is performed using the one dimensional method of characteristics which is essentially a solution technique for the steady, one dimensional Euler equations. The equations governing the ghost cell properties are

$$\rho_e = \rho_j + \frac{P_e - P_j}{(a_j)^2} \tag{4.2}$$

$$u_e = u_j + \frac{P_j - P_e}{\rho_j a_j} \tag{4.3}$$

$$v_e = v_j \tag{4.4}$$

where ρ is density, P is pressure, a is sound speed, u is velocity normal to the boundary, and v is

velocity parallel to the boundary. Subscript e indicates properties at the exit, or the properties of the ghost cells immediately adjacent to the DSMC domain. Subscript j indicates properties of the DSMC cell. The ghost cell temperature T_e can then be determined using the ideal gas law

$$T_e = \frac{P_e}{n_e k_B} = \frac{m P_e}{\rho_e k_B} \tag{4.5}$$

where n is number density, m is molecular weight of the gas, and k_B is the Boltzmann constant. The assumptions made for this boundary condition are that the flow is locally adiabatic, inviscid, and close to a perfect gas. Typically, Equations 4.2 - 4.5 are applied to each boundary collision cell/ghost cell pair every time-step of the DSMC simulation. The properties of the ghost cells are then used to generate a flux of particles into the domain using one of the equilibrium flux methods described in §4.2. Thus the flux of particles into each boundary collision cell could be unique.

One of the challenges that occurs when applying the above boundary condition is the low signal to noise ratio that can occur for low-speed DSMC simulations. This can cause instantaneous collision cell property values to vary widely. When the scatter occurs in a boundary cell from which ghost cell data is calculated, the problem is magnified because it then causes an unrealistic flux of particles into the domain. To mitigate the influence of statistical scatter, time averaging was implemented into the subsonic boundary condition in the SPARTA DSMC code. For the averaging scheme, collision cell data is averaged over some specified number of time-steps N_t. At the end of each averaging period, Equations 4.2-4.5 are applied to update the ghost cell values. Ghost cell values remain constant during the next averaging period. It should be noted that this averaging scheme makes this boundary condition even more limited to steady state flows because the averaging will damp changes with time.

Simulations of a hotwire were carried out using the implicit boundary condition method with time averaging. The outlet pressure was set equal to the inlet pressure. The averaging and update interval was $N_t = 200$. Results for the temperature and horizontal velocity fields are are shown in Figures 4.1 and 4.2, respectively. Significant back-flow into the domain from the outlet is observed. To see if this was caused by scatter, additional simulations were run with $N_t = 2{,}000$,

but the steady state results were the same, indicating that statistical scatter is not the cause of the erroneous back-flow. The following section addresses this back-flow issue.

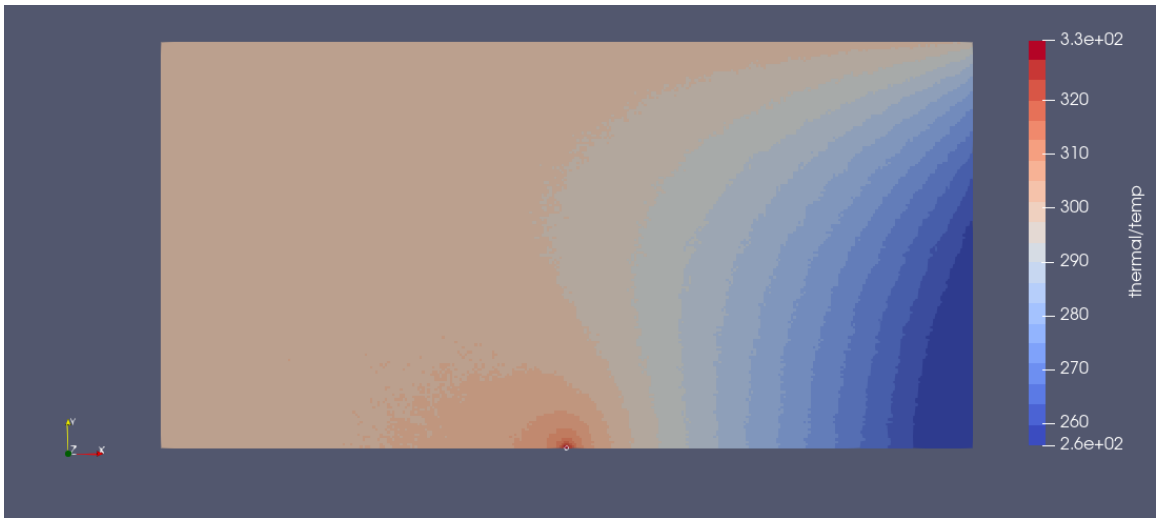

Figure 4.1: Temperature field for implicit boundary condition with time averaging collision cell data over 200 time-steps and updating ghost cell values at the same frequency. Temperature color scale is in K.

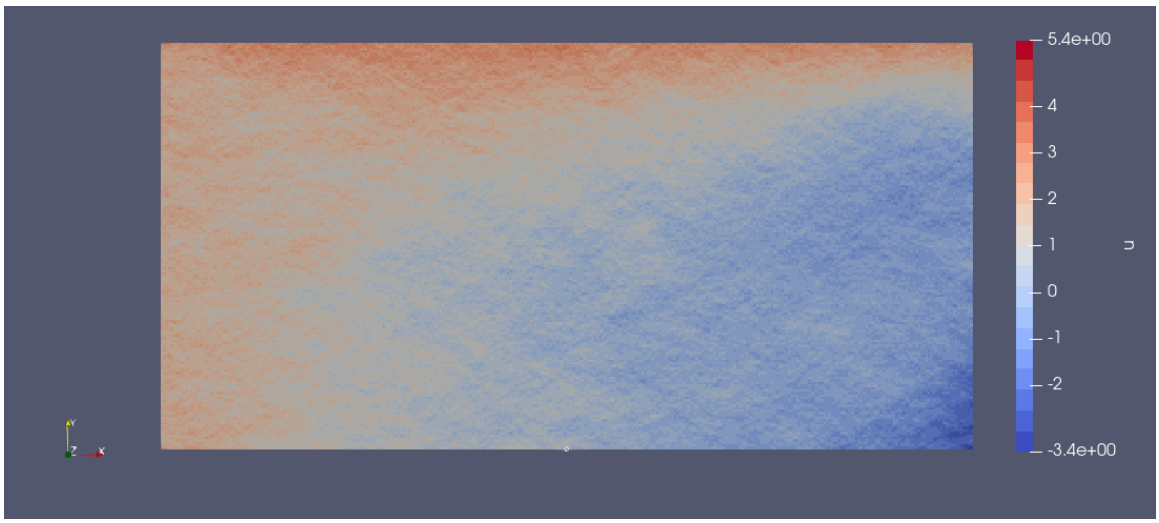

Figure 4.2: Horizontal velocity field for implicit boundary condition with time averaging collision cell data over 200 time-steps and updating ghost cell values at the same frequency. Velocity color scale is in m/s.

4.5 Target Mass Flow Rate

Implicit methods were primarily derived for use with pressure driven flows such as channel flow. For those simulations, the pressures at the inlet and outlet are known a priori, and so can be specified with confidence because they are a defining feature of the flow field. The simulation of a fine-wire is not such a case. Some unknown amount of pressure loss will occur from the inlet to the outlet because of the presence of the cylinder. This means that specifying the inlet pressure as being equal to the outlet pressure leads to an outlet pressure that is too high. Too high of an outlet pressure leads to a reversed pressure gradient at the boundary that forces gas into the domain from the outlet. It is therefore hypothesized that small errors in the specified outlet pressure cause the back-flow problem seen above. This hypothesis can be supported by considering the one dimensional and steady momentum equation for inviscid flow which can be written as

$$0 = -\frac{1}{\rho}\frac{\partial P}{\partial x} - u\frac{\partial u}{\partial x}. \tag{4.6}$$

Rearranging to solve for $\partial u/\partial x$ gives

$$\frac{\partial u}{\partial x} = -\frac{1}{\rho u}\frac{\partial P}{\partial x}. \tag{4.7}$$

This equation shows that as density and velocity (momentum) decrease, velocity becomes increasingly sensitive to changes in pressure. Considering changes in u and P over some arbitrary distance, one can write

$$\delta u = -\frac{1}{\rho u}\delta P. \tag{4.8}$$

This equation was evaluated using a value of $u = 3$ m/s and values of ρ corresponding to various altitudes. Results are shown in Figure 4.3. It is shown that changes in pressure less than 1 Pa can result in very significant changes in flow velocity for the low momentum flows of interest. This supports the hypothesis presented above which stated that small errors in the specified boundary pressure lead to significant acceleration or deceleration of the flow at the boundary. To address this issue for some applications, an iterative method for adjusting pressure at a boundary will now be presented.

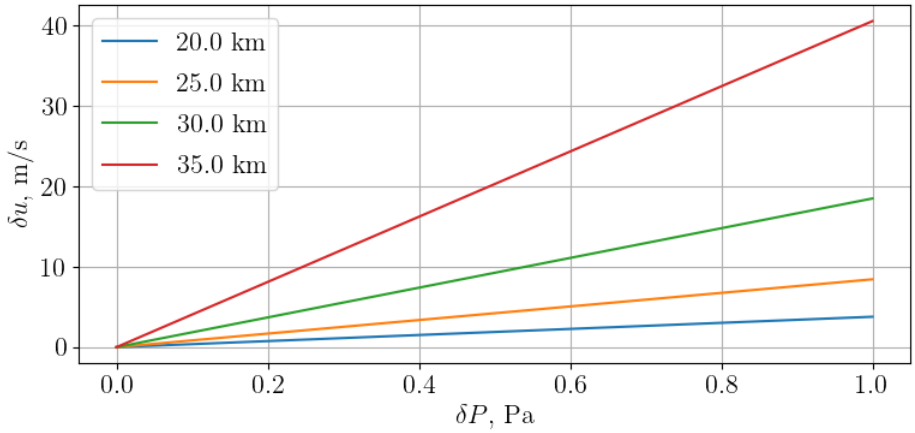

Figure 4.3: Sensitivity of changes in velocity to changes in pressure for various altitudes according to Equation 4.8.

Any iterative scheme for adjusting pressure must have some target that the iteration algorithm is attempting to reach. For many different steady state flow fields, the total mass flow rate through the system is known. This is particularly true for confined systems such as channel flows. It is therefore reasonable to specify a desired mass flow rate at a boundary. A relationship between mass flow rate and the specified boundary condition can be derived from Equation 4.8. Mass flow rate can be written in terms of velocity and density as

$$\dot{m} = \rho u A \tag{4.9}$$

where A is surface area of the boundary which is normal to u. Using Equation 4.9, Equation 4.8 can be written as

$$\frac{\delta \dot{m}}{\rho A} = -\frac{A}{\dot{m}} \delta P. \tag{4.10}$$

Rearranging gives

$$\delta P = -\frac{\dot{m}}{\rho A^2} \delta \dot{m}. \tag{4.11}$$

As should be expected, this says that increasing pressure at the boundary ($\delta P > 0$) causes a decrease in mass flow out of the boundary ($\delta \dot{m} < 0$) because of the introduced back pressure. Conversely, a decrease in pressure results in an increase in mass flow rate.

Defining δ as the difference between the value at the current time-step (current iteration) and the next time-step (next iteration) gives

$$\delta P = P_i - P_{i+1} \tag{4.12}$$

$$\delta \dot{m} = \dot{m}_i - \dot{m}_t \tag{4.13}$$

Plugging these into Equation 4.11 and solving for P_{i+1} gives

$$P_{i+1} = P_i + \omega \frac{\dot{m}_i}{\rho_i A^2} \left(\dot{m}_i - \dot{m}_t \right) \tag{4.14}$$

where the values for ρ and $\dot{m}$ in Equation 4.11 have been taken to be those at the current time-step (ρ_i and $\dot{m}_i$, respectively), and a damping parameter ω has been added to artificially reduce the change in pressure between iterations. This can be used to prevent divergence. The values of ρ_i and $\dot{m}_i$ can either be taken from the ghost cells, or the DSMC collision cells. The current implementation takes these values from the ghost cells. This means that pressure will be adjusted until the mass flow rate of the ghost cells matches the specified value.

Equation 4.14 has been used in continuum CFD applications (e.g. STAR-CCM+), but the current work is the first known use of it in a DSMC code. This pressure correction method has been implemented into the implicit boundary condition method in the SPARTA DSMC code and was applied to the same flow field as that used above to evaluate the implicit method. Figures 4.4 and 4.5 show the change in boundary pressure and mass flow rate over time, respectively. It is shown that the iterative method successfully changes pressure to a steady state value which provides the correct mass flow rate, within some amount of statistical scatter, through the ghost cells at the boundary.

For the results shown, the temperature was specified at the outlet, so only velocity was calculated by the implicit boundary condition. When left unspecified, the temperature deviated significantly from expected values. The reason for this behavior is not yet known and will be the subject of future investigation. Additionally, in order to apply the mass flow correction, the top boundary was made a reflective wall. If this were not done, net flow into or out of the domain

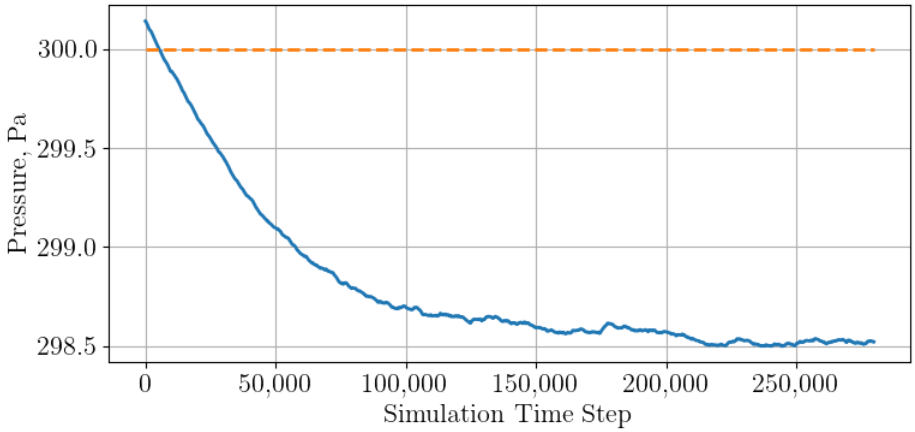

Figure 4.4: Outlet pressure over time for the iterative target mass flow rate boundary condition. The orange line indicates the nominal ambient pressure.

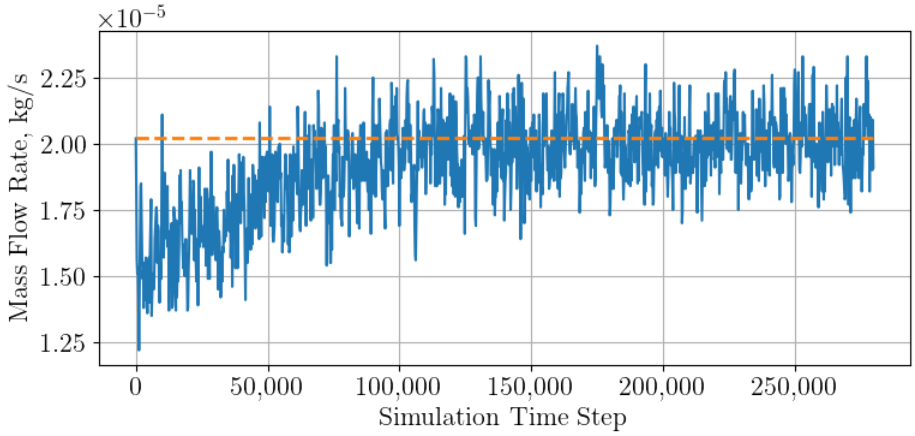

Figure 4.5: Outlet mass flow rate over time for the iterative target mass flow rate boundary condition. The orange line indicates the target mass flow rate which is equal to the mass flow rate into the system.

through the top boundary makes it impossible to specify a priori what the mass flow rate through the outlet should be. Unfortunately, the reflective boundary condition adds an additional source of error in that the simulation is modeling an infinite array of heated wires, rather than a single wire. This leads the temperature of the gas between the wires to be higher than it would if only a single wire were being simulated. This is shown in Figure 4.6 where the temperature contours appear to elongate in the vertical direction. Additionally, Figure 4.7 shows that the constriction of

flow between the wires causes a region of higher velocity at the top of the domain, a feature of the flow field that would not occur if only a single wire were present.

Simulations using the target mass flow outlet, standard implicit outlet, and equilibrium outlet were run to compare the performance of these different boundary conditions. The simulation using equilibrium boundaries used the same condition on all sides of the domain while both the other simulations used a reflective boundary condition on the top side of the domain. Figure 4.8 show

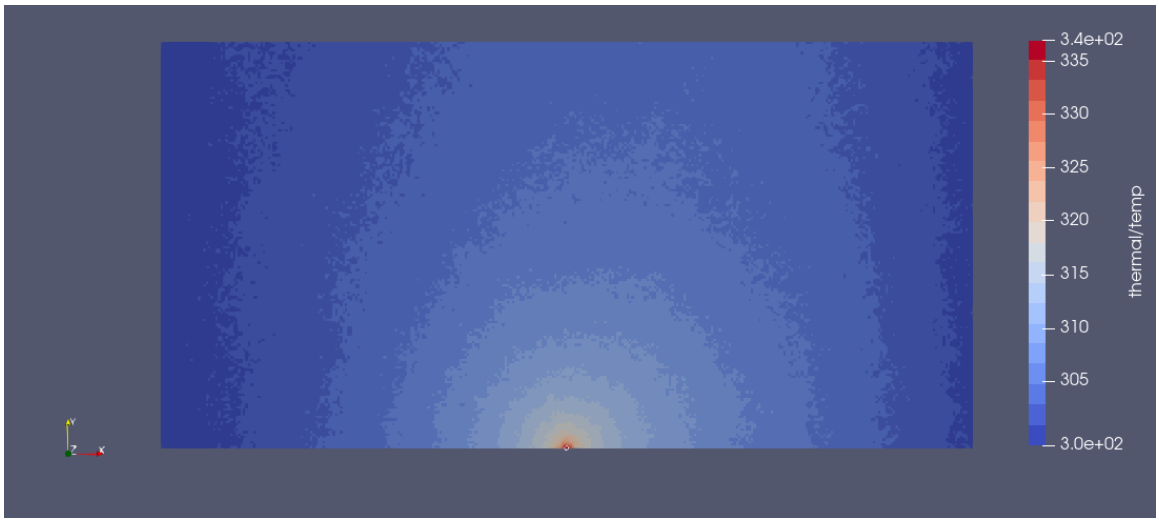

Figure 4.6: Temperature field for implicit boundary condition with time averaging and target mass flow rate. Temperature color scale is in K.

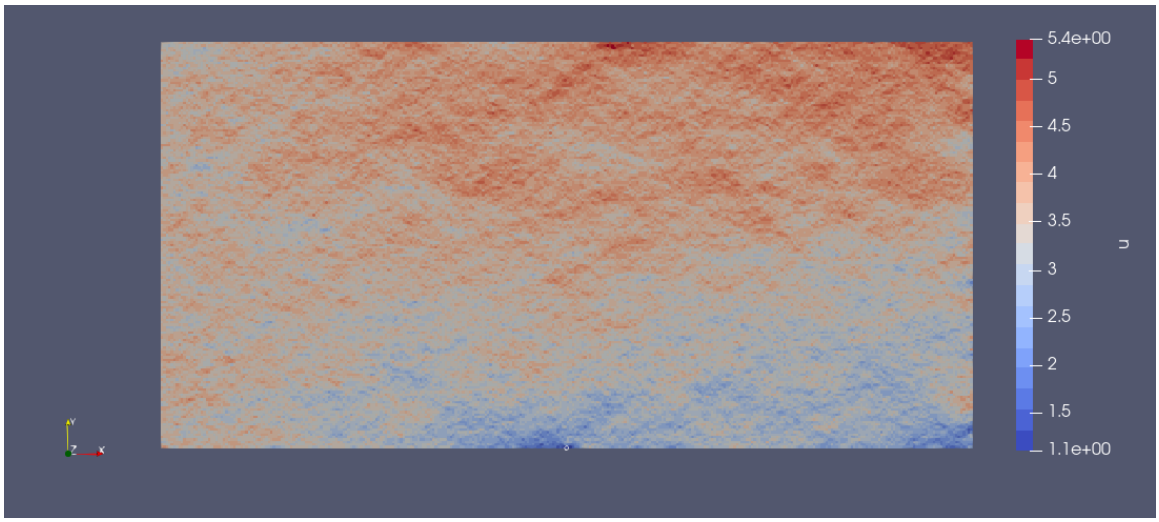

Figure 4.7: Horizontal velocity field for implicit boundary condition with time averaging and target mass flow rate. Velocity color scale is in m/s.

the stagnation line velocity for the three different simulations. Results for both implicit methods show a decrease in velocity between the inlet and the outlet, while the equilibrium boundary condition does not. These data suggest there is some finite amount of drag from the wire that the equilibrium boundary condition might not simulate properly. The standard implicit method with a fixed pressure at the outlet has a lower flow speed throughout the entire domain than the equilibrium boundary condition case. This is consistent with the reasoning above that suggested an incorrect pressure specified at the outlet could create an unrealistic back-pressure.

It was calculated that the mass flow rate through the fixed pressure simulation was lower than the expected value based on the set free stream properties. The target mass flow condition has a generally higher velocity than the equilibrium boundary case and is everywhere higher than the fixed pressure case. Although the data from Figure 4.5 shows that the target mass flow rate boundary condition resulted in the correct mass flow rate through the ghost cells, it was calculated from collision cell data that the mass flow rate through the domain was higher than the desired value. This discrepancy between the ghost cell and adjacent collision cell values is not unreasonable for DSMC simulations because boundary conditions do not force a particular solution as they do in CFD. They only provide a particular flux of particles which then influences the particles inside the domain. It is expected that improved results could be achieved if collision cell data, rather than ghost cell data, were used in Equation 4.14 to adjust the specified pressure at the boundary.

These initial results serve as a proof of concept for the mass flow rate pressure correction boundary condition. Further refinement is needed before it can be more generally applied. For the purposes of the current work, it was concluded that the improvements gained by such a boundary condition would be minimal relative to other uncertainties (e.g. statistical scatter) and biases (e.g. domain size bias, Chapter 5) in the simulations, so further refinement of this boundary condition has not been pursued.

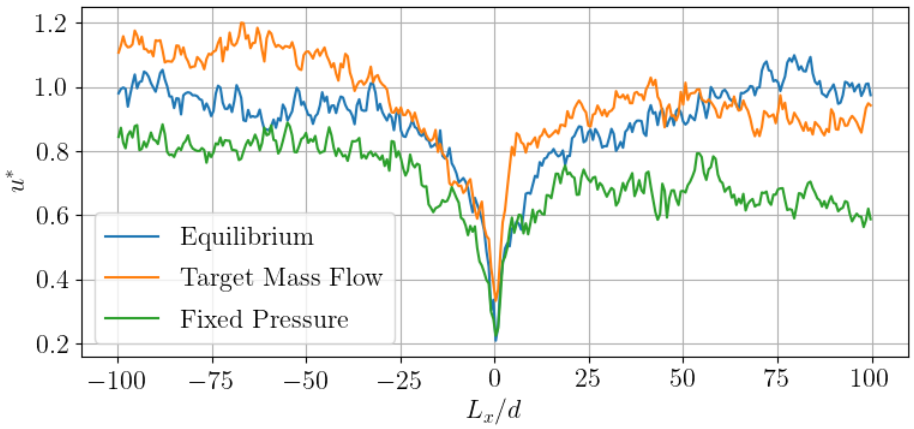

Figure 4.8: Comparison of stagnation line velocity for different outlet boundary conditions.

4.6 Summary and Conclusions

Various boundary conditions for low-speed DSMC simulations were presented and discussed. A target mass flow rate implicit boundary condition is presented and applied to DSMC simulations for the first time. Initial results show that the condition can be effective for limited applications and that further refinement is needed before general use. For the purposes of simulating flow around heated fine-wires, it is concluded that the most appropriate boundary condition for the domain outlet, and all other sides of the domain, is an equilibrium boundary condition. This produces the most realistic flow field around the wire, and most closely reflects the physical situation of the real system. The equilibrium boundary condition implemented in the SPARTA DSMC code is the surface flux method. Results presented in the remainder of this document will use either the piston outlet with an elongated domain ($L_{outlet} = 3L_{inlet}$), or an equilibrium outlet. Minimal differences between these different conditions are observed.

Chapter 5

Influence of Domain Size On Simulated Fine-Wire Heat Transfer

5.1 Overview

In low-speed, nearly incompressible flows, disturbances propagate across very large distances. When simulating a body in an unconfined flow field, this means that domain boundaries must be positioned very far away from the body of interest in order that the solution at the body is no longer a function of their distance away from the body. This domain size issue is less important for internal flows where the boundaries serve as a defining feature of the flow, or for periodic systems where boundary locations are again fixed based on the physical dimensions of the system.

A primary goal of the current study is to investigate the heat transfer from unconfined heated cylinders in low-speed flows. The heat transfer in these low-density and low-speed flows is very small. This makes slight biases introduced by the presence of the domain significant. Figure 5.1 illustrates the challenge at hand. The data shown are for 3 m/s flow of 300 K air (80% N_2, 20% O_2) over a 373.15 K cylinder. These data were produced with a full domain (no symmetry line), elongated downstream section ($L_{outlet} = 3L_{inlet} = 3L$). The outlet used a piston boundary condition. Results are normalized by the simulated Nu_f value when $L/d = 10$. It is observed that a domain large enough to fully converge results has not been achieved for any of the conditions simulated.

The data in Figure 5.1 show that results are a weaker function of domain size for higher values of Kn. This is due to the fact that intermolecular collisions become increasingly less important at larger values of Kn. Fundamentally, small domain sizes introduce error in the present DSMC

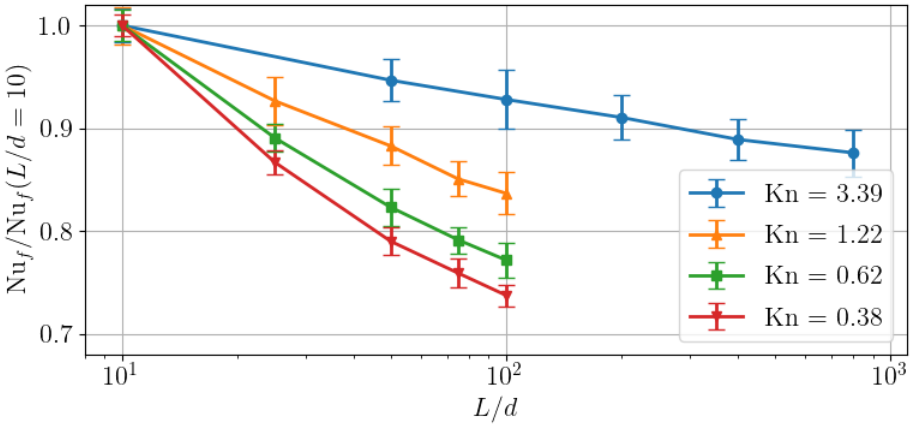

Figure 5.1: Heat transfer as a function of domain size for 3 m/s flow at 4 different Kn values.

simulations because an insufficient number of collisions are simulated between the wire and the free stream. As Kn values increase into the free-molecular regime, intermolecular collisions can be completely ignored and results will become independent of domain size.

A change in domain size influence is also observed for different flow speeds. This is shown in Figure 5.2 where Kn = 0.38. Higher flow speeds converge at smaller domain sizes than lower speeds. Simulated wire heat transfer is a function of the simulated temperature field around the wire. The two primary factors that influence the temperature field are convective forcing from the free stream flow and the location of the domain boundary where temperature is effectively fixed. For large flow speeds, convective forcing is the dominant factor and the location of the boundary has a minimal influence on the temperature field. Conversely, for low flow speeds, convective forcing is weak and the boundary location can be dominant. Unfortunately, the flows of interest to the current study are below about 8 m/s where significant domain size effects are observed.

This domain convergence problem cannot simply be addressed by enlarging the domain because the simulations quickly become impractical or even impossible with current computational resources. Using the computational cost data from Figure 3.5 and the steady state estimation of Equation 3.8, the necessary number of processors to run a simulation to steady state in 12 hours is shown in Figure 5.3 for different values of Kn. These data assume 100 particles per cell. Fewer

processors could be used if less particles were simulated. However, this would introduce statistical scatter which would need to be mitigated by increasing simulation time. Current super computer resources (RMACC Summit) limit simulations to 24 hour run times. It is shown that the estimated number of processors quickly exceeds the capacity of the RMACC Summit super computer, shown in the dashed black line.

It is clear that the domain size influence on results is significant and that available computa-

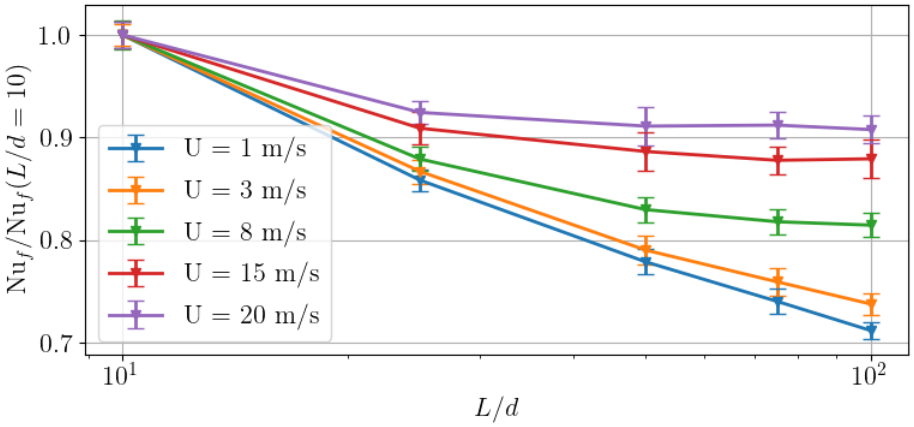

Figure 5.2: Heat transfer as a function of domain size for various flow velocities and Kn = 0.38.

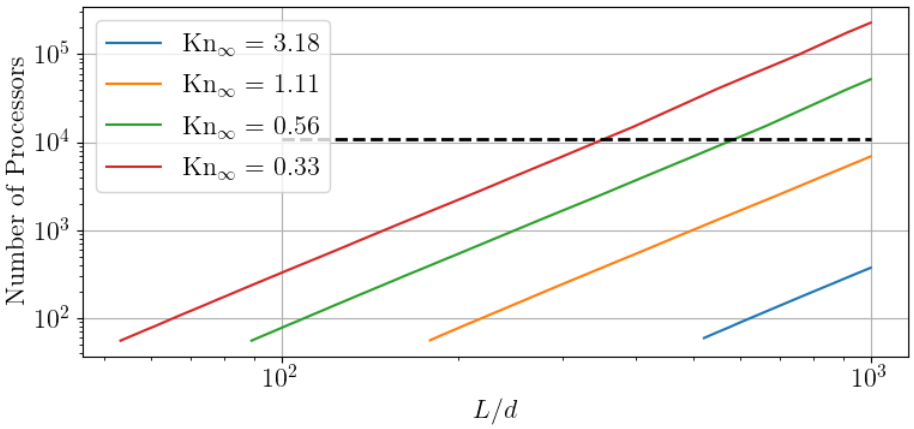

Figure 5.3: Approximate number of processors required for a simulation to reach steady state in 12 hours for various wire Kn values and domain sizes. Flow speed considered is 3 m/s. The black dashed line shows the total number of processors available on the RMACC Summit supercomputer.

tional resources prevent the simulation of the very large domains needed. The remaining sections of this chapter discuss different approaches to address this domain size problem that were considered and attempted.

5.2 Domain Convergence Method

One approach considered for addressing the bias introduced by the domain boundary is to run simulations with various domain sizes and then fit a curve to that data which could be used to predict what the simulated value would be for a sufficiently large domain. Based on the data above, significant extrapolation may be necessary for lower values of Kn. Because of this significant extrapolation, it is desired that the form of the fitting equation be grounded in some physical description of the system, rather than arbitrary curve fits whose limiting behavior may have no physical justification or meaning.

The simulation domain can be approximately modeled by two concentric circular cylinders. The temperature of the inner cylinder is equal to that of the wire, and the temperature of the outer cylinder is equal to that of the free stream. For continuum gas at zero velocity with constant thermal conductivity and a cylinder of unit length, the governing equation for the heat transfer between these two surfaces is given by Fourier's law as

$$\dot{Q} = -kA(r)\frac{dT}{dr} \tag{5.1}$$

where r is the radius from center of the cylinders, $\dot{Q}$ is the rate of heat transfer in W, and $A(r)$ is the heat transfer surface area at radius r. Rearranging and substituting $A(r) = 2\pi r$ gives

$$-dT = \frac{\dot{Q}}{2\pi r k}dr. \tag{5.2}$$

Integrating from the inner to the outer cylinder yields

$$-\int_{T_i}^{T_o} dT = \int_{r_i}^{r_o} \frac{\dot{Q}}{2\pi r k}dr \tag{5.3}$$

$$T_i - T_o = \frac{\dot{Q}}{2\pi k}\left(\ln r_o - \ln r_i\right) \tag{5.4}$$

$$T_i - T_o = \frac{\dot{Q}}{2\pi k}\ln\left(\frac{r_o}{r_i}\right) \tag{5.5}$$

where T_o, T_i and r_o, r_i are the temperature and radius of the outer and inner cylinders, respectively. Solving for $\dot{Q}$ and expressing in terms of simulation domain size $L = r_o$ and wire diameter $d = 2r_i$ gives

$$\dot{Q} = 2\pi k \frac{T_i - T_o}{\ln(r_o/r_i)} = 2\pi k \frac{T_i - T_o}{\ln(2L/d)}. \tag{5.6}$$

Solving in terms of Nu gives

$$\mathrm{Nu} = \frac{\dot{Q}}{\pi k (T_i - T_o)} = \frac{2}{\ln(2L/d)}. \tag{5.7}$$

Interestingly, this theory predicts that Nu$\rightarrow$ 0 as $L/d \rightarrow \infty$. This is in agreement with theory presented in [14] in which a relation for Nu was derived from Oseen's flow theory (Equation 1.8). The reason for this limit in each of these theories is that, according to the continuum model for a fluid at rest, energy transfer only occurs in the presence of a temperature gradient according to Fourier's Law of heat conduction. As the distance between the inner and outer cylinders (or the wire and domain boundary) gets very large, the temperature gradient at the inner cylinder approaches zero. In any case, Equation 5.7 at least provides a functional form for the expected trend between heat transfer and domain size for the current problem in which it is hypothesized that heat transfer to the cylinder is being dominated by conduction between the wire and domain boundary rather than convective forcing. Inspired by this solution, a good candidate for a fitting function is

$$\mathrm{Nu} = A + \frac{B}{\ln(C \cdot L/d)} \tag{5.8}$$

where A, B, and C are fitting parameters calculated using a non-linear least squares algorithm applied to data from simulations with various L/d values. This equation allows a non-zero limit, A, as $L/d \rightarrow \infty$. To illustrate the fitting process, the best-fit lines calculated for the Kn = 0.38 data in Figure 5.2 are shown in Figure 5.4. The form of the model appears to accurately represent the behavior of the data.

The value for the fit parameter A represents the predicted value for Nu at an infinitely large domain. This asymptotic value of Nu is compared with the original DSMC data and experimental data from [63] in Figure 5.5. From this data it appears that the convergence approach worked well

for the values of $\mathrm{Re}_f > 0.075$. However, it appears to dramatically under-predict heat transfer for the lower velocity cases. The reason for this apparent dramatic shift in performance is due to the lower speed simulations being completely dominated by the presence of the boundary. This shows that a particular domain size needs to be reached before any noticeable influence of the free stream velocity is observed. Prior to that domain size, the simulation box behaves very similar to the concentric cylinder model from which the fit was derived, which results in a very low value of A. This is because an infinitely large system in which only conduction is present will have zero heat transfer according to the continuum model [14].

Results of applying the method to a range of conditions is shown in Figure 5.6. All Kn conditions used the same domain sizes to apply the method (L/d = 10, 25, 50, 75, and 100). Again, reasonable corrections to the data are observed for higher Re cases, but at lower velocities, the method appears to dramatically over-correct the data. It is interesting to note that the corrected data for the lower velocity cases actually appears to collapse onto a single curve. This may be evidence of the fact that these simulations are all dominated by the same physical phenomena, that being the domain size since that is constant across all simulations. It should be noted that the parameter A was restricted to only positive values since negative heat transfer for the present conditions is unrealistic. This also prevented divergence of the non-linear solver for some cases.

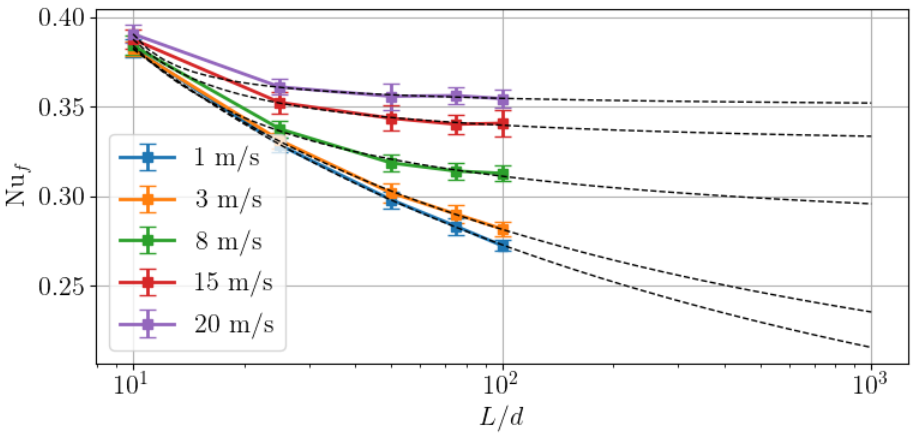

Figure 5.4: Heat transfer data from Figure 5.2 with a non-linear least squares fit of Equation 5.8.

The shortcomings of the method are primarily due to the fact that heat transfer results from simulations with too small of a domain size are entirely dominated by the presence of the domain. The bulk flow has very little influence on the heat transfer. The method only appears to work when simulation domains are large enough to where the convective forcing begins to dominate over the influence of the boundary. This can be seen in Figure 5.7 for data from the $\mathrm{Kn}_f = 0.65$ case. In this view, the dependence of Nu_f on L/d is very linear for the lower velocity cases. Deviations from that trend only occur for the higher velocity cases where convection effects dominate at lower domain sizes. Extrapolating from the data that is almost entirely dominated by conduction between the boundary and the wire results in a large under prediction of heat transfer because conduction will, in fact, become very small for such large domain sizes.

From the above results and discussion for the domain size method, it can be concluded that the approach could work for a limited number of scenarios, but can only be trusted for moderate corrections to simulation results. The method still requires data from simulations with domains that are large enough to where convective forcing begins to dominate over the influence of the boundary. No general methods for predicting how large that is for different conditions is yet established. Given this minimum domain size for the method to work, it is difficult to say how much the approach

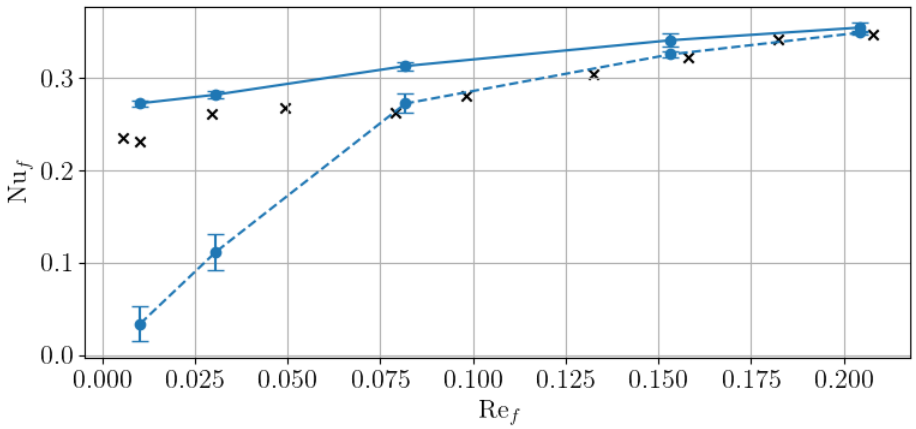

Figure 5.5: Comparison of DSMC results (solid line), domain convergence prediction (dashed line), and experimental data (black x's) for $\mathrm{Kn}_f = 0.38$.

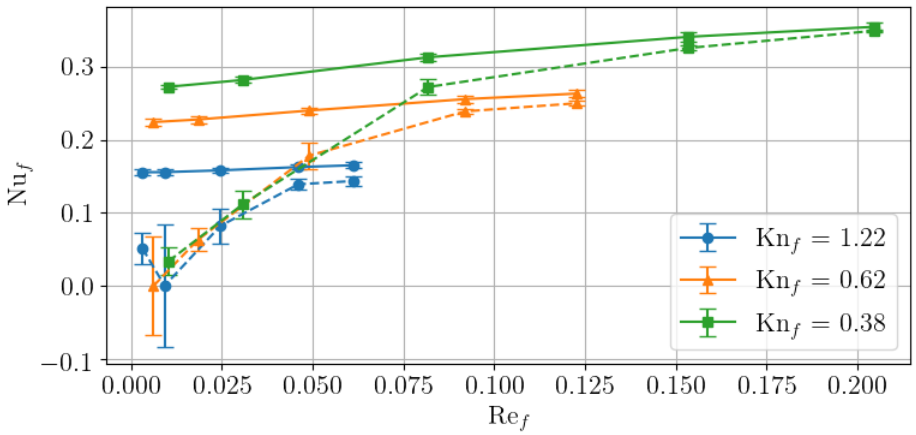

Figure 5.6: Results of applying the domain convergence method to DSMC data collected for various Kn_f values. Dashed lines show the prediction from the domain convergence method with the fit uncertainty.

could reduce the overall computational cost relative to simply running simulations of a sufficient size. Given these shortcomings, no generally applicable domain convergence method has been established. It should be noted that other forms of fitting equations were explored, but the one given in Equation 5.8 has provided the best and most reasonable results to-date. Determining a more appropriate fitting function could be the topic of future study and may help to produce a reliable domain convergence methodology.

5.3 Effect of Domain Length

Given the finite flow speeds, it could be reasoned that better results could be obtained if the downstream boundary is positioned further from the wire than the rest of the boundaries. This was tested for a domain with an equilibrium outlet boundary condition and results are shown in Figure 5.8. For the orange triangle data set, the distance of the outlet from the wire is increased while the inlet and top boundaries remain a fixed distance from the wire ($L_{inlet} = L_{top} = 100 \cdot d$). The blue square data set shows results from a half-square domain where the inlet, top, and outlet are equidistant from the wire ($L_{inlet} = L_{top} = L_{outlet}$). No discernible change in wire heat transfer occurs when only the down stream boundary location is changed, while significant change occurs

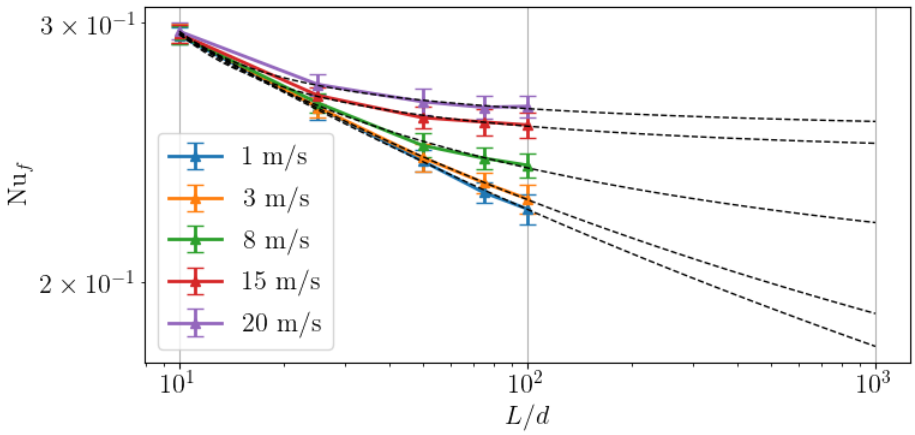

Figure 5.7: Log-log plot of heat transfer as a function of domain size for $\mathrm{Kn}_f = 0.65$.

for the case where all boundaries are moved further from the wire. These data indicate elongated domains do not improve results for the low-speed flows of interest. This also provides evidence that the simulations which used an elongated domain with a piston outlet are likely minimally biased by the slight errors that the piston condition may introduce (§4.3).

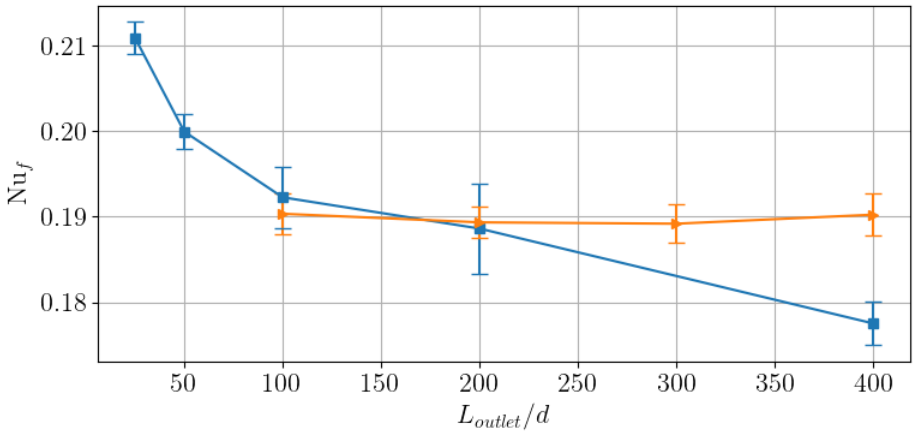

Figure 5.8: Heat transfer data for DSMC simulations with various domain sizes. The blue square data set shows heat transfer results for a half square domain where the inlet top and bottom are equidistant from the wire. The orange triangle data set shows results for a domain where the inlet and top are 100 diameters from the wire center and only the outlet boundary position is changed.

5.4 Improving Computational Efficiency for Large Domains

For continuum CFD simulations, it is common to refine the computational grid where gradients are high or near surfaces. Areas of the flow that have small gradients or are far from surfaces can have larger computational cells. This can greatly improve the efficiency of continuum CFD simulations because the computational cost scales with number of grid elements. The same benefit does not exist for current DSMC methods. Computational cost for a DSMC simulation scales primarily with the number of simulated particles as was shown in Chapter 3. The ratio of real gas molecules to simulated molecules is dictated by the parameter f_{num} which is specified as a single value for each simulation. For the case of a heated wire, density increases to the free stream value as distance from the wire increases. This means that a higher density of simulated particles is required in the far field of the simulation than near the wire even though gradients far from the wire are very small. This is independent of the exact collision cell grid.

DSMC simulations are discretized spatially by collision cells. Collision cells are used to sort particles to be collided with one another. One key physical requirement of DSMC simulations is that the size of collision cells must be less than the mean free path of particles. Mean free path scales inversely with density. Again, considering the flows of interest here, this would result in a finer collision cell grid far from the wire despite the fact that gradients in that region will be small.

In light of the above discussion, refining the collision cell grid for the current simulations would not reduce computational cost as domain size increases. It does, however, highlight a potential area of future development for the DSMC method. A DSMC simulation involves three different discretizations that include the discretization of time with a time-step (Δt), space with collision cells (ΔL_c), and number of particles with f_{num}. Adaptive methods exist for both the time-step and collision cell sizes. These methods have helped to greatly improve the efficiency of many DSMC simulations. However, no method currently exists to dynamically refine f_{num} or to have variable values of f_{num} within a given simulation. The discussion above provides an argument for the development of such a feature. In the far field of the simulation, the density of the gas is high but

the gradients are low. In this region of the flow, it would be reasonable to significantly increase the value of f_{num} (decrease the number of simulated particles). Near the wire, a higher density of simulated particles (lower f_{num}) would be required to accurately capture gradients in the flow and provide a sufficient number of surface collisions for calculating heat transfer. A variable f_{num} scheme for DSMC would be similar to the Discrete Velocity Methods discussed in Chapter 2 where particle mass can change during a collision. As DVM codes increase in availability and maturity, they may prove to be a better simulation method for the current problem than conventional DSMC.

5.5 Summary and Conclusions

Data presented in this chapter show that the influence of domain size on simulated wire heat transfer is significant up to very large domain sizes. Constructing DSMC domains that are large enough to not influence results is computationally impractical or impossible for simulations where the wire Kn value is less than about 3. A domain convergence method was presented as a means to potentially correct results for the bias introduced by the finite domain size. The method appears effective for simulations with larger values of Re when only small corrections to wire heat transfer results are expected. However, it can predict very unreasonable values if insufficient simulation data is provided to the fitting algorithm. Ultimately, the method is not currently robust enough for general implementation. In light of the data presented in this chapter, it is clear that DSMC should not be used to directly generate fine-wire models of Nu as a function of Re for conditions in the middle transition regime because the domain size bias is a strong function of simulated flow speed.

However, DSMC is still useful at examining trends with Kn and can still be used, within a reasonable degree of accuracy, for exploring the parameter space of fine-wires that are difficult to do experimentally. Additionally, experiments of very high Kn flows are difficult because of the decreasing signal to noise ratio. DSMC, however, becomes more feasible with increasing Kn, though the problem of statistical scatter is still present. Given these complementary features of DSMC and experimental data, the two means of collecting data should be used together to paint a picture

of heat transfer through the entire transition regime. Despite the known bias introduced by finite domain sizes, the remainder of this report presents simulation results exploring various aspects of the fine-wire parameter space. The effect of domain size bias on those results is discussed in light of the data presented in this chapter.

Chapter 6

Fine-Wire Heat Transfer in Rarefied Flows

6.1 Overview

This chapter presents results from DSMC simulations of heated fine-wires in rarefied flows. Given the shortcomings of the current simulation methodology, as discussed in Chapter 5, the goal of the simulations herein is not to develop heat transfer models directly. Simulations are instead used to explore the parameter space of these fine-wires and to develop some physical insight into their behavior in the transition regime.

The work of Xie et al. 2017 is cited frequently throughout this chapter [63]. The data and empirical models presented in that work represent the most recent and thorough treatment of fine-wire heat transfer in the transition regime. They present empirical models derived from their data which are currently being used for processing turbulence measurements for the HYFLITS campaign. Verifying those models and understanding their limitations is of immediate engineering and scientific interest.

6.1.1 Initial Verification of Simulation Results

Figure 6.1 shows simulation results for heat transfer across a wide range of Kn_f values along with experimental data and free-molecular theory [63]. These data are for a flow speed of about 5 m/s. At low Kn_f values, good agreement with experiment is observed. As Kn_f increases, DSMC data begins to agree very well with free-molecular theory. These data show that, despite the biases caused by the finite domain size, the present simulations can still provide realistic results

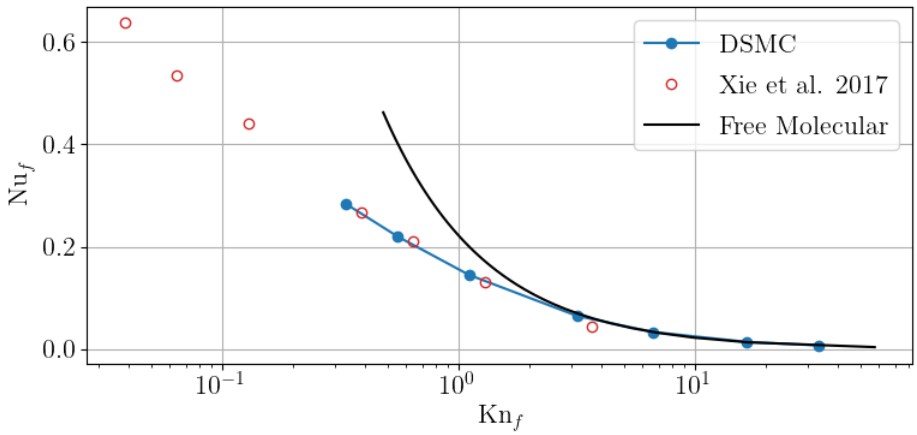

Figure 6.1: DSMC Simulation results compared with experimental data from [63] and free-molecular theory through the transition regime.

and trends through the transition regime. This data also supports the claim made in the previous chapter that DSMC will become increasingly accurate at higher Kn values and can therefore be trusted to accurately predict when free-molecular theory becomes sufficiently accurate.

6.2 Sensitivity to Reynolds Number

Figure 6.2 shows a comparison of DSMC simulation results to the empirical model for Nu_f presented in [63]. Generally good agreement is observed. Simulated heat transfer shows a lower sensitivity to velocity than the empirical model. This can be attributed to the bias due to finite domain size which increases with decreasing Re_f as was discussed in Chapter 5. Difference between simulation data and the empirical model is shown in Figure 6.3. Decreasing simulation bias with increasing Re_f is clearly observed. Despite that known bias, however, simulations predict a lower Nu_f value at high Re_f for the $\mathrm{Kn}_f = 1.12$ case. This discrepancy is relatively small and could be due to any number of minor differences between the simulation and experiment including the surface accommodation coefficient α or the wire temperature. Another possible cause is the piston outlet condition used for the simulation data shown. As was discussed in Chapter 4, this condition is expected to result in an unrealistic temperature field around the wire. That bias will tend to

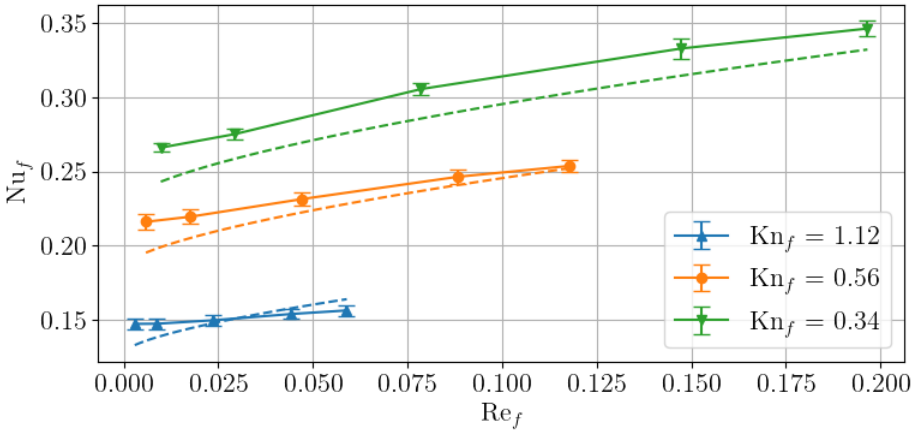

Figure 6.2: Comparison of DSMC heat transfer data (markers and solid lines) with the empirical model presented in [63] (dashed lines) for various Kn_f values. Uncertainty bars indicate $\pm 1\sigma$ of the steady state DSMC data.

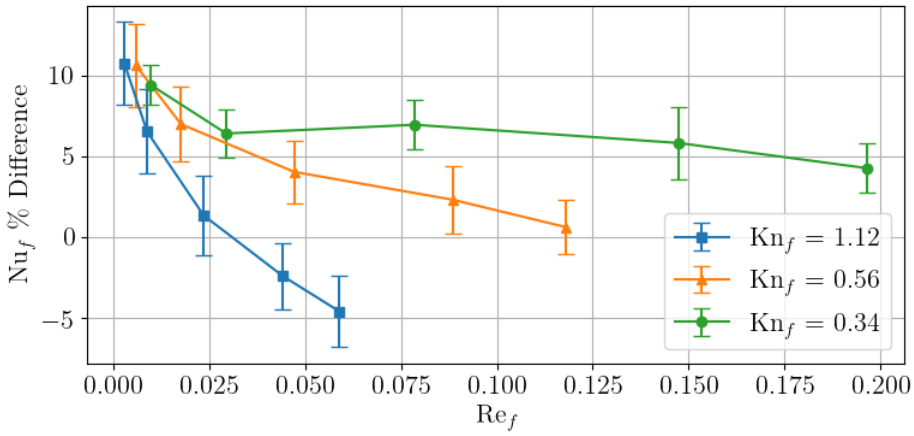

Figure 6.3: Difference between DSMC heat transfer data and the empirical model presented in [63] for various Kn_f values. Uncertainty bars indicate $\pm 1\sigma$ of the steady state DSMC data.

increase the temperature on the downstream side of the wire which would subsequently decrease the power loss from the wire to the fluid. Given the model and simulation uncertainties, it is difficult to draw any decisive conclusions about this difference between the simulations and empirical model.

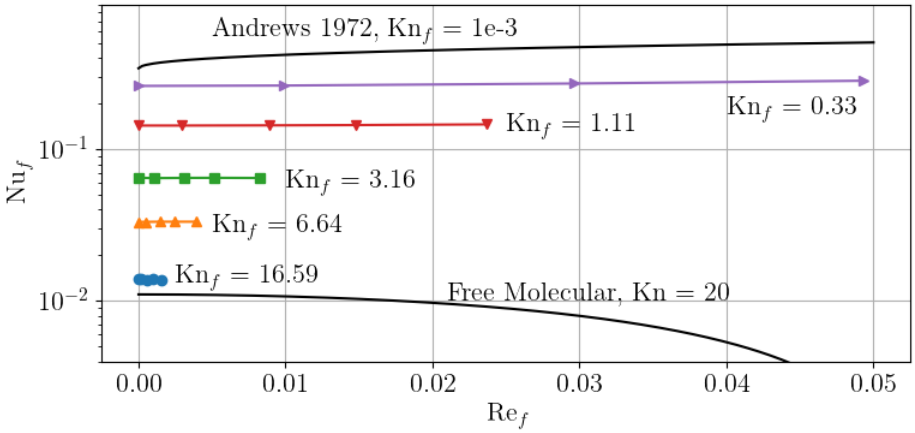

Figure 6.4: Simulation data for Nu_f as a function of Re_f for various Kn values. Empirical model from [5] and free-molecular theory are shown.

6.2.1 Velocity Dependence from Continuum to Free-Molecular

Figure 6.4 shows DSMC results for Nu_f as a function of Re_f for various Kn_f values. Included in the plot is the empirical model for slip-flow from [5] and free-molecular theory. It is seen that these two cases have entirely different behaviors. The model from [5] shows Nu_f as an increasing function of Re_f. This is also true for the models presented in [63] and all known models in continuum and slip-flows. The free-molecular solution, however, is a decreasing function of Re and the maximum value of Nu occurs at $\mathrm{Re} = 0$.

The free-molecular result can be reasoned by considering the molecular model of fluids. Gas particles impact a surface and then are emitted from that surface. A particle's state before and after that interaction may or may not be correlated depending on the type of collision that occurs. Energy transfer with the surface occurs when a particle has a different energy before and after it collides with the surface. In a free-molecular flow, intermolecular collisions do not occur. This means that every particle hitting the wire is from the free stream and will, statistically speaking, share the same thermal properties of the free stream. For a wire with an elevated temperature relative to the free stream, this means that the maximum positive energy difference between the state of particles being emitted from the wire and the state of particles impacting the wire occurs

when the velocity is zero. As flow speed increases, the kinetic energy of particles hitting the surface increases, decreasing the energy difference between emitted particles and impacting particles. This results in Nu decreasing with increasing Re. At a certain flow speed, or Re value, free stream particles will have a greater energy than particles emitted from the surface causing the flow of energy to reverse and instead go from the fluid to the surface. For the case shown in Figure 6.4, this occurs at a Re_f value of about 0.44 for free-molecular flow (although it cannot be seen because the y axis is log scale).

The same phenomena also occurs in the continuum. At sufficiently high flow speeds the net energy transfer will be from the fluid to the wire, rather than the reverse. The point at which this occurs is a function of the temperature difference for both free-molecular and continuum flows. This means that a maximum Nu_f occurs at some finite value of Re_f in a continuum flow. The data here shows that the value for Re_f at which a maximum heat transfer occurs must drop from some finite value to zero as Kn increases through the transition regime.

A key practical implication from the results of Figure 6.4 is that the value of $\partial \mathrm{Nu}_f / \partial \mathrm{Re}_f$ at low values of Re_f moves from a positive value in the continuum and slip-flow regimes to a negative value in the free-molecular regime. This means the sensitivity of wire heat transfer to flow speed is very small for low-Re_f values through the transition regime. This can make hotwire flow speed or turbulence measurements very difficult and impossible at the point where $\partial \mathrm{Nu}_f / \partial \mathrm{Re}_f = 0$. This comparison with free-molecular theory also explains why simulated heat transfer shows no discernible sensitivity to flow velocity for higher Kn values. It was first reasoned that this was due to the domain size bias, and that still may be true to a certain extent. However, according to the above discussion, there is a physical justification for an insensitivity of heat transfer with velocity for high Kn flows.

6.3 Sensitivity to Gas Composition

The experiments of [63] were performed using diatomic nitrogen, N_2. Previous authors have shown that fine-wire heat transfer models can be applied to various gases with little error [5].

Simulations were run to explore the dependence of heat transfer on gas composition for the current conditions. Three different gases were simulated including 100% N_2, 100% Ar, and a mixture of 80% N_2 and 20% O_2 to simulate atmospheric air. Results are compared with empirical models from [63] in Figure 6.5. The difference between empirical models and simulation data is shown in Figure 6.6. Minimal difference between simulations of N_2 and air are observed, while a significant difference is observed for the simulations of Ar. The former point is important because it helps to validate the use of the model from [63] for analyzing atmospheric turbulence measurements currently being made. The results shown also reveal that the empirical models should not be extrapolated above the specified range for Kn_f ($\mathrm{Kn}_f < 3$). Even being slightly outside of this range results in very large discrepancies as is shown by the $\mathrm{Kn}_f = 3.15$ data for N_2 and air.

The significant shift observed for the simulations of Ar shows that some dimension of the parameter space has not been sufficiently taken into account in the empirical model. To further validate the Ar results, Figure 6.7 shows simulation data for both Ar and N_2 as Kn_f values are increased into the free-molecular regime. Each data set shows a smooth transition to the free-molecular solution, which is notably different for the two mixtures. This highlights that analysis of free-molecular theory is useful for understanding the important dimensions of the fine-wire parameter space in the transition regime. It is reasonable to conclude from the data shown that the models from [63] should not be applied to gas mixtures that are significantly different than pure N_2.

6.4 Sensitivity to Accommodation Coefficient

Thermal accommodation coefficient, α_{th}, quantifies the efficiency of energy transfer between a gas and a surface. A typical definition for α_{th} is

$$\alpha_{th} = \frac{q_i - q_r}{q_i - q_w} \tag{6.1}$$

where q_i is the incident energy flux, q_r is the energy flux of particles reflected off the surface, and q_w is the energy flux away from the surface if all reflected particles are emitted from the surface according to the Maxwellian equilibrium distribution at the wall temperature ($0 \leq \alpha_{th} \leq 1$). Experimental

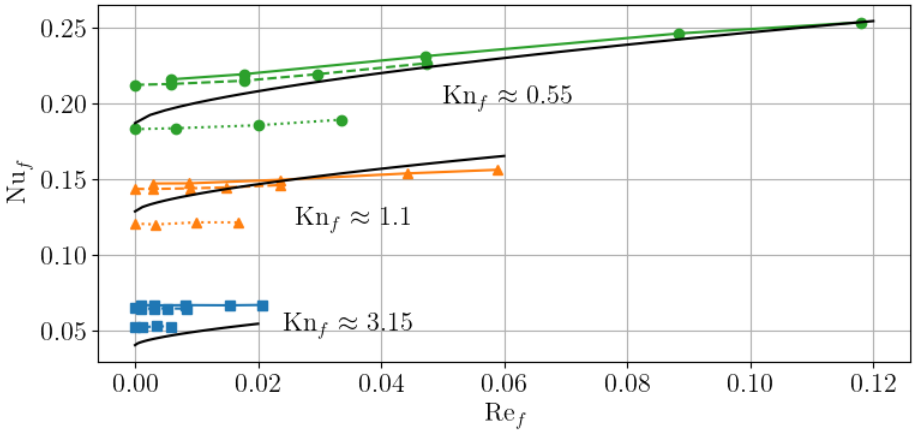

Figure 6.5: Simulated values of Nu_f as a function of Re_f for simulations of N_2 (dashed lines), Ar (dotted lines), and a mixture of 80% N_2 and 20% O_2 (solid lines). Empirical models from [63] are also shown for reference.

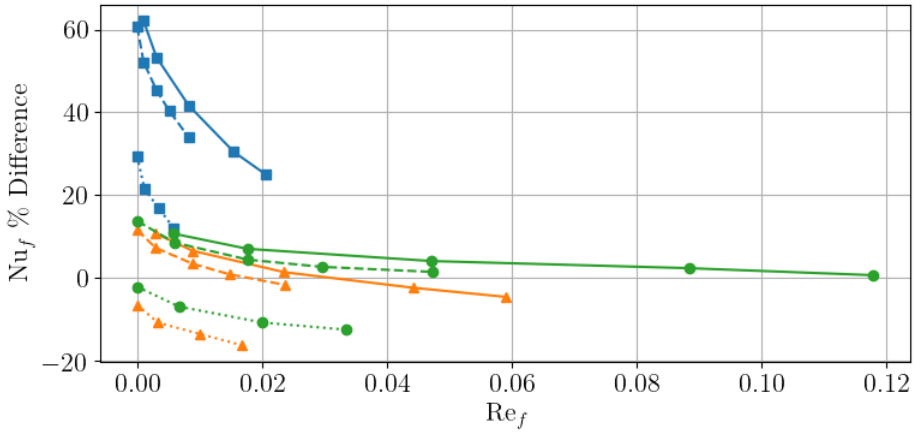

Figure 6.6: Difference between simulated values of Nu_f and the empirical model from [63]. Data is from simulations of N_2 (dashed lines), Ar (dotted lines), and a mixture of 80% N_2 and 20% O_2 (solid lines). Data for Kn_f values of 0.55 (green circles), 1.1 (orange triangles), and 3.15 (blue squares) are also shown.

determination of α_{th} can be quite difficult because it depends on many factors including the gas mixture, surface material, surface temperature, pressure, and surface manufacturing details [3, 5, 12, 23]. Manufacturing inconsistencies and surface impurities can significantly change α_{th}, especially for micro-surfaces whose surface flaws have a length scale similar in magnitude to the surface itself. Many authors have noted that α_{th} becomes an increasingly important parameter for fine-wires as

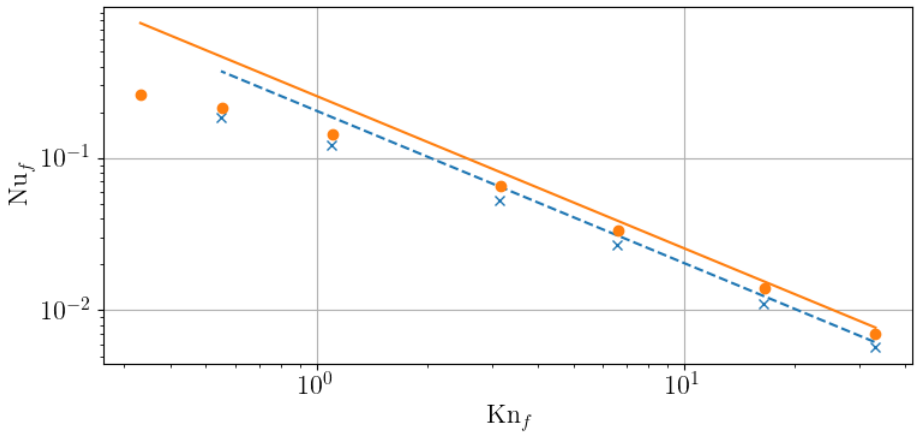

Figure 6.7: DSMC data for Nu_f as a function of Kn_f for zero velocity Ar (blue x's) and N_2 (orange circles). Free-molecular solutions for each mixture are also shown with the dashed blue line and the solid orange line showing the solutions for Ar and N_2, respectively.

Kn values increase [5, 6].

While it is very difficult to experimentally measure and control the accommodation coefficient of fine-wires, a specific value for α_{th} can be modeled simply in the DSMC method by considering a mix of specular and diffuse reflections at the wire surface. During a specular reflection, the normal velocity of an impacting particle is reversed and internal energy modes remain unchanged. Particle energy before and after the surface reflection is equal, so no energy transfer occurs. During a diffuse reflection, a particle that impacts a surface is assumed to be absorbed, then re-emitted from the surface in a random direction with a speed and internal energy according to the Maxwellian equilibrium distribution at the surface temperature. The fraction of diffusely reflected particles is specified for a simulation by the parameter α. A specific value for α_{th} is modeled by setting $\alpha = \alpha_{th}$. If $\alpha = 1$, all particles are diffusely reflected and $q_r = q_w$. If $\alpha = 0$, all particles are specularly reflected and $q_r = q_i$. The net energy exchange between the surface and the gas is zero for a fully specular surface.

Because of the uncertainty in experimentally measured values for α_{th}, DSMC simulations were used to investigate the sensitivity of wire heat transfer to variations in α. Simulations were performed with different values of α. Figure 6.8 shows the dependence of Nu_f on α for four different

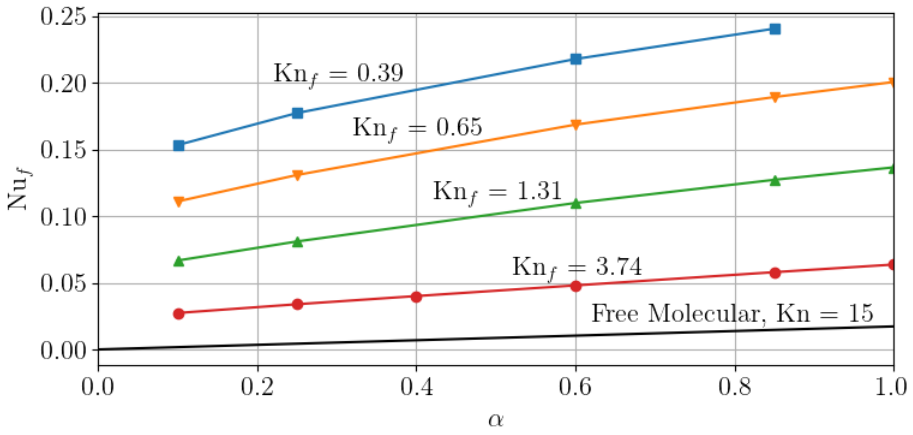

Figure 6.8: Dependence of wire power loss on surface accommodation coefficient at different values of wire Knudsen number. Data shown correspond to $U_\infty = 3$ m/s. The free-molecular solution for Kn = 15 is also shown.

Kn$_f$ cases. Results shown correspond to $U_\infty = 3$ m/s, though this same data was also produced for $U_\infty = 1$, 8, 15, and 20 m/s. Similar trends are observed at other velocities. Only one case is presented for brevity. The simulated mixture is air (80% N_2 and 20% O_2) at various pressures ($P = 105$, 300, 600, and 1000 Pa). Free stream and wire temperatures are $T_\infty = 300$ K and $T_w = 373$ K. Wire diameter is $d = 20$ μm. An elongated domain was used where $(L_{inlet}, L_{top}, L_{oulet})/d = (100, 100, 300)$. A piston condition was assigned at the outlet.

The data shown for each value of Kn$_f$ are quite linear for $\alpha > 0.25$. It is known that all of these curves, however, must pass through the origin where all reflections are specular (Nu$_f$ = 0 when $\alpha = 0$). This means that the gradient (∂Nu$_f/\partial\alpha$) must be very high and non-linear as α approaches zero. Details of the behavior near $\alpha = 0$ are not of particular interest to the current study because realistic values of α_{th} for hotwires in air are greater than 0.5, where the data appears linear. The model for free-molecular flow is also shown. As can be seen in Equation 3.9, the rate of heat transfer is directly proportional to α in free-molecular flow.

DSMC data presented in most of this work uses $\alpha = 0.85$, an estimate for both tungsten and platinum wires in N_2 or O_2 [3]. Using the data shown in Figure 6.8 (and that same data for other velocity cases), the derivative of Nu$_f$ with respect to α at $\alpha = 0.85$ can be estimated using a simple

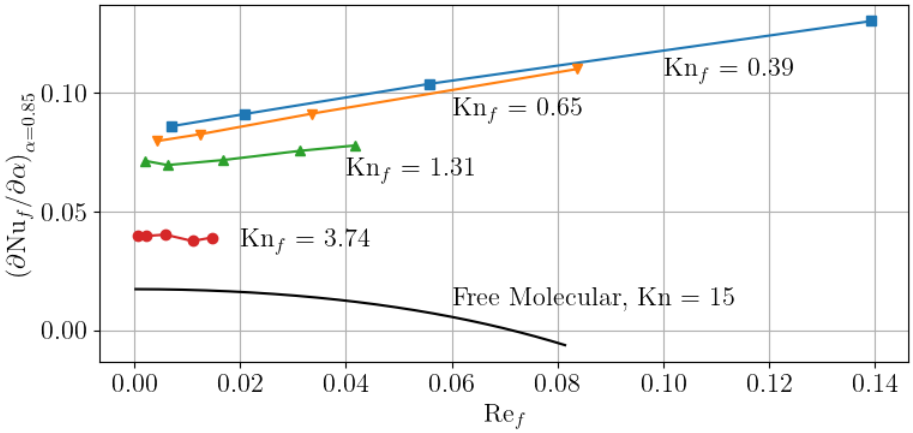

Figure 6.9: Derivative of Nu_f with respect to α evaluated from DSMC data at $\alpha = 0.85$. Black line is calculated from free-molecular theory for Kn = 15.

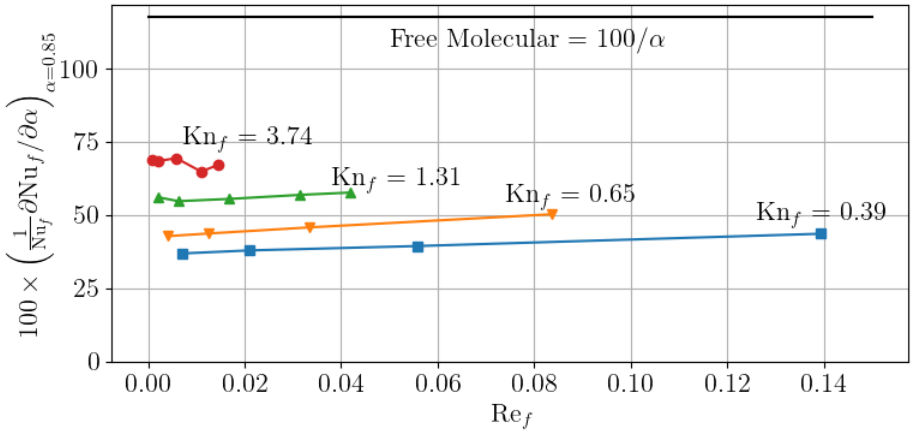

Figure 6.10: Derivative of Nu_f with respect to α evaluated from DSMC data at $\alpha = 0.85$ normalized by the respective value of Nu_f. The result from free-molecular theory is given by the solid black line.

finite difference. The calculated value for $\partial \mathrm{Nu}_f/\partial\alpha$ is shown as a function of Re_f for different Kn_f values in Figure 6.9. The same data are shown in Figure 6.10 normalized by the respective value of Nu_f. These data represent the percent uncertainty in Nu_f caused by some uncertainty in α.

A shift in the dependence of $\partial \mathrm{Nu}_f/\partial\alpha$ on Re_f occurs as Kn values increase through the transition regime and into the free-molecular regime. Simulation results show that increased sensitivity to α is observed with increasing Re_f and Kn_f. The opposite trend with Re_f is observed in the

free-molecular case. Free-molecular theory predicts that sensitivity to α decreases with increasing Re_f and actually reverses sign at sufficiently high Re_f. The point at which $\partial \mathrm{Nu}_f/\partial\alpha = 0$ identically aligns with where the rate of heat transfer is zero. At higher values of Re, the direction of heat transfer reverses so that energy is instead transferred from the fluid to the wire. The negative sign for $\partial \mathrm{Nu}_f/\partial\alpha$ after this point means that smaller values of α lead to less negative values of Nu_f.

The normalized data in Figure 6.10 reveals that although the absolute sensitivity decreases with higher Kn values, the relative sensitivity increases. This is consistent with the reasoning and data of previous researchers who have noted that the importance of knowing α_{th} increases in the rarefied flow regimes [5, 6]. The free-molecular solution is also shown in Figure 6.10. This solution is readily derived by considering that the free-molecular solution for Nu is directly proportional to α,

$$\mathrm{Nu} = \alpha f(\mathrm{Pr}, \mathrm{Re}, T^*, \gamma). \tag{6.2}$$

The derivative of Equation 6.2 is then

$$\frac{\partial \mathrm{Nu}}{\partial \alpha} = f(\mathrm{Re}, \mathrm{Pr}, T^*, \gamma). \tag{6.3}$$

Normalizing by the respective value of Nu then gives

$$\frac{1}{\mathrm{Nu}}\frac{\partial \mathrm{Nu}}{\partial \alpha} = \frac{1}{\alpha}. \tag{6.4}$$

This value is constant with respect to Re, which justifies the results for the $\mathrm{Kn}_f = 3.74$ case where the data also appears constant with respect to Re_f. The dependency on Re_f observed in the lower Kn_f cases could be due to the domain size bias. It is known from the results presented in Chapter 5 that current DSMC simulations over-predict Nu_f at lower values of Re_f. If, however, simulations predict $\partial \mathrm{Nu}_f/\partial\alpha$ more accurately than $\partial \mathrm{Nu}_f/\partial \mathrm{Re}_f$, then normalizing by the biased data would explain the positive slope seen for high Kn cases in Figure 6.10.

The data above provide approximate values that can be used for subsequent sensitivity analyses of fine-wires operating in the transition regime. For example, if a finewire has a surface accommodation coefficient of $\alpha = 0.85 \pm 0.1$, this data shows that the subsequent uncertainty in

Nu_f ranges from about 3.6% to 7.5% for Kn values from 0.39 to 3.74. The free-molecular limit provides a maximum estimate for the sensitivity of Nu with α. This maximum limit, for a given value of α is $100 \times \delta\alpha/\alpha$. For the example just mentioned, this value is $\approx 12\%$.

6.5 Sensitivity to Temperature

The free stream and wire temperatures for the experiments of [63] were 300 K and 373.15 K, respectively. At altitudes of interest for the HYFLITS research campaign, the ambient temperatures range from about 216 K to 232 K according to the standard atmosphere model [1]. Wire temperatures are controlled to be about 30-40 K above the ambient. This large difference in temperatures warrants a particular investigation. DSMC simulations at various pressures were run with a free stream temperature of 225 K and wire temperature of 260 K. These data are compared with other simulation data where $T_w = 373.15$ K and $T_\infty = 300$ K and the empirical models from [63] in Figures 6.11 and 6.12. The latter figure shows the difference between simulation results and the empirical model.

For all data that lies within the stated model bounds ($\mathrm{Kn}_f < 3$), the difference is less than 20%. It does, however, appear that the lower temperature cases generally have a higher difference for a given value of Re_f. This difference is still within the expected simulation biases, though, so definitive conclusions cannot be drawn. Considering the limit of free-molecular flow, the Nusselt number becomes a function of temperature through the term $T^* = T_w/T_\infty$. The value of T^* for the experiments of [63] is 1.24 and for the HYFLITS measurements is about 1.16. Figure 6.13 compares the two different temperature cases across a wide range of Kn_f values for a flow velocity of 3 m/s. Also shown is the empirical model from [63] and free-molecular theory. Only one line is drawn for each model because the difference between model predictions for the two different temperature cases is less than the line width. The small difference in the value of T^* for the two cases results in a small difference in the solution at the free-molecular limit. This provides further evidence that the models from [63] can be used to analyze turbulence measurements despite the different temperature situation in the HYFLITS fine-wire measurement system.

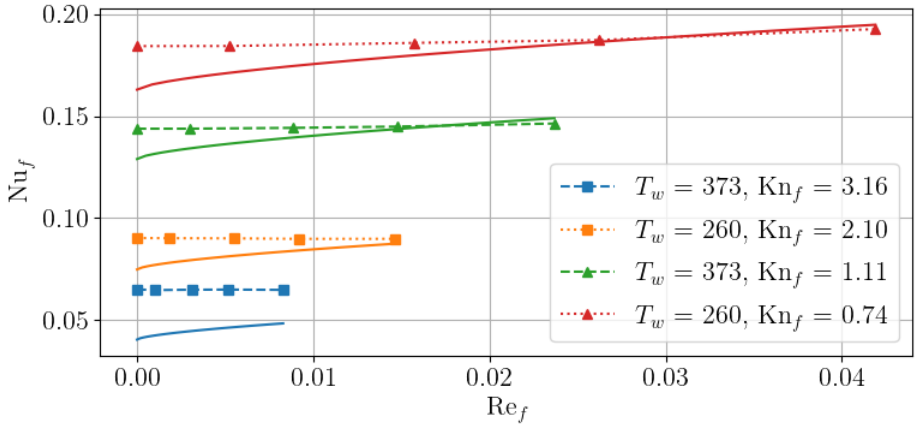

Figure 6.11: Simulated Nu_f as a function of Re_f for wires at various temperatures and Kn_f values. Solid lines show the respective empirical models from [63].

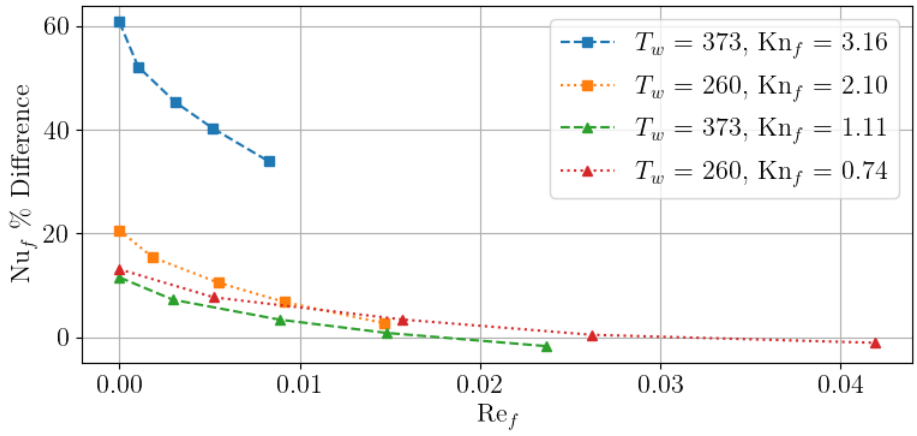

Figure 6.12: Difference between simulated heat transfer rate and empirical models from [63] for simulations of various wire temperatures.

6.6 Heat Transfer From Transition to Free-Molecular Regimes

Simulation results in Figure 6.13 show a smooth transition from the empirical model of [63] for $\mathrm{Kn} < 2$ to free-molecular theory for $\mathrm{Kn} > 5$. Percent difference between simulation results and each of these models is given in Figure 6.14. This view further illustrates the range of applicability for each model. A difference of less than 10% between simulation results and the empirical model is observed for $\mathrm{Kn}_f < 2$. Much of this is attributable to the finite domain size error in the

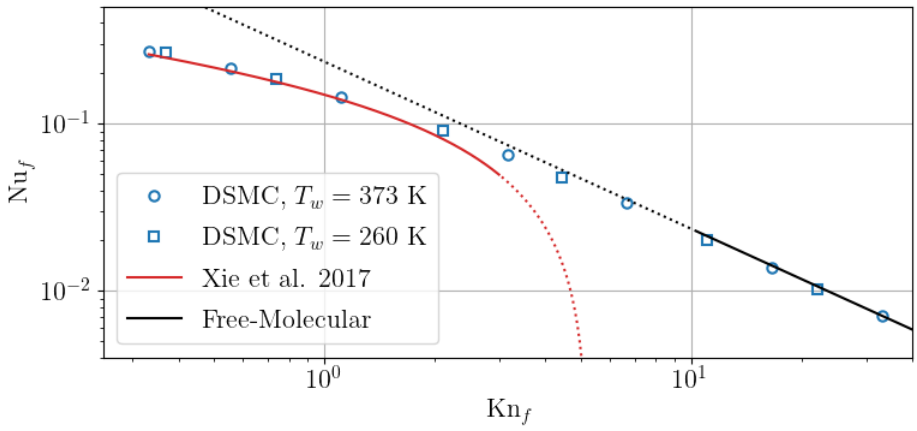

Figure 6.13: Comparison between simulation results, the empirical model from [63], and free-molecular theory. Dotted lines indicate an extrapolation of the respective model.

simulations. However, the model and simulation results significantly diverge for Kn values above 2 with differences greater than 40% by a Kn value of 3. Large differences at Kn values above 3 were observed in results above. It was originally stated in [63] that the empirical model could be applied to Kn values up to 3. However, the present results suggest that the applicable range may only extend up to a Kn value of about 2. Simulation results show increasingly better agreement with free-molecular theory as Kn increases. For $\mathrm{Kn} \geq 3$, the difference between simulation results and free-molecular theory is less than the difference with the empirical model from [63].

These results have direct implications for fine-wire measurements of turbulence in the stratosphere. Shown in Figure 6.14 are dashed vertical lines that indicate the respective altitude for the given value of Kn for a 5 μm wire with $T_w - T_\infty = 35$ K according to the 1976 U.S. Standard Atmosphere Model [1]. This approximately models the conditions of balloon-borne fine-wires of the HYFLITS campaign. This shows that the empirical models from [63] are appropriate for data collected below about 35 km. Above that altitude, significant errors may be introduced by using the model from [63]. In the processing of data, the value of Kn_f based on measured temperature and pressure should be checked. To ensure that empirical models introduce an error that is less than about 20% (Appendix A), data collected where $\mathrm{Kn}_f > 2.5$ should be discarded until a more

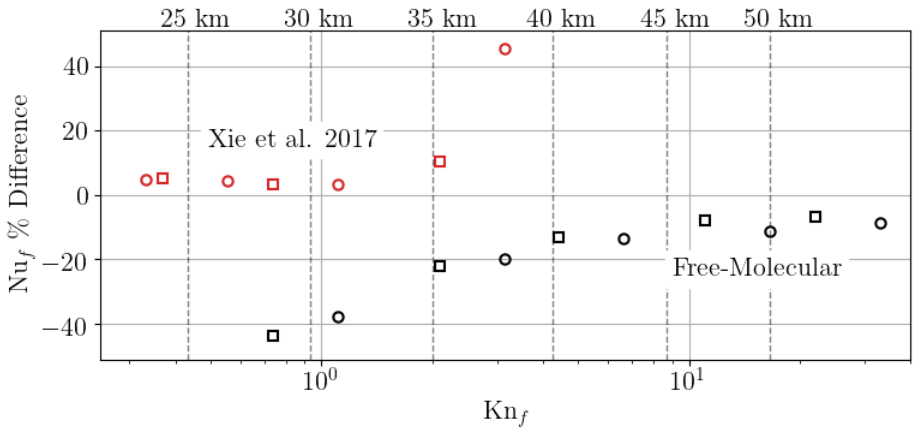

Figure 6.14: Difference between simulated Nu and the empirical model from [63] (red) and free-molecular theory (black). Square markers show results where $T_w = 260$ K and $T_\infty = 225$ K. Circle markers show results where $T_w = 373$ K and $T_\infty = 300$ K. Dashed vertical lines and labels indicate the respective altitude for a 5 μm wire with $T_w - T_\infty = 35$ K [1].

appropriate empirical model is developed for these values of Kn_f.

As discussed in §6.2.1, the shift to free-molecular conditions results in a sign change of $\partial \mathrm{Nu}_f / \partial \mathrm{Re}_f$. Present results suggest that this sign change could occur at an altitude between 40 and 50 km for the HYFLITS system based on the fact that simulations begin to agree very well with free-molecular theory in this region. Further simulations and analyses are necessary to more accurately identify where $\partial \mathrm{Nu}_f / \partial \mathrm{Re}_f = 0$.

6.7 Conclusions

Extensive simulation data exploring the parameter space of fine-wires in the transition regime was presented in this chapter. Initial verification of simulation results is given in Section 6.1.1. Several important conclusions can be drawn from the data presented.

Given the known simulation error discussed in Chapter 5, results shown in Section 6.2 for the velocity dependence of power loss verifies empirical models from [63] for the values of Kn_f and Re_f explored.

An investigation of the velocity dependence of heat transfer rate from continuum to free-

molecular conditions was conducted in Section 6.2.1. It is observed that $\partial \mathrm{Nu}_f / \partial \mathrm{Re}_f$ changes from a positive value in the continuum regime to a negative value in the free-molecular regime for low-Re conditions. This means that $\partial \mathrm{Nu}_f / \partial \mathrm{Re}_f = 0$ at low-Re values somewhere in the transition regime. Fine-wires cannot be used to measure changes in flow speed at the point where $\partial \mathrm{Nu}_f / \partial \mathrm{Re}_f = 0$. Based on subsequent results presented in Section 6.6, it is predicted that $\partial \mathrm{Nu}_f / \partial \mathrm{Re}_f = 0$ at an altitude between 40 and 50 km for the HYFLITS measurement system. Further investigation is necessary to more precisely identify where $\partial \mathrm{Nu}_f / \partial \mathrm{Re}_f = 0$ for the conditions of interest.

Simulations of various gas compositions reveal that differences in heat transfer rate for fine-wires in N_2 and air (80% N_2, 20% O_2) are negligible over the Re_f and Kn_f ranges of interest to the HYFLITS campaign. This verifies the use of empirical models, which are derived from experimental data for N_2, for measurements made in atmospheric air. However, significant differences are observed between results for N_2 and Ar. The observed differences are supported by the fact that free-molecular solutions for these two gases are similarly different.

An investigation of power loss dependence on the surface accommodation coefficient α is presented in Section 6.4. Results show that the relative sensitivity of heat transfer rate to α increases with Kn_f and reaches a maximum at the free-molecular limit. Free-molecular theory shows that for the particular case of $\alpha = 0.85 \pm 0.1$ (which is representative of real fine-wires), the maximum uncertainty in Nu is about 12%.

Simulations with wire and free stream temperatures matching both experiments from [63] and the HYFLITS measurement system were performed. No significant differences in wire power loss between these two different temperature situations are observed. This result is supported by that fact that the two temperature situations have similar solutions at the free-molecular limit. This further verifies the use of empirical models from [63] for the HYFLITS system.

Finally, differences between simulation results and the empirical model from [63] and free-molecular theory are explored over a wide range of Kn_f in Section 6.6. The empirical model diverges from simulation results significantly for Kn_f values above 2 which corresponds to altitudes above about 35 km for the HYFLITS measurement system. The difference between simulation data and

free-molecular theory is less than 20% for Kn_f values above 4 or altitudes above about 40 km. New power loss models are needed for measurements collected where Kn_f is greater than about 2.5 and until free-molecular theory is deemed sufficiently accurate.

Chapter 7

Fine-Wire Temperature Jump in Rarefied Flows

7.1 Overview

The phenomena of temperature jump in rarefied flows is well known. Temperature jump refers to the difference in temperature between a surface and the gas immediately adjacent to that surface. Wall boundary conditions for continuum CFD generally assume this difference is zero. However, as Kn values increase for a given flow, a temperature jump occurs and the normal continuum assumption becomes invalid. As should be expected, simulation results of the current study reveal a significant temperature difference between the wire and the adjacent gas for moderate Kn values. Several studies have accounted for temperature jump using a first order approximation of temperature jump at the wire surface [5, 15, 31]. These results have proven valuable for the slip-flow regime, but accuracy degrades as Kn increases into the transition regime. No known studies have thoroughly investigated temperature jump around fine-wires in the transition regime. The reason for this lack in the literature is due to the difficulty or inability to measure this temperature jump experimentally, and the relative lack of numerical simulation studies of fine-wires in this regime. Results presented illustrate that the classical approach to nondimensionalizing power loss in the continuum regime is not appropriate for the transition and free-molecular regimes. A discussion of results for hotwire heat transfer in light of this temperature jump is presented in the final section.

Temperature jump is the temperature of the gas immediately adjacent to the wire. For subsonic flow with no chemical reactions, the temperature of the fluid surrounding the wire can be expected to lie in the range of $T_\infty \geq T \geq T_w$. A reasonable dimensionless representation of the

temperature jump surrounding the wire is then

$$T_j^* = \frac{T_j - T_\infty}{T_w - T_\infty}. \tag{7.1}$$

For the present DSMC simulations, temperature data is output on a per-collision cell basis. Practically speaking, many different definitions of temperature jump could be used. For the current work, temperature jump has been defined as the average temperature of all collision cells whose center lies within one mean free path of the surface. The mean free path for this purpose is calculated based on the free stream conditions. This definition ensures that data from several collision cells will be included because collision cells are sized to be less than 1/2 the mean free path in width and height. Figure 7.1 illustrates the algorithm used for identifying collision cells from which temperature jump is calculated. A minimum radius is required in the algorithm to ensure that cells which are entirely or mostly contained within the wire are not included in the calculation of T_j. After the cells near the wire are identified with this algorithm, the average and standard deviation of thermal temperature of the cells is calculated. Steady state data is calculated as the average T_j for all steady state output data. The uncertainty of the steady state data is taken as the quadrature sum of the average standard deviations from all data sets and the standard deviation of the time-varying T_j data. All temperature jump data presented herein is presented as a point representing this time average and uncertainty bars representing that quadrature summed uncertainty.

7.1.1 Influence of Domain Size on Simulated Temperature Jump

A study of the impact of domain size on results for temperature jump was conducted. Results for T_j^* as a function of domain size are shown in Figure 7.2 for various Kn values. A positive relationship between domain size and temperature jump is observed for all data sets over the range of domain sizes used. The relationship is relatively weak, however. Dependence on domain size increases with decreasing values of Kn. Values of T_j^* for the largest three domain sizes lie within each other's uncertainty bounds for each case. Results presented in subsequent sections are from

simulations where $L/d = 100$.

7.2 Empirical Model for Transition Regime Temperature Jump

As discussed above, it should be expected for the flows of interest to the current work that values of T_j^* should lie between 0 and 1. As Kn $\to 0$, it should be expected that $T_j^* \to 1$. This is the standard assumption made when analyzing most hotwire data to-date. As Kn $\to \infty$, it should be expected that $T_j^* \to 0$. This is reasonable because as Kn gets very large, a vanishing number of particles collide with the surface. Those particles which do collide with the surface travel a relatively far distance away from the wire before colliding with other particles. Therefore, particles reflecting off the surface have a negligible impact on the average temperature of gas particles near the surface. In the transition regime between these two limits, the value of T_j^* must decrease with increasing Kn.

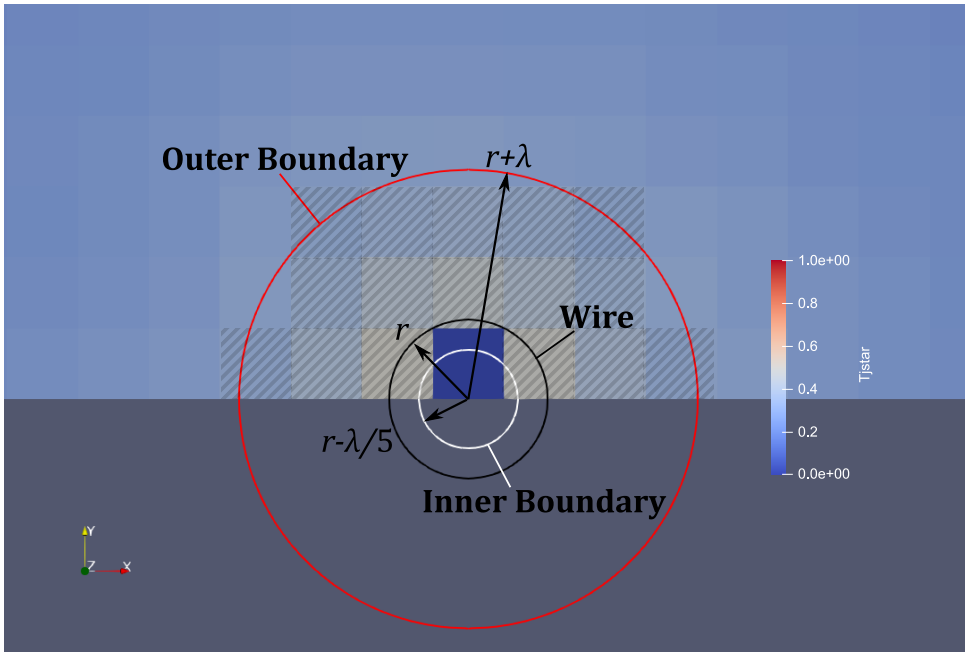

Figure 7.1: Schematic illustrating the method for calculating temperature jump from DSMC data. The outer and inner boundaries define the region where DSMC data is selected. λ is the mean free path calculated at free stream conditions. Hashed cells indicate those chosen for calculating the temperature jump in the given example.

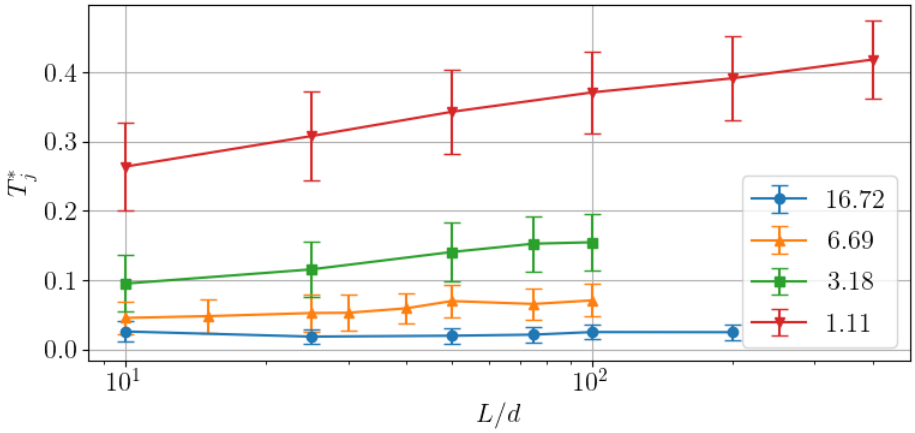

Figure 7.2: Temperature jump results for simulations with various domain sizes. The legend indicates the free stream value of Kn for each set of data.

A model has been developed for T_j^* from DSMC data. The model equation is given by

$$T_j^* = \frac{1}{2}\text{erfc}\left(A + B \times \ln\left(\frac{\text{Kn}_{jf}}{\alpha}\right)\right) \tag{7.2}$$

where erfc() is the complementary error function, A and B are calibration constants, α is the surface accommodation coefficient, and Kn_{jf} is the value for Kn calculated using the jump film temperature, $T_{jf} = 0.5(T_j + T_\infty)$. For purposes of calculating the calibration parameters A and B, the model can be rearranged as

$$\text{erfc}^{-1}\left(2T_j^*\right) = A + B \times \ln\left(\frac{\text{Kn}_{jf}}{\alpha}\right). \tag{7.3}$$

In this form, the values of A and B can be found using linear least squares optimization applied to data for T_j^*. DSMC simulation data has been used to calculate these parameters. The simulation data used had a flow velocity of 3 m/s, $\alpha = 0.7$, 0.85, and 1, $T_w = 373.15$, $T_\infty = 300$, and the simulated gas is N_2. The data and model with optimal parameters are shown in Figure 7.3. The calculated parameter values for the model are $A = 0.111$ and $B = 0.461$. The model appears to very accurately represent the variation of temperature jump with Kn. For all data points, the model is within the uncertainty of the DSMC data.

This temperature jump model is defined based on the value for Kn calculated from the film

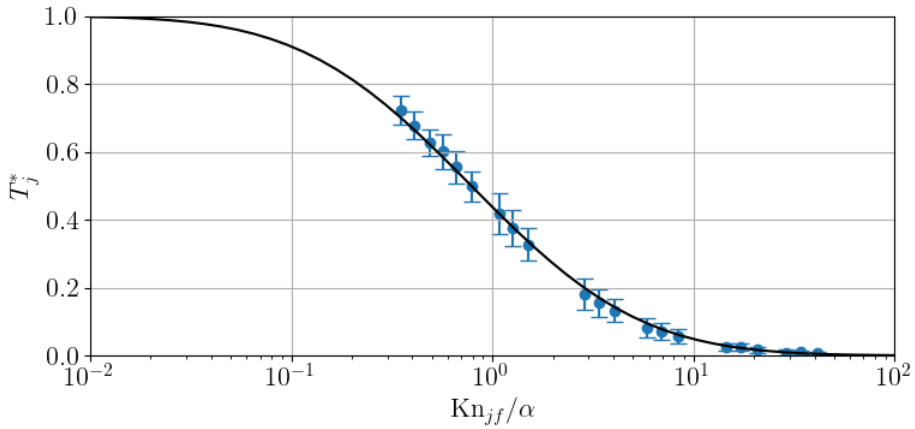

Figure 7.3: DSMC temperature jump data from simulations run with various values of P and α. The black line is the best fit complementary error function model shown in Equation 7.2.

temperature predicted by the model. This means that a strict use of the model requires an iterative procedure. One example for such a procedure is described below.

(1) Calculate the value for Kn based on λ_∞

(2) Use Equation 7.2 to calculate T_j^* for the current Kn value

(3) Calculate the film temperature by

$$T_{jf} = T_\infty + \frac{T_j^*}{2}(T_w - T_\infty) \tag{7.4}$$

(4) Calculate the value for Kn based on $\lambda_{jf} = \lambda(T_{jf})$

(5) Repeat steps 2 - 4 until convergence

For many engineering applications, it would probably be sufficient to simply use the Kn value calculated from the film or free stream temperature mean free path. Since mean free path is a function of temperature, the accuracy of this approach will depended on the magnitude of the temperature difference between the wire and the free stream, with larger temperature differences leading to more potential error.

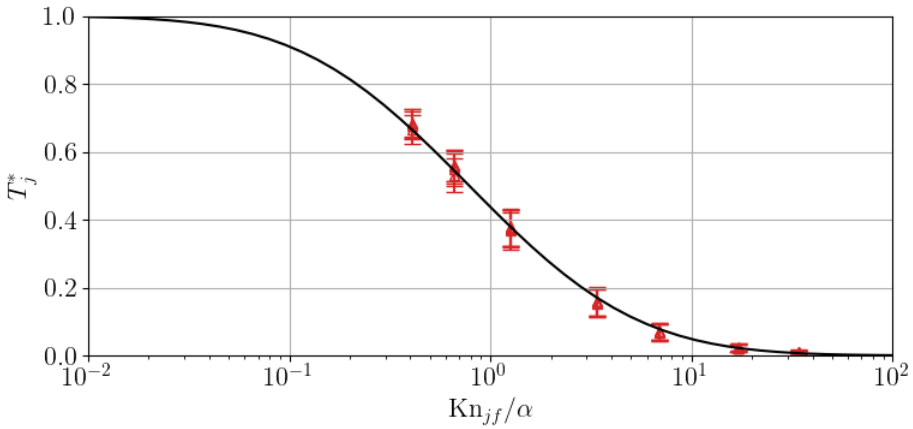

Figure 7.4: DSMC temperature jump data from simulations run with various values of P and U. The black line is the model shown in Figure 7.3.

The above model was compared with a number of other simulation results in order to explore its general applicability. Figure 7.4 compares the model (black line) with simulations run with velocities ranging from 0 to 8 m/s and $\alpha = 0.85$. All other simulation parameters were the same as those for the data from which the model was derived. Excellent agreement is observed, with the model predicting within the uncertainty of each DSMC data point. It should be noted that this model is not expected to apply at significantly higher velocities. In supersonic flow, for example, temperatures around the wire will be higher than the free stream because of the shock wave that would form upstream of the wire.

Dependence of temperature jump on wire temperature was also explored. Figure 7.5 shows simulation results for wire temperatures of 335 K (green squares) and 301 K (blue x) with $\alpha = 0.85$ and a velocity of 3 m/s. Very good agreement is observed. The very low wire temperature case has significant uncertainty because of the low signal to noise ratio of the DSMC simulation. It can be concluded, at the very least, that the low wire temperature data does not contradict the model. Practically speaking, the above temperature jump model would likely never be needed for cases with a very low overheat because fluid properties in such a flow field are effectively constant.

Lastly, dependence of temperature jump on the gas species was explored. Figure 7.6 shows

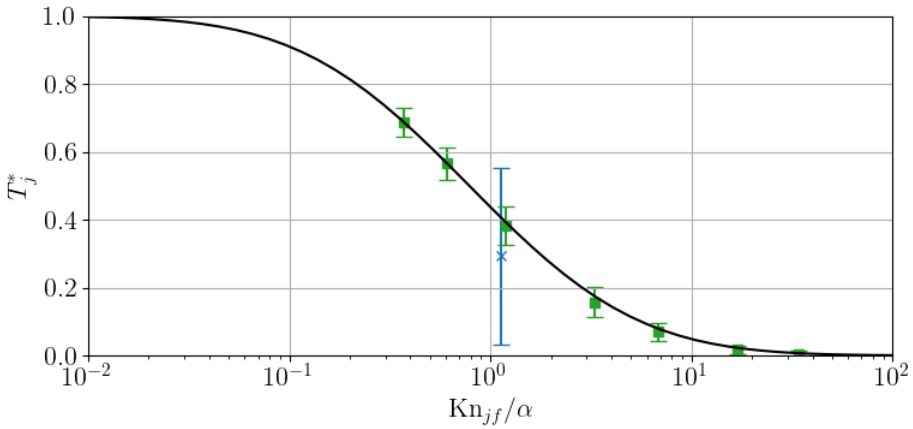

Figure 7.5: DSMC temperature jump data from simulations run with various values of P and T_w. Data for $T_w - T_\infty$ values of 73.15 K (green squares) and 1 K (blue x) are shown. The black line is the model shown in Figure 7.3.

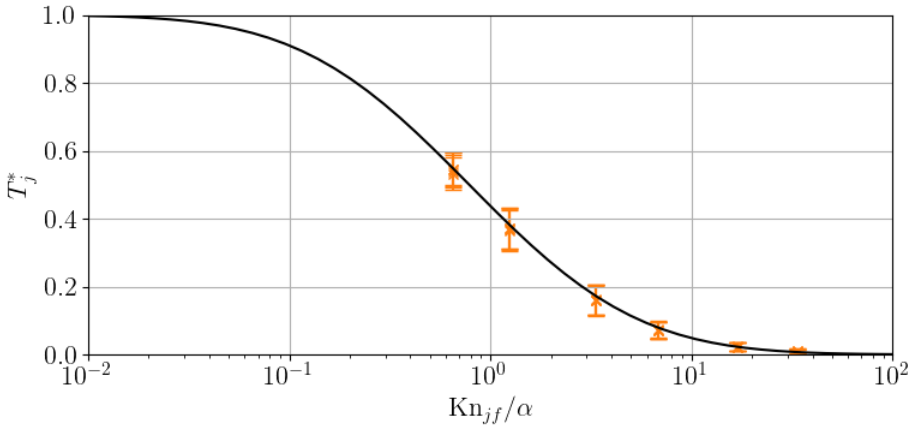

Figure 7.6: DSMC temperature jump data from simulations of Argon. Uncertainty bars indicate $\pm 1\sigma$ of the steady state DSMC data. The wire overheat is $T_w - T_\infty = 73.15$ K. The black line is the model shown in Figure 7.3.

results from simulations of Argon with $\alpha = 0.85$ and a velocity of 3 m/s. Once again, the model predicts the temperature jump to within the uncertainty of the DSMC data. This observation is interesting in light of the observation made above that the wire heat transfer rate from simulations of Argon and N_2 is significantly different. The current data suggests that temperature jump is a more universal feature of the flow than power loss.

7.2.1 Temperature Jump Model Limitations

The domain convergence study presented above shows a weak dependence of T_j^* on domain size for lower values of Kn, but that data suggests that the model may under predict temperature jump in the middle part of the transition regime where $\mathrm{Kn}_{jf} \sim 1$.

For Kn values simulated here, temperature jump around the wire is uniform, which makes it appropriate to characterize T_j with a single value. For lower Kn cases or for higher flow speeds, it should be expected that the upstream and downstream portions of the wire may experience different values of temperature jump because of the significantly different temperature gradients that would occur in those regions [10]. Because of this, it is only recommended that the model be used for the transition regime range considered ($\mathrm{Kn}_{jf}/\alpha \geq 0.3$), and for flow speeds near those simulated here ($U < 10$ m/s). Application of this model outside of that range may be appropriate but further validation is required.

The dependence of T_j^* on accommodation coefficient was successfully taken into account by dividing the value of Kn_{jf} by α. Simulations here only included $\alpha = 0.7$, 0.85, and 1.0. This range covers measured values of α for many engineering surfaces. Error may be introduced if this model is applied for values of α lower than 0.7. However, the model does predict the logical trend that as $\alpha \to 0$, $T_j^* \to 0$ for all values Kn. Further testing is required to determine if the model can be accurately applied to lower values of α.

7.3 Discussion of Temperature Jump Results

Temperature jump is important in the analysis of fine-wires for at least two notable reasons. The first is that typical heat transfer models evaluate gas properties at the so-called film temperature of the gas which is equal to the arithmetic mean of the wire and free stream temperatures. This has been shown to effectively collapse much of the experimental data that exists for fine-wire heat transfer in flows of various gases at various wire temperatures. However, the phenomena of temperature jump in the transition regime suggests that nondimensionalizing heat transfer by film

temperature properties is not appropriate. This can also be reasoned by considering the extreme case of free-molecular flow. In free-molecular flow, the only gas molecules impacting the wire are those of the free stream. Particles which reflect off the surface do not influence the free stream particles because free-molecular flow is defined by the lack of collisions. It is therefore reasonable that only free stream fluid properties need to be considered in nondimensionalizing free-molecular fine-wire heat transfer. The temperature jump model presented can smoothly bridge the continuum and free-molecular cases. Through the transition regime, the model smoothly transitions the property evaluation temperature (T_{jf}) from the traditional film temperature in the continuum regime ($T_{jf} = T_f$) to the free stream temperature in the free-molecular regime ($T_{jf} = T_\infty$).

As an example of this application, data from Figure 6.14 was recalculated using fluid properties evaluated at the jump film temperature T_{jf} rather than the film temperature as was originally done. The procedure outlined in Section 7.2 was used to iteratively calculate T_{jf} for each data point. Recalculated data is shown with filled markers in Figure 7.7. Note that only differences with free-molecular theory were recalculated. Differences with the empirical model from [63] were not adjusted because the model is based on evaluating properties at the film temperature. Modifying that model would require reprocessing their experimental data using the present temperature jump model.

By using the temperature jump model, simulation results are shifted such that the difference with the free-molecular solution is now less than 10% for $\mathrm{Kn}_{jf} > 4$ and less than 5% for $\mathrm{Kn}_{jf} > 9$. This new analysis lowers the altitude at which free-molecular theory could be sufficiently accurate for processing fine-wire data, and it further supports the previously stated prediction that $\partial \mathrm{Nu}/\partial \mathrm{Re} = 0$ at some altitude between 40 and 50 km for the HYFLITS system.

Data where $T_w - T_\infty = 35$ K (squares) is shifted less than data where $T_w - T_\infty = 73$ K (circles). Data is also shifted less at lower values of Kn. Both of these observations are due to the fact that, for a given fluid with temperature dependent properties, the magnitude of the impact of using this model scales with the difference between T_f and the model predicted value of T_{jf}. This difference is small for lower values of $T_w - T_\infty$ and at lower values of Kn. Based on the results

in Figure 7.7, it is expected that using the temperature jump model for the HYFLITS fine-wire system will have a negligible impact on results because $T_w - T_\infty \approx 35$ K for the hotwire instrument, and most measurements to-date have been collected at altitudes below 35 km.

The temperature jump model could be applied to the other results presented in this work as most of the data has been presented in terms of properties evaluated at the film temperature (indicated by the subscript f). Based on the discussion here, it is expected that results for higher $T_w - T_\infty$ values and higher Kn values may be appreciably modified. Reanalyzing the present data and quantifying the impact of using the temperature jump model is an area of future work.

The second reason that temperature jump is important for fine-wires is that it highlights important differences between the molecular model of gases, and the continuum model. In the continuum, energy transfer through a fluid is modeled by thermal conductivity and Fourier's Law. As $T_j^* \to 0$, the temperature gradient must also go to zero. Additionally, thermal conductivity, which is fundamentally due to intermolecular collisions, also must go to zero in the free-molecular limit. According to the continuum model, both of these limiting behaviors suggest that heat transfer goes to zero as the Kn value increases to the collisionless flow regime. This, however, is not the case. Heat transfer between the wire and gas becomes independent of the thermal conductivity

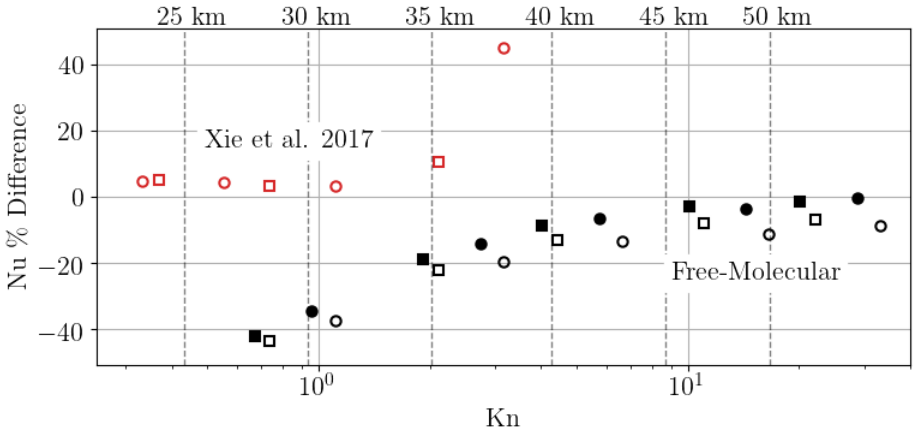

Figure 7.7: Same as Figure 6.14 with the addition of filled markers that show data normalized by fluid properties calculated at the jump film temperature according to the model shown in Figure 7.3.

in the free-molecular regime as can be seen in the respective solution for heat transfer shown in Equation 3.9. The temperature jump data and the discussion here further supports the idea presented in Chapter 3 that Nu is not the most physically relevant expression for heat transfer in rarefied flows. Fully developing a more physically appropriate set of dimensionless parameters for fine-wire heat transfer in rarefied flows can be a topic for future study.

7.4 Summary and Conclusions

Temperature jump data for heated fine-wires through the transition regime were presented and discussed in this chapter. An empirical model for temperature jump was derived from simulations of N_2 in a 3 m/s flow. The model was validated for various flow velocities, surface accommodation coefficients, wire temperatures, and gas compositions. Significant temperature jump at the wire surface means that evaluating fluid properties at the film temperature is not appropriate for fine-wires in the transition regime. The presented empirical model can be used to calculate a jump film temperature which is appropriate for calculating fluid properties. Data from Section 6.6 in the previous chapter is reanalyzed using the temperature jump model. Results are shifted such that the difference with free-molecular theory is less than 10% for Kn values above 4 or altitudes above 40 km for the HYFLITS system. The importance of using the temperature jump model scales with the values for Kn and $T_w - T_\infty$. For most data collected on the HYFLITS campaign, Kn < 2 and $T_w - T_\infty \approx 35$ K. For these conditions, negligible error is introduced if the temperature jump at the wire surface is ignored.

Chapter 8

Conclusions and Future Work

This work presents the results of a numerical simulation study of heated fine-wires in low-speed, rarefied flows. Motivation comes from the need for measurements of stratospheric turbulence. From this motivation, the following two research questions arise.

(1) Can current empirical models for transition regime wire power loss be accurately used for analyzing data from fine-wires in the stratosphere?

(2) How does power loss depend on free stream velocity for fine-wires from the transition regime to the free-molecular flow regime?

With regard to the first question, it was found that the empirical model from [63] can be accurately used up to an altitude of about 35 km or a fine-wire Knudsen value of about 2. Free-molecular flow theory can be accurately used above an altitude of about 45 km or a fine-wire Knudsen value of about 10. With regard to the second question, it was found that, at low flow velocities, the derivative of convective power loss with respect to flow velocity is positive in the continuum regime, negative in the free-molecular regime, and, therefor, must be zero somewhere in the transition regime. Thermal anemometry cannot be used to measure velocity fluctuations where wire power loss is independent of flow velocity. It is expected that this occurs at some altitude between 40 and 50 km for the HYFLITS measurement system.

Scientific and engineering contributions of the current work include:

(1) Development of an implicit target mass flow boundary condition for low-speed DSMC (Chapter 4)

(2) Evaluation of simulation accuracy for predicting fine-wire power loss in low-speed rarefied flows (Chapter 5)

(3) Verification of an empirical power loss model for fine-wires in the transition regime (Chapter 6)

(4) Characterization of fine-wire power loss from the transition to free-molecular flow regimes (Chapter 6)

(5) Empirical model for fine-wire temperature jump from the transition to free-molecular regimes (Chapter 7)

8.1 Summary of Results

A review of numerical methodologies for simulating transition regime flow is presented. Direct Boltzmann Solvers appear most suited for simulating low-speed transition regime simulations, however, there is no available simulation software and much development is needed before a code could be applied to general problems. As discrete velocity methods become available and mature, their reduced statistical scatter and computational cost relative to DSMC may make them more appropriate than DSMC for the flows of interest here. The DSMC method remains the most accurate, generally applicable, and available method for transition regime simulations. Therefore, the DSMC method serves as the primary simulation tool for this work.

The DSMC method is well suited for simulations of high-speed flows, but particular care must be taken in the choice of boundary conditions for low-speed DSMC simulations. Analysis and discussion of boundary conditions for low-speed DSMC simulations is included. A target mass flow rate boundary condition for low-speed DSMC is presented. Preliminary results using the new condition show good performance, but further tuning and characterization of the condition is

required before it can be generally applied.

Results for wire heat transfer from DSMC simulations are shown to be strongly dependent on the computational domain size. Convergence of results is not achieved even for domain sizes that push the limits of an available supercomputer resource. The dependence of simulated fine-wire heat transfer is characterized with respect to simulated Reynolds and Knudsen numbers. Stronger dependence is observed for simulations of high Knudsen number and low Reynolds number flows. A domain convergence extrapolation method to correct results for the domain size effect is discussed, though results show that the method can produce unrealistic corrections at lower simulated velocities.

A thorough investigation of the fine-wire parameter space is conducted. In particular, the sensitivity of heat transfer to flow speed, surface accommodation coefficient, gas composition, and temperatures is explored. From the results presented, it can be concluded that currently available empirical power loss models can be accurately used to process turbulence data collected for the HYFLITS campaign at altitudes up to about 35 km. Results for Kn values corresponding to higher altitudes diverge significantly from empirical models. It is also observed that, for low-Re values, the value of $\partial \mathrm{Nu}/\partial \mathrm{Re}$ is positive in the continuum regime, negative in the free-molecular flow regime, and, therefore, must be zero somewhere in transition regime. Thermal anemometry cannot be used to measure turbulence where $\partial \mathrm{Nu}/\partial \mathrm{Re} = 0$. Based on a comparison of simulation results with free-molecular theory, it is predicted that this point occurs at some altitude between 40 and 50 km for the HYFLITS fine-wire measurement system.

Finally, the temperature jump around fine-wires through the transition regime is investigated. As could be expected, the data show that temperature jump increases through the transition regime. This suggests that classical heat transfer models based on evaluating fluid properties at the film temperature are not appropriate and may introduce significant errors for fine-wires with a high temperature loading. An empirical model for temperature jump derived from simulation data is presented and analyzed. Applicability of the model over a range of wire temperatures, gas compositions, surface accommodation coefficients, and flow velocities is demonstrated. This model

can be used to calculate fluid properties at the appropriate temperature throughout the transition regime.

8.2 Future Work

Several areas for future work flow from the current study for both low-speed transition regime simulations and the characterization of fine-wire power loss in the transition regime.

The DSMC simulation method is robust in its physical accuracy and general applicability, but the method is computationally expensive for low-speed aerodynamic flows. Alternative methods for simulating the transition regime have been developed, but models and codes still need significant development. In particular, Direct Boltzmann Solvers appear best suited for simulating transition regime fine-wires in low-speed flows, but no general-use codes are available, and most implementations can only be applied to Cartesian computational grids.

In the HYFLITS measurement system, cold-wires are operated with a very low overheat value ($T_w - T_\infty \approx 1$ K) to measure fluctuations in free stream temperature. The heat transfer signals when operating in this cold-wire mode are relatively small, and some have questioned if any measurable change in heat transfer occurs at all. The simulation methodology presented here could be used to investigate the dependence of heat transfer on free stream temperature changes for low temperature wires. Cold-wire simulations, however, are different in several important ways from the hotwire simulations presented. The first challenge to be addressed is that the signal to noise ratio for DSMC simulations of cold-wires is very low. This results in significant uncertainty in simulation data. Much larger simulated particle densities or longer steady state sampling periods will be needed to reduce statistical scatter to a reasonable level. It is difficult to say how the domain size dependence of results will be different from the present hotwire simulations. On the one hand, the difference in temperature between the wire and free stream boundaries is much smaller, so it stands to reason that smaller domains would be needed. On the other hand, the energy transfer from the surface to the gas is also much smaller, so the small expected bias from the finite domain size could still be large relative to the wire heat transfer. Domain size studies

similar to those presented here would therefore be needed for cold-wire simulations. The need for cold-wire simulations provides further motivation for developing a Direct Boltzmann Solver which is deterministic and so does not have statistical noise. In fact, cold-wire simulations are more suited for such a solver than hotwire simulations because the velocity space is relatively small, and variation of gas properties with temperature can be ignored.

Initial results for the target mass flow boundary condition serve as a proof of concept that the method can work to achieve a desired mass flow rate. However, modifications need to be made in order to improve results. In particular, the method should be adjusted such that mass flow rate through the boundary DSMC collision cells is used to calculate the pressure correction, rather than the ghost cell mass flow rate. Additional tuning of the method is also needed to allow for the implicit calculation of temperature at the boundary.

Analysis of the influence of domain size on simulation results highlights several potential avenues for future work. Further refinement of the domain convergence method to account for finite domain size bias could lead to a generally applicable methodology. Computational cost of very large DSMC simulation domains could be reduced by the development of variable simulated particle density simulations (variable f_{num}). Further development of coupled CFD/DSMC simulation codes could also enable the simulation of domains large enough to eliminate the influence of domain size.

It was observed in the current work that, for low-Re values, the value of $\partial \mathrm{Nu}/\partial \mathrm{Re}$ is zero somewhere in transition regime. Thermal anemometry cannot be used to measure turbulence where $\partial \mathrm{Nu}/\partial \mathrm{Re} = 0$. It is therefore important to accurately characterize where this occurs with respect to Reynolds number and Knudsen number so that fine-wire measurement systems can be designed to avoid these conditions.

Temperature jump data presented show that film temperature fluid properties are not appropriate for nondimensionalizing fine-wire data in the transition regime. Since most of the data presented in this work was normalized using film temperature fluid properties, reanalyzing results using the temperature jump model may adjust some of the data presented. Future studies should explore how the presented temperature jump model should be used and quantify when it is neces-

sary.

Finally, no generalized or continuous models of fine-wire heat transfer through the transition regime have been developed. The model presented in [63] is useful for limited engineering applications, but is discontinuous across different Kn regimes and significantly diverges from simulation data for Kn values above about 2. The data and analyses presented here lay the ground work for developing a complete model of fine-wire heat transfer in the transition regime for low-speed flows. The known biases of the present DSMC simulations prevent its use to directly develop models of heat transfer with respect to flow velocity for flows in the middle transition regime. However, because accuracy increases with Knudsen number, simulations can be used to accurately predict the approach to free-molecular conditions and the point where free-molecular theory can be applied. Slip and transition regime experimental data could be used along with DSMC and free-molecular theory to develop a coherent and continuous model for transition regime fine-wire heat transfer.

Bibliography

[1] U.s. standard atmosphere. Technical Report NASA-TM-X-74335, National Aeronautics and Space Administration, October 1976.

[2] Y. Aihara, D. R. Kassoy, and Paul A. Libby. Heat transfer from circular cylinders at low reynolds numbers. II. experimental results and comparison with theory. Physics of Fluids, 10(5):947, 1967.

[3] I. Amdur and L. A. Guildner. Thermal accommodation coefficients on gas-covered tungsten, nickel and platinum1. Journal of the American Chemical Society, 79(2):311–315, jan 1957.

[4] Jonathon Anderson, Patrick J. Burns, Daniel Milroy, Peter Ruprecht, Thomas Hauser, and Howard Jay Siegel. Deploying RMACC summit. In Proceedings of the Practice and Experience in Advanced Research Computing 2017 on Sustainability, Success and Impact. ACM, jul 2017.

[5] G.E Andrews, D Bradley, and G.F Hundy. Hot wire anemometer calibration for measurements of small gas velocities. International Journal of Heat and Mass Transfer, 15(10):1765–1786, oct 1972.

[6] Lionel V. Baldwin, Virgil A. Sandborn, and James C. Laurence. Heat transfer from transverse and yawed cylinders in continuum, slip, and free molecule air flows. Journal of Heat Transfer, 82(2):77–86, may 1960.

[7] Ram Prakash Bharti, R. P. Chhabra, and V. Eswaran. A numerical study of the steady forced convection heat transfer from an unconfined circular cylinder. Heat and Mass Transfer, 43(7):639–648, jul 2006.

[8] G. Bird. Molecular Gas Dynamics and the Direct Simulation of Gas Flows. Oxford University Press, 1994.

[9] Chunpei Cai, Iain D. Boyd, Jing Fan, and Graham V. Candler. Direct simulation methods for low-speed microchannel flows. Journal of Thermophysics and Heat Transfer, 14(3):368–378, jul 2000.

[10] M. Cevdet Çelenligil. Heat transfer simulation of rarefied laminar flow past a circular cylinder. In AIP Conference Proceedings, 2016.

[11] Paul A. Chambre and Samuel A. Schaaf. Flow of Rarefied Gases. Princeton University Press, 1961.

[12] S.H.P. Chen and S.C. Saxena. Interface heat transfer and thermal accommodation coefficients: Heated tungsten wire in nitrogen environment. International Journal of Heat and Mass Transfer, 17(2):185–196, feb 1974.

[13] Peter Clarke, Philip Varghese, and David Goldstein. A low noise discrete velocity method for the boltzmann equation with quantized rotational and vibrational energy. Journal of Computational Physics, 352:326–340, jan 2018.

[14] J. Cole and A. Roshko. Heat transfer from wires at reynolds numbers in the oseen range. In Proceedings of the Heat Transfer and Fluid Mechanics Institute, pages 13–23, 1954.

[15] D. C. Collis and M. J. Williams. Two-dimensional convection from heated wires at low reynolds numbers. Journal of Fluid Mechanics, 6(03):357, oct 1959.

[16] M. R. Davis and P. O. A. L. Davies. Factors influencing the heat transfer from cylindrical anemometer probes. International Journal of Heat and Mass Transfer, 15(9):1659–1677, sep 1972.

[17] R.G. Deissler. An analysis of second-order slip flow and temperature-jump boundary conditions for rarefied gases. International Journal of Heat and Mass Transfer, 7(6):681–694, jun 1964.

[18] S. C. R. Dennis. Steady laminar forced convection from a circular cylinder at low reynolds numbers. Physics of Fluids, 11(5):933, 1968.

[19] Arnold Eucken. Über das wärmeleitvermögen, die spezifische wärme und die innere reibung der gase. Phys. Z, 14(8):324–332, 1913.

[20] Jing Fan and Ching Shen. Statistical simulation of low-speed rarefied gas flows. Journal of Computational Physics, 167(2):393–412, mar 2001.

[21] Rod Frehlich, Yannick Meillier, Michael L. Jensen, and Ben Balsley. Turbulence measurements with the CIRES tethered lifting system during CASES-99: Calibration and spectral analysis of temperature and velocity. Journal of the Atmospheric Sciences, 60(20):2487–2495, oct 2003.

[22] Irene M. Gamba and Sergej Rjasanow. Galerkin–petrov approach for the boltzmann equation. Journal of Computational Physics, 366:341–365, aug 2018.

[23] F.O. Goodman. Thermal accommodation. Progress in Surface Science, 5:261–375, jan 1974.

[24] Harold Grad. On the kinetic theory of rarefied gases. Communications on Pure and Applied Mathematics, 2(4):331–407, dec 1949.

[25] Xiao-Jun Gu, Robert W. Barber, Benzi John, and David R. Emerson. Non-equilibrium effects on flow past a circular cylinder in the slip and early transition regime. Journal of Fluid Mechanics, 860:654–681, dec 2018.

[26] Xiao-Jun Gu and David R. Emerson. A high-order moment approach for capturing non-equilibrium phenomena in the transition regime. Journal of Fluid Mechanics, 636:177–216, sep 2009.

[27] Zhaoli Guo, T. S. Zhao, and Yong Shi. Physical symmetry, spatial accuracy, and relaxation time of the lattice boltzmann equation for microgas flows. Journal of Applied Physics, 99(7):074903, apr 2006.

[28] Yuan Hu, Quanhua Sun, and Jing Fan. Simulation of gas flow over a micro cylinder. In ASME 2009 Second International Conference on Micro/Nanoscale Heat and Mass Transfer, Volume 1. ASMEDC, jan 2009.

[29] Shashank Jaiswal, Alina A. Alexeenko, and Jingwei Hu. A discontinuous galerkin fast spectral method for the full boltzmann equation with general collision kernels. Journal of Computational Physics, 378:178–208, feb 2019.

[30] George EM Karniadakis. Numerical simulation of forced convection heat transfer from a cylinder in crossflow. International Journal of Heat and Mass Transfer, 31(1):107–118, jan 1988.

[31] D. R. Kassoy. Heat transfer from circular cylinders at low reynolds numbers. i. theory for variable property flow. Physics of Fluids, 10(5):938, 1967.

[32] Louis Vessot King. XII. on the convection of heat from small cylinders in a stream of fluid: Determination of the convection constants of small platinum wires with applications to hot-wire anemometry. Philosophical Transactions of the Royal Society of London. Series A, Containing Papers of a Mathematical or Physical Character, 214(509-522):373–432, jan 1914.

[33] Timm Krüger, Halim Kusumaatmaja, Alexandr Kuzmin, Orest Shardt, Goncalo Silva, and Erlend Magnus Viggen. The Lattice Boltzmann Method. Springer International Publishing, 2017.

[34] C.F. Lange, F. Durst, and M. Breuer. Momentum and heat transfer from cylinders in laminar crossflow at 10-4 $\leqslant$ re $\leqslant$ 200. International Journal of Heat and Mass Transfer, 41(22):3409–3430, nov 1998.

[35] Q. Li, Y. L. He, G. H. Tang, and W. Q. Tao. Lattice boltzmann modeling of microchannel flows in the transition flow regime. Microfluidics and Nanofluidics, 10(3):607–618, oct 2010.

[36] W. W. Liou and Y. C. Fang. Implicit boundary conditions for direct simulation monte carlo method in mems flow predictions. Computer Modeling in Engineering & Science, 1(4):119–128, 2000.

[37] Qing Liu and Xiang-Bo Feng. Numerical modelling of microchannel gas flows in the transition flow regime using the cascaded lattice boltzmann method. Entropy, 22(1):41, dec 2019.

[38] Elham Maghsoudi, Michael James Martin, and Ram Devireddy. Momentum and heat transfer in laminar slip flow over a cylinder. Journal of Thermophysics and Heat Transfer, 27(4):607–614, oct 2013.

[39] Amir-Mehran Mahdavi, Nam T. P. Le, Ehsan Roohi, and Craig White. Thermal rarefied gas flow investigations through micro-/nano-backward-facing step: Comparison of DSMC and CFD subject to hybrid slip and jump boundary conditions. Numerical Heat Transfer, Part A: Applications, 66(7):733–755, jun 2014.

[40] Luke J. Melander and Graham V. Candler. Investigation of atmospheric turbulence and shock interaction for a hypersonic sphere-cone. In AIAA Scitech 2021 Forum. American Institute of Aeronautics and Astronautics, jan 2021.

[41] Luc Mieussens. A survey of deterministic solvers for rarefied flows. AIP Publishing LLC, 2014.

[42] A. B. Morris, P. L. Varghese, D. B. Goldstein, and Takashi Abe. Improvement of a discrete velocity boltzmann equation solver with arbitrary post-collision velocities. In AIP Conference Proceedings. AIP, 2008.

[43] A.B. Morris, P.L. Varghese, and D.B. Goldstein. Monte carlo solution of the boltzmann equation via a discrete velocity model. Journal of Computational Physics, 230(4):1265–1280, feb 2011.

[44] Robert P. Nance, David B. Hash, and H. A. Hassan. Role of boundary conditions in monte carlo simulation of microelectromechanical systems. Journal of Thermophysics and Heat Transfer, 12(3):447–449, jul 1998.

[45] Georgii Oblapenko, David B. Goldstein, Philip Varghese, and Christopher Moore. Modeling of ionized gas flows with a velocity-space hybrid boltzmann solver. In AIAA Scitech 2021 Forum. American Institute of Aeronautics and Astronautics, jan 2021.

[46] Lorenzo Pareschi and Benoit Perthame. A fourier spectral method for homogeneous boltzmann equations. Transport Theory and Statistical Physics, 25(3-5):369–382, apr 1996.

[47] S. J. Plimpton, S. G. Moore, A. Borner, A. K. Stagg, T. P. Koehler, J. R. Torczynski, and M. A. Gallis. Direct simulation monte carlo on petaflop supercomputers and beyond. Physics of Fluids, 31(8):086101, aug 2019.

[48] Yasvanth Poondla, Philip Varghese, David Goldstein, and Kyle Higdon. Modeling of chemical reactions using quasi-particle simulation (QuiPS). In 31ST INTERNATIONAL SYMPOSIUM ON RAREFIED GAS DYNAMICS: RGD31. AIP Publishing, 2019.

[49] Savio Poovathingal, Eric C. Stern, Ioannis Nompelis, Thomas E. Schwartzentruber, and Graham V. Candler. Nonequilibrium flow through porous thermal protection materials, part II: Oxidation and pyrolysis. Journal of Computational Physics, 380:427–441, mar 2019.

[50] Mikhail Aleksandrovich Pugach, Alexander Aleksandrovich Ryzhov, and Alexander Vitalyevich Fedorov. Estimation of the effect of free-stream turbulence and solid particles on the laminar-turbulent transition at hypersonic speeds. TsAGI Science Journal, 47(1):15–28, 2016.

[51] Christopher A. Roseman, Dale A. Lawrence, Joseph L. Pointer, Steve Borenstein, and Brian M. Argrow. A low-cost balloon system for high-cadence, in-situ stratospheric turbulence measurements. In 2021 AIAA AVIATION Forum. American Institute of Aeronautics and Astronautics, jul 2021.

[52] Christopher A. Roseman, Joseph L. Pointer, Brian Argrow, and Dale A. Lawrence. Experimental and numerical calibration of hotwire anemometers for the study of stratospheric turbulence. In AIAA Scitech 2021 Forum. American Institute of Aeronautics and Astronautics, jan 2021.

[53] Niraj Shah, Abhimanyu Gavasane, Amit Agrawal, and Upendra Bhandarkar. Comparison of various pressure based boundary conditions for three-dimensional subsonic DSMC simulation. Journal of Fluids Engineering, 140(3), oct 2017.

[54] C. Shen, J. Z. Jiang, and J. Fan. Information preservation method for the case of temperature variation. In AIP Conference Proceedings. AIP, 2001.

[55] Eric C. Stern, Savio Poovathingal, Ioannis Nompelis, Thomas E. Schwartzentruber, and Graham V. Candler. Nonequilibrium flow through porous thermal protection materials, part i: Numerical methods. Journal of Computational Physics, 380:408–426, mar 2019.

[56] Henning Struchtrup. Macroscopic Transport Equations for Rarefied Gas Flows. Springer-Verlag GmbH, 2006.

[57] Hongwei Sun and Mohammad Faghri. Effects of rarefaction and compressibility of gaseous flow in microchannel using dsmc. Numerical Heat Transfer, Part A: Applications, 38(2):153–168, aug 2000.

[58] Quanhua Sun, Iain Boyd, and Jing Fan. Development of an information preservation method for subsonic, micro-scale gas flows. In AIP Conference Proceedings. AIP, 2001.

[59] Quanhua Sun and Iain D. Boyd. A direct simulation method for subsonic, microscale gas flows. Journal of Computational Physics, 179(2):400–425, jul 2002.

[60] K.C. Tseng, T.C. Kuo, S.C. Lin, C.C. Su, and J.S. Wu. Simulations of subsonic vortex-shedding flow past a 2d vertical plate in the near-continuum regime by the parallelized DSMC code. Computer Physics Communications, 183(8):1596–1608, aug 2012.

[61] Martin W. Tysanner and Alejandro L. Garcia. Non-equilibrium behaviour of equilibrium reservoirs in molecular simulations. International Journal for Numerical Methods in Fluids, 48(12):1337–1349, 2005.

[62] Alexander Vazsonyi and Iain Boyd. An axisymmetric direct kinetic solver for simulation of hollow cathode plasmas. In 36th International Electric Propulsion Conference, 09 2019.

[63] Fushou Xie, Yanzhong Li, Zhan Liu, Xinbao Wang, and Lei Wang. A forced convection heat transfer correlation of rarefied gases cross-flowing over a circular cylinder. Experimental Thermal and Fluid Science, 80:327–336, jan 2017.

[64] Fushou Xie, Yanzhong Li, Xingbao Wang, Ying Wang, Gang Lei, and Kewei Xing. Numerical study on flow and heat transfer characteristics of low pressure gas in slip flow regime. International Journal of Thermal Sciences, 124:131–145, feb 2018.

[65] Kyoji Yamamoto and Kazuyuki Sera. Flow of a rarefied gas past a circular cylinder. Physics of Fluids, 28(5):1286, 1985.

[66] L. M. Yang, C. Shu, W. M. Yang, Z. Chen, and H. Dong. An improved discrete velocity method (DVM) for efficient simulation of flows in all flow regimes. Physics of Fluids, 30(6):062005, jun 2018.

[67] Y.-H Zhang, X. J Gu, R. W Barber, and D. R Emerson. Modelling thermal flow in the transition regime using a lattice boltzmann approach. Europhysics Letters (EPL), 77(3):30003, jan 2007.

Appendix A

HYFLITS Fine-Wire Methodology

Investigators for the HYFLITS balloon campaign have derived a methodology for fine-wires to self-calibrate in flight. This self-calibration procedure does not entirely obviate the need for empirical power loss relations, but it does eliminate the need to experimentally calibrate every individual fine-wire instrument, a common practice among experimental researchers. The following methodology is not an essential element of the present work, but it provides background that highlights the motivation and implications of the current work.

A.1 Fine-Wire Model for Measuring Turbulent Fluctuations

The power balance of a fine-wire can be written as

$$\dot{Q}_{gen} = \dot{Q}_c + \dot{Q}_h + c\dot{T}_w \tag{A.1}$$

where c is the heat capacity of the wire and radiation has been ignored. The last term represents the change in energy stored in the wire. This is included for the present methodology because the temperature (resistance) control of the fine-wire circuit is weak. This makes the time-variation of wire temperature non-negligible. Simple linear models are assumed for both $\dot{Q}_c$ and $\dot{Q}_h$ and are given by

$$\dot{Q}_c = H_c(T_w - T_\infty) \tag{A.2}$$

$$\dot{Q}_h = H_h(T_w - T_\infty) \tag{A.3}$$

where the coefficients H_c and H_h are the thermal conductance due to end-conduction and due to convection, respectively. By defining the total wire conductance as

$$H = H_c + H_h \tag{A.4}$$

the wire power balance can be written as

$$\dot{Q}_{gen} = H(T_w - T_\infty) + c\dot{T}_w. \tag{A.5}$$

Considering finite changes due to turbulent fluctuations yields

$$\Delta\dot{Q}_{gen} = \Delta H(\overline{T}_w - \overline{T}_\infty) + \overline{H}\Delta T_w - \overline{H}\Delta T_\infty + c\Delta\dot{T}_w. \tag{A.6}$$

Rearranging gives

$$\Delta H(\overline{T}_w - \overline{T}_\infty) - \overline{H}\Delta T_\infty = \Delta\dot{Q}_{gen} - \overline{H}\Delta T_w - c\Delta\dot{T}_w \tag{A.7}$$

where all terms on the right hand side can be related to measured wire resistance. The value for $\overline{H}$ is periodically estimated in-flight using a chopping procedure. The value for ΔH is dependent on turbulent fluctuations of velocity, ΔT_∞ represents turbulent fluctuations of temperature, and $(\overline{T}_w - \overline{T}_\infty)$ can be calculated from measurements. Using this model, measured fluctuations in wire resistance are used to calculate values for ΔH and ΔT_∞. The temperature structure parameter can be calculated directly from the measurements of ΔT_∞. ΔH must first be related to turbulent velocity fluctuations Δv before turbulent dissipation rate can be estimated. The following section derives the relationship between ΔH and Δv.

A.2 Calculation of Velocity Fluctuations

The relationship between measured fluctuations in thermal conductance ΔH and fluctuations in velocity Δv will now be derived. Ultimately, a model is needed for $\partial H/\partial U$ to convert ΔH to Δv by

$$\Delta v = \left(\frac{\partial H}{\partial U}\right)^{-1} \Delta H \tag{A.8}$$

Note that the inverse of the derivative is shown rather than the inverse derivative simply because models relating wire power loss to flow velocity are typically in a form where the rate of energy transfer is expressed as a function of velocity. Empirical models for convective power loss from a circular cylinder are typically expressed analytically in terms of Reynolds ($\mathrm{Re} = \rho U d/\mu$) and Knudsen ($\mathrm{Kn} = \lambda/d$) number as

$$\mathrm{Nu} = f(\mathrm{Re}, \mathrm{Kn}). \tag{A.9}$$

where Nu is a dimensionless expression for wire power loss and is given by

$$\mathrm{Nu} = \frac{hd}{k} = \frac{\dot{Q}_h}{\pi k L_w (T_w - T_a)}. \tag{A.10}$$

Using Equations A.3 and A.10, convective thermal conductance can be written as

$$H_h = (\pi k L_w)\mathrm{Nu}. \tag{A.11}$$

The derivative of H_h with respect to Nu is

$$\frac{\partial H_h}{\partial \mathrm{Nu}} = \pi k L_w. \tag{A.12}$$

An expression for $\partial\mathrm{Nu}/\partial\mathrm{Re}$ is derived from empirical relations for wire power loss. The derivative of Re with respect to velocity is

$$\frac{\partial \mathrm{Re}}{\partial U} = \frac{\rho d}{\mu}. \tag{A.13}$$

Given the above relations, the dependence of convective thermal conductance on changes in free stream velocity can be written as

$$\frac{\partial H_h}{\partial U} = \frac{\partial H_h}{\partial \mathrm{Nu}} \frac{\partial \mathrm{Nu}}{\partial \mathrm{Re}} \frac{\partial \mathrm{Re}}{\partial U}. \tag{A.14}$$

Total thermal conductance and its derivative with respect to velocity are given by

$$H = H_h + H_c \tag{A.15}$$

$$\frac{\partial H}{\partial U} = \frac{\partial H_h}{\partial U} + \frac{\partial H_c}{\partial U}. \tag{A.16}$$

It is reasoned that end-conduction not a strong function of free stream velocity, and that because the prongs are large relative to the wire, the time rate of change of end-conduction will be slow. With these assumptions, the derivative of H_c can be ignored and the result is

$$\frac{\partial H}{\partial U} = \frac{\partial H_h}{\partial U}. \tag{A.17}$$

This and the above equations lead to a relationship between ΔH and Δv that is given by

$$\Delta v = \left[\frac{\partial H_h}{\partial \mathrm{Nu}}\frac{\partial \mathrm{Nu}}{\partial \mathrm{Re}}\frac{\partial \mathrm{Re}}{\partial U}\right]^{-1}\Delta H \tag{A.18}$$

$$\Delta v = \left[(\pi k L_w)\frac{\partial \mathrm{Nu}}{\partial \mathrm{Re}}\bigg|_{\overline{\mathrm{Re}}}\left(\frac{\rho d}{\mu}\right)\right]^{-1}\Delta H. \tag{A.19}$$

Further consolidation of that expression gives

$$\Delta v = \frac{\mu}{\pi k L_w \rho d}\left(\frac{\partial \mathrm{Nu}}{\partial \mathrm{Re}}\bigg|_{\overline{\mathrm{Re}}}\right)^{-1}\Delta H. \tag{A.20}$$

This equation relates turbulent fluctuations to measured or known quantities. Flow parameters μ, k, and ρ are calculated at the wire film temperature and the ambient pressure. An analytical model for wire temperature as a function of axial position is used to estimate the correct wire and film temperatures. The ideal gas law is used to calculate ρ, Sutherland's law is used to calculate μ, and the model from [1] is used to calculate k. Wire diameter d and length L_w are estimated from measurements of wire resistance and properties of platinum. The derivative of the power loss model $\partial\mathrm{Nu}/\partial\mathrm{Re}$ is calculated at the average wire Reynolds number. Average Reynolds number $\overline{\mathrm{Re}}$ is calculated from the average velocity across the wire $\overline{U}$ and fluid properties described above. The value for $\overline{U}$ is calculated from filtered GPS data and a model for flow blockage due to the wire prongs. It is assumed that prong blockage does not damp turbulent fluctuations of velocity, but only the mean flow velocity across the wire.

The measured values of Δv are then used to calculate turbulent dissipation rate using the procedure outlined in the following section.

A.3 Estimation of Turbulence Dissipation Rate

The following lays out the procedure for calculating turbulence dissipation rate ϵ. First, a Fast-Fourier-Transform (FFT) is applied to a section of time-varying Δv data. For N samples of data (Δv_1, Δv_2,...Δv_n,...,Δv_N) that correspond to N equally spaced points in time (t_1, t_2,...t_n,...,t_N), the FFT of the signal can be written as

$$\mathscr{F}_v(k) = \frac{2}{N}\sum_{n=1}^{N} \Delta v_n \exp\left[-2i\pi(k-1)(n-1)/N\right], 1 \leq k \leq N. \tag{A.21}$$

Note that $\mathscr{F}_v$ is a vector of length N. The $2/N$ term normalizes the FFT so that sinusoidal components up to Nyquist frequency have the correct amplitude. The power spectral density (PSD) of velocity is then obtained by

$$S_v(f) = \frac{t_s}{2}\left(\mathscr{F}_v \odot \mathscr{F}_v^*\right) \tag{A.22}$$

where t_s is the length of the sampling interval in seconds, $\mathscr{F}_v^*$ is the complex conjugate of $\mathscr{F}_v$, and $\odot$ indicates element-by-element multiplication. The units of S_v are $(\mathrm{m/s})^2/\mathrm{Hz}$. The frequencies corresponding to the elements of $\mathscr{F}_v$ and S_v are

$$f(k) = \frac{k}{t_s}, 1 \leq k \leq N. \tag{A.23}$$

However, the highest possible frequency with meaningful information (Nyquist frequency), is $\frac{1}{2}N/t_s$. Higher frequency data is prone to aliasing and should be discarded.

A model for the turbulence PSD in the inertial subrange is used to estimate dissipation rate from the measured PSD, $S_v(f)$. A model for the inertial subrange of the velocity PSD in terms of the turbulent dissipation is given in [21] as

$$S_v(f) = x_0 f^{-5/3} \tag{A.24}$$

where

$$x_0 = 0.146169\overline{U}_\infty^{2/3}\epsilon^{2/3}. \tag{A.25}$$

In Equation A.25, $\overline{U}_\infty$ is the average velocity of the wire during the measurement interval. The value for $\overline{U}_\infty$ comes from filtered GPS data. It should be noted that because this is a model for ambient turbulence, the mean velocity is not affected by prong blockage. This is unlike the mean velocity over the wire that was used above for evaluating the derivative of the power loss model. This turbulence model is then fit to the measured PSD where the fitting parameter is ϵ. The best fit value for ϵ is calculated by rearranging the model to solve for ϵ,

$$\epsilon(f)^{2/3} = \left(\frac{1}{0.146169 \overline{U}_\infty^{2/3}} \right) S_v(f) \odot f^{5/3}. \tag{A.26}$$

Equation A.26 gives ϵ as a function of frequency f. A single, best-fit value for ϵ can be calculated by taking a simple average

$$\epsilon^{2/3} = \left(\frac{1}{0.146169 \overline{U}_\infty^{2/3}} \right) \overline{S_v^*(f)} \tag{A.27}$$

where $S_v^*(f) = S_v(f) \odot f^{5/3}$ represents the signal PSD normalized by frequency raised to the $-5/3$ power. Also, the dependence of ϵ on f has been dropped because this now represents an average value that is independent of frequency. The relationship between some error in Δv and the subsequent error in ϵ is derived below.

A.4 Turbulent Dissipation Rate Sensitivity Analysis

Consider that the measured velocity fluctuations $\Delta v'$ differ from the true velocity fluctuations by some factor ξ such that

$$\Delta v' = \xi \Delta v. \tag{A.28}$$

Here ξ represents error or uncertainty in $\Delta v'$. With this consideration, the procedure laid out above can be applied to $\Delta v'$ to determine how ξ carries through to the calculated value for ϵ.

First, an FFT of the signal is calculated. The FFT is a linear operator which means one can

write

$$\mathscr{F}(\Delta v') = \mathscr{F}(\xi \Delta v) \tag{A.29}$$

$$\mathscr{F}_{v'} = \xi \mathscr{F}(\Delta v) \tag{A.30}$$

$$\mathscr{F}_{v'} = \xi \mathscr{F}_v \tag{A.31}$$

where $\mathscr{F}_{v'}$ is the FFT of the signal containing error and $\mathscr{F}_v$ is the true FFT. The calculation of the signal PSD then follows in a similar fashion as

$$\mathscr{F}_{v'} \odot \mathscr{F}^*_{v'} = \mathscr{F}(\xi \Delta v) \odot \mathscr{F}^*(\xi \Delta v) \tag{A.32}$$

$$S_{v'} = \xi^2 \mathscr{F}_v \odot \mathscr{F}^*_v \tag{A.33}$$

$$S_{v'} = \xi^2 S_v \tag{A.34}$$

where, again, $S_{v'}$ is the PSD of the signal containing error and S_v is the true PSD. Applying Equation A.27 to $S_{v'}$ for calculating the best-fit value of ϵ gives

$$(\epsilon')^{2/3} = \left(\frac{1}{0.146169 U^{2/3}} \right) \overline{S^*_{v'}(f)} \tag{A.35}$$

$$(\epsilon')^{2/3} = \left(\frac{1}{0.146169 U^{2/3}} \right) \xi^2 \overline{S^*_v(f)} \tag{A.36}$$

$$(\epsilon')^{2/3} = \xi^2 \epsilon^{2/3} \tag{A.37}$$

$$\epsilon' = \xi^3 \epsilon \tag{A.38}$$

So a given error in Δv represented by ξ carried through to ϵ results in ϵ' which is a factor of the original by the cube of the error in velocity fluctuations. This result is reasonable when considering that the power of a flow is proportional to the cube of velocity, and ϵ is the dissipation rate of the kinetic energy (i.e. dissipation power) of turbulent velocity fluctuations. Since values for ϵ are typically reported in terms of $\log_{10}(\epsilon)$, it is useful to write Equation A.38 as

$$\log_{10}(\xi^3) = \log_{10}\left(\frac{\epsilon'}{\epsilon} \right) \tag{A.39}$$

$$3 \log_{10}(\xi) = \log_{10}(\epsilon') - \log_{10}(\epsilon). \tag{A.40}$$

The term ξ is related to a percent error of Δv by

$$\%\text{Error} = 100 \times \frac{\Delta v' - \Delta v}{\Delta v} \tag{A.41}$$

$$\%\text{Error} = 100 \times \frac{\xi \Delta v - \Delta v}{\Delta v} \tag{A.42}$$

$$\%\text{Error} = 100 \times (\xi - 1). \tag{A.43}$$

Using Equations A.40 and A.43, Figure A.1 shows the relationship between errors in measured Δv and calculated ϵ. Based on input from meteorologists who model atmospheric turbulence, measures of $\log_{10}(\epsilon)$ that have an accuracy of +/- 0.5 or less would be useful for comparison with models. The dashed lines in the figure show these limiting reference lines. This range of acceptable accuracy in ϵ corresponds to a Δv error range of about -31% to $+46\%$ ($0.69 < \xi < 1.46$).

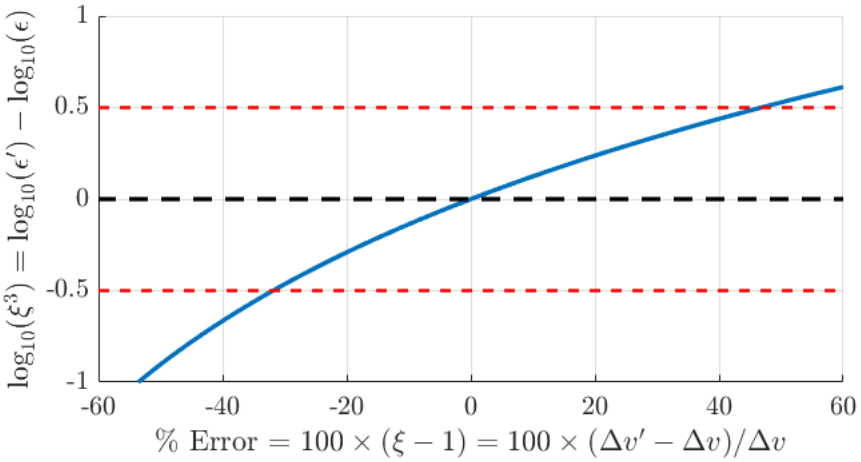

Figure A.1: Relationship between error in measured velocity fluctuations Δv and error in calculated turbulent dissipation rate ϵ. The black dashed line is a reference for no error. Red dashed lines represent $\pm$ 1/2 decade error in ϵ.

Given this constraint on Δv, the model for calculating Δv from measurements given in Equation A.20 can then be used to calculate subsequent uncertainty requirements for particular measured and model quantities such as flow properties, ΔH, and the power model derivative $\partial \text{Nu}/\partial \text{Re}$.